GROUND STATE OF ^{10}Li AND ^{13}Be

By

Shigeru Kennedy Yokoyama

A DISSERTATION

Submitted to
Michigan State University
in partial fulfillment of the requirements
for the degree of

DOCTOR OF PHILOSOPHY

Department of Physics and Astronomy

1996

ABSTRACT

GROUND STATE OF ^{10}Li AND ^{12}Be

By

Shigeru Kennedy Yokoyama

^{11}Li nucleus is known to have the structure of a ^{9}Li core and a two-neutron halo and is the heaviest particle stable Li isotope. The ground state study of ^{10}Li is important to understand the structure of ^{11}Li since it has information on the n +^{9}Li interaction which determines a significant part of the ^{11}Li three body structure. A direct mass measurement of ^{10}Li is impossible since it has very short lifetime (~10^{-21} s). Previous experimental studies have shown conflicting results for the ^{10}Li ground state. ^{13}Be information is also crucial for understanding of ^{14}Be structure similar to the ^{10}Li and ^{11}Li case. The goal of the current work is to determine the ground state properties of ^{10}Li and ^{13}Be.

The technique of sequential neutron decay spectroscopy (SNDS) was employed around 0° for the present study. The nuclei ^{10}Li, and ^{13}Be were created via fragmentation. They decayed immediately in the target and emitted a neutron and a fragment (^{9}Li and ^{12}Be) which were separated with magnets and detected. The relative velocity spectra were created from the experimental information. Monte Carlo simulations were performed and the results were compared with the data. The limit of the decay constants for each isotope were extracted via χ^2 analysis.

The low-lying *s*-wave ground state was established for ^{10}Li at $E_r \approx 50$ keV or $a_s \approx$ -40 fm. The result of ^{13}Be could be either interpreted as a low-lying *s*-wave state or the tail of the known state at 2.0 MeV.

To my wife, Kelly

ACKNOWLEDGMENTS

First, I would like to thank my advisor, Michael Thoennessen. He has always been a great help to me. His perspective always helped me stay on the right track and showed me the way to proceed. I could never have come this far without his help.

I thank professors Pawel Danielewicz, Michael Harrison, Wayne Repko, and Brad Sherrill for being my guidance committee. I also thank professor Gregers Hansen for insightful discussions and providing the scattering length calculations. As a collaborator, I really enjoyed having discussions with professor Aaron Galonsky.

I learned a lot from a former post-doc of our research group, Robert A. Kryger. He especially contributed to the improvement of my computer skills a great deal. Peter Thirolf, a former post-doc, was a good example to me in his way of being unintimidated with having too many things to do. His solid way of handling complicated tasks influenced my attitude toward the thesis writing.

It was very lucky for me to be able to work with Easwar Ramakrishnan, Afshin Azhari, Thomas Baumann, and Marcus Chromik as colleagues. I believe we were one of the best 'teams' in the NSCL. I would like to thank Afshin Azhari and Mike Fauerbach for their proofreading of my thesis drafts.

It was really enjoyable interacting with the people in the NSCL including John 'Ned' Kelley, Raman Pfaff, Don Sackett, Larry Phair, Mike Lisa, Wen-Chen Hsi, Tong Li, Eu-

gene Gualtieri, Stefan Hannuschke, Q. Pan, Damian Handzy, Jim Brown, Magie Hellström, Chris Powell, Jon Kruse, Jing Wang, Phil Zecher, Mathias Steiner, Sally Gaff, Barry Davids, Heiko Scheit, Thomas Glasmacher, Jac Caggiano, Njema Frazier, Corn Williams, Richard Ibbotson, Roy Lemmon, Gerd Kunde, Razvan Popescu, Luke Chen, Renan Fontus, and Kyoko Fuchi.

I would like to thank all the staff of the NSCL, especially Raman Anantaraman, Reg Ronningen, Richard Au, Ron Fox, Barbara Pollack, John Yurkon, Dennis Swan, Dave Sanderson, and Craig Snow. They saved me from many troubles I encountered while I conducted experiments and research in the NSCL.

My experience at the NSCL gave me the privilege to meet international visitors such as Toshiyuki Kubo, Yoshiyuki Iwata, and Ákos Horváth. Meeting and working with people from all over the world was a very unique and valuable experience.

I also would like to thank my computer at home PowerMacintosh 7500/100, Zip drive, and 28.8kbps modem for their stable operation. I wrote the thesis with this system. At the beginning of 1996, 100MHz clock speed and 28.8kbps modem was kind of fast but I'm sure that readers will find it ridiculously slow in the very near future.

I would like to thank my friend Dr. Frederick I. Kaplan for his encouragement and help in my life in Michigan.

I am also thankful for my friendship family in Michigan, Roy and Elaine Pentilla. Their hospitality was very heart warming especially during the cold holiday season in Michigan.

I thank my family in Japan and my brother Naohiko in L.A. for all sorts of support. I'm glad that all of my family could visit me in East Lansing while I was studying at Michigan State University.

Finally I thank my wife Kelly Yokoyama Kennedy for her love and support. In finally reaching this goal I deeply thank all those people around me in Michigan. I will never forget the people and the beautiful campus of Michigan State University.

TABLE OF CONTENTS

LIST OF TABLES ix

LIST OF FIGURES x

Chapter 1
Introduction 1

Chapter 2
Neutron Halo Nuclei 3
2.1 The Two-Neutron Halo Nucleus ^{11}Li 3
2.2 ^{10}Li And ^{11}Li Three-Body Models 6
2.3 Recent Reports of The ^{10}Li Ground State 12
2.4 ^{14}Be Three-Body Models and ^{13}Be Ground State 22

Chapter 3
Experimental Details 25
3.1 Experimental Method 25
3.2 Mechanical Setup 27
3.3 Neutron Detectors 31
3.4 Fragment Telescope 33
3.5 Electronics and Data Acquisition 37

Chapter 4
Data Analysis 41
4.1 Overview 41
4.2 Calibration of Detectors 42
4.2.1 Calibration of the Fragment Telescope 42
4.2.2 Neutron Detector Calibration 51
4.2.3 Time Calibration 53
4.3 Coincidence Fragment Spectra 55
4.3.1 He group 57
4.3.2 Li Group 58

4.3.3 Be Group....60
4.4 Simulation of Experiment....61

Chapter 5
Results and Discussion....65
5.1 Selection of The Valid Events....65
5.2 The Relative Velocity Spectrum of ^{7}He....65
5.3 The Relative Velocity Spectrum of ^{10}Li....69
5.3.1 The *s*-wave Case....75
5.3.2 The *p*-wave Case....80
5.4 The Relative Velocity Spectrum of ^{13}Be....82
5.4.1 The *s*-wave Case....84
5.4.2 The *d*-wave Case....88

Chapter 6
Summary and Conclusions....92

BIBLIOGRAPHY....94

LIST OF TABLES

Table 3.1 A example of an output file of the INTENSITY [Win92] calculation for an 80 MeV/nucleon ^{18}O beam (intensity = 10 pnA) with a 94 mg/cm^2 ^{9}Be Target. 29

Table 4.1 Calibration beam energies for different target thicknesses. 42

LIST OF FIGURES

Figure 2.1 [Kob88] (a) Transverse-momentum distributions of ^{6}He fragments from the reaction ^{8}He + C. The solid lines are fitted Gaussian distributions with a reduced width of $\sigma_0 = 59$ MeV/c. (b) Transverse-momentum distributions of ^{9}Li fragments from reaction ^{11}Li + C. The solid lines are fitted distributions with two Gaussian components. The dotted line is a contribution of the wide component in the ^{9}Li distribution. The reduced width of the two components are $\sigma_0 = 71$ MeV/c and $\sigma_0 = 17$ MeV/c, respectively.....5

Figure 2.2 [Han87] The calculated relations between the matter r.m.s. radius and 2n separation energy with mass parameters corresponding to ^{11}Li and ^{6}He by Hansen and Jonson. The experimental values for radii and 2n separation energies were taken from [Tan85] and [Wap85]. 7

Figure 2.3 [Ber91] The dependence of the ^{11}Li two neutron separation energy to the ^{10}Li $1p_{1/2}$ state energy predicted by Bertsch and Esbensen. The solid line and dashed line show correlated and uncorrelated neutron cases, respectively. ...8

Figure 2.4 [Tho94] The comparison of the calculated ^{9}Li core momentum distributions from ^{11}Li fragmentation by Thompson and Zhukov and the experimental data by Orr *et al.* (square) and Kobayashi *et al.* (star). The calculation includes *s*-wave potential as well as *p*-wave potential in n-^{9}Li interaction. 10

Figure 2.5 [Tho94] The calculated relation between ^{11}Li binding energy, $vp_{1/2}$ resonance energy, and $vs_{1/2}$ scattering length. The horizontal solid line shows the observed two-neutron binding energy of ^{11}Li by Kobayashi *et al.* [Kob92]....11

Figure 2.6 [Wil75] The energy spectra of ^{8}B was obtained from the following reactions using 121 MeV ^{12}C beam. (a) ^{12}C(^{9}Be,^{8}B)^{13}B is for an energy calibration, (b) ^{9}Be(^{9}Be,^{8}B)^{10}Li is from singles events, and (c) ^{9}Be(^{9}Be,^{8}B)^{10}Li is from coincidence events with ^{9}Li from the breakup of the recoiling ^{10}Li. The angle was at 14° in the laboratory. 13

Figure 2.7 [Ame90] The spectrum of protons produced in absorption of stopped π^- mesons by ^{11}B nuclei. The arrow shows the resonance at $E_r = 0.15 \pm 0.15$ MeV and $\Gamma < 0.4$ MeV.....14

Figure 2.8 Competition between $s_{1/2}$ and $p_{1/2}$ levels among N=7 nuclei [Tal60]. The levels are shifted to match the lowest $p_{1/2}$ state. Extrapolation implies the non-normal parity ground state of ^{10}Li [Bar77].....14

Figure 2.9 [Boh93] Energy spectra of ^{12}N from the reaction of ^{9}Be(^{13}C,^{12}N)^{10}Li by Bohlen *et al.* The ground state (E_r = 0.42 MeV) and the first excited state at E_x = 0.38 MeV (E_r = 0.80 MeV) are not completely resolved. 15

Figure 2.10 [You94] The energy spectrum from the transfer reaction ^{11}B(^{7}Li,^{8}B)^{10}Li by Young *et al.* It shows a strong evidence of the state at $E_r \approx$ 500 keV. 16

Figure 2.11 [Kry93] The relative velocity spectra of ^{9}Li + n coincidence events obtained with sequential neutron decay spectroscopy by Kryger *et al.* The dashed line is a simulated spectrum with the parameter by Wilcox *et al.* (E_r = 800 keV, l = 1) superimposed on the Gaussian background (dotted). The solid line is a simulated spectrum with the parameter by Amelin *et al.* (E_r = 150 keV, l = 0) plus the Gaussian background. 17

Figure 2.12 [Zin95] Radial momentum distributions of neutrons from ^{10}Li breakup reported by Zinser *et al.* ^{10}Li was created by one proton stripping from ^{11}Be (top) or by one neutron stripping from ^{11}Li (bottom). In the top figure, the top dotted line assumes an l = 1 resonance at 0.05 MeV. The two sets (a_s = -5 and -50 fm) of the calculations were shown with the ^{9}Li recoil widths σ_Q = 100 MeV/c (solid) and σ_Q = 0 MeV/c. In the bottom figure, two contributions were considered in the theoretical curves. One is diffraction (1/3 intensity) and the other is the intermediate state of ^{10}Li (2/3 intensity) which was assumed to be a pure s state. 19

Figure 2.13 [Ost96] Spectra of the ^{10}Be(^{12}C,^{12}N)^{10}Li reaction by Ostrowski *et al.* Although the state reported by Bohlen *et al.* [Boh93] at E_r = 0.42 MeV was assumed to be there for fitting, it is not resolved from the ground state at E_r = 0.24 MeV. The state reported by Wilcox *et al.* at 0.8 MeV was not observed in these spectra. 21

Figure 2.14 [Kor95] The proton spectrum from the reactions CD^2(^{12}Be,p) (solid) and C(^{12}Be,p) (dotted). The lowest state extracted reliably is at E_r = 2 MeV. ...23

Figure 3.1 Kinematic diagram of the sequential neutron spectroscopy for the ^{10}Li decay. 25

Figure 3.2 Floor plan of the National Superconducting Cyclotron Laboratory. 28

Figure 3.3 Top view of the experimental setup. 30

Figure 3.4 The dimensions of one neutron detector and the configuration of the whole detector array. The gray area shows the neutron sensitive part. 32

Figure 3.5 Simulated efficiency curve of the neutron detector with a sideway geometry. It was calculated with the code KSUEFF [Cec79]. 33

Figure 3.6 Efficiency plot of the neutron detection for the ^{10}Li neutron decay for the decay energy range of 0.00 MeV < E_r < 1.00 MeV. The energy dependent solid angle coverage of the neutron detectors, the energy dependent neutron detector efficiency, and fragment detector acceptance are folded as a total neutron detection efficiency. The upper abscissa indicates a corresponding decay energy. 34

Figure 3.7 Schematic of the fragment telescope. 35

Figure 3.8 Front view of one of the ΔE Si detectors. The gray area shows the sensitive region. The crossed lines on the gray area indicates the segmentation lines. 36

Figure 3.9 Structure of CsI(Tl) E detector array. Each of the nine crystals were wrapped with white blotter paper independently to optically isolate them from each other. 37

Figure 3.10 Diagram of the electronics. 38

Figure 4.1 Two dimensional histogram of energy loss in the ΔE2 detector's quadrant number 1 versus time of flight of the fragments. m/q = isotopes are selected using the A1200 mass analyzer.....44

Figure 4.2 Two dimensional histogram of energy loss in the ΔE2 detector's quadrant number 1 versus total energy in the E3 detector of the fragments. The large square gate in the plot was applied to select the valid signal for a projection.....44

Figure 4.3 Energy spectrum of the calibration beam with an A/Z = 3 gate. 46

Figure 4.4 Quadratic fitting for energy calibration of the ^{6}He fragment for each E detector. The E2 detector was omitted due to its nonlinear behavior. 47

Figure 4.5 Quadratic fitting for energy calibration of the ^{9}Li fragment for each E detector. The E2 detector was omitted due to its nonlinear behavior. 48

Figure 4.6 Quadratic fitting for energy calibration of the ^{12}Be fragment for each E detector. The E2 detector was omitted due to its nonlinear behavior. 49

Figure 4.7 Energy loss spectrum of the calibration beam with A/Z=3 gate.....50

Figure 4.8 Timing diagram of the neutron signals and the QDC gate. Shaded areas show the integrated part of the neutron signal. 51

Figure 4.9 Two dimensional plot of the neutron detector signal. A ^{239}Pu-Be source was used to supply γ-rays and neutrons along with ^{60}Co γ-ray source. 52

Figure 4.10 Compton edges of a ^{60}Co source and a ^{239}Pu-Be source in a one dimensional plot of the neutron total signal. It was obtained by using the γ-ray condition established in the two dimensional plot (Figure 4.9). 53

Figure 4.11 The relation of the fragment time signal, the neutron detector signal, and the RF time signal. The earliest and latest possible neutron signal have margins of ~ 25 ns from the edge of the fragment signal to take a fragment time spread into account. 56

Figure 4.12 ΔE_1 (first quadrant of ΔE) vs. E3 plot of He group. The oval contour shows a ^{6}He gate. 57

Figure 4.13 ΔE_1 (first quadrant of ΔE) vs. TOF (thin plastic time) plot of He group. The contour gates show the ^{6}He reals gate and the ^{6}He randoms gate. 58

Figure 4.14 ΔE_1 (first quadrant of ΔE) vs. E3 plot of the Li group. The contour shows a ^{9}Li isotope gate. 59

Figure 4.15 ΔE_1 (first quadrant of ΔE) vs. TOF (thin plastic time) plot of Li group. The contour gates show the ^{9}Li reals gate and the ^{9}Li randoms gate. 59

Figure 4.16 ΔE_1 (first quadrant of ΔE) vs. E3 plot of the Be group. The contour shows a ^{12}Be isotope gate. 60

Figure 4.17 ΔE_1 (first quadrant of ΔE) vs. TOF (thin plastic time) plot of Be group. The contour gates show the ^{12}Be reals gate and the ^{12}Be randoms gate. 61

Figure 4.18 χ_ν^2 versus neutron TOF resolution plot. χ_ν^2 is for the fit of the ^{7}He neutron decay simulation and the data. The minimum χ_ν^2 of (best fit) is at t_{nres} ~ 0.70 ns. 63

Figure 5.1 The relative velocity spectrum for ^{6}He + n coincidence events. The circles with the error bars are the data. The dashed line shows the estimated background. The dotted line is the simulated decay of ground state of ^{7}He without the background and the solid line is a sum of the background and the simulation. 66

Figure 5.2 The Breit-Wigner lineshapes of ^{7}He state at Er = 440 keV with the width of Γ = 160 keV. The solid line shows the actual case with the angular momentum l = 1. For the comparison, l = 0 case is shown with the dashed line. The low energy region of the peak for the l = 1 case is suppressed compared to the l = 0 case. 68

Figure 5.3 The relative velocity spectrum simulation of $^{7}He \rightarrow {}^{6}He + n$ decay for the different time resolutions. The dotted line shows a case of perfect resolution (σ_{tn} = 0.00 ns, σ_{tf} = 0.00 ns). The solid line shows a case of a current experimental resolution (σ_{tn} = 0.70 ns, σ_{tf} = 0.057 ns). The dashed line shows a case of the experiment by Kryger *et al.* (σ_{tn} = 0.89 ns, σ_{tf} = 0.89 ns).....70

Figure 5.4 The relative velocity spectrum of $^{10}Li \rightarrow {}^{9}Li + n$. The convention of the data point and the Gaussian background are the same as the ^{7}He spectrum. The dashed side peaks are the simulation of the *p*-wave state at E_r = 538 keV reported by Young *et al.* The dashed central peak is the simulation with l = 0, E_r = 50 keV, Γ_0 = 241keV. This is the fit at χ_ν^2 minimum for the *s*-wave neutron.....72

Figure 5.5 The level diagram of the possible two cases of the neutron decay of ^{10}Li...74

Figure 5.6 The valid region of the *Er* and Γ_0 space based on the χ^2 analysis and Wigner limit for *s*-wave initial state of ^{10}Li.....76

Figure 5.7 The result of the calculations with the Faddeev three body function for the ^{11}Li binding energy as a function of $1p_{1/2}$ resonance energy and the scattering length of the $1s_{1/2}$ low-lying state. The current result a_s = -40.0 fm is indicated with the solid line.....78

Figure 5.8 The ^{10}Li lineshapes used for the best fit of the simulation to the data. The relative population of the *s*-wave and *p*-wave is 33% and 67%, respectively..79

Figure 5.9 The valid region of the E_r and Γ_0 space based on the χ^2 analysis and Wigner limit for *p*-wave initial state of ^{10}Li.....81

Figure 5.10 The relative velocity spectrum of the $^{12}Be + n$ coincidence events. 83

Figure 5.11 The level diagram of the possible two cases of the neutron decay of ^{13}Be..85

Figure 5.12 The valid region of the E_r and Γ_0 space based on the χ^2 analysis and the Wigner limit for *s*-wave initial state of ^{13}Be. 86

Figure 5.13 The ^{13}Be lineshapes used for the best fit of the simulation to the data. The relative population of the *s*-wave and *d*-wave is 44% and 56%, respectively..87

Figure 5.14 The valid region of the E_r and Γ_0 space based on the χ^2 analysis and Wigner limit for *d*-wave initial state of ^{13}Be. The case (a) in Figure 5.11 is assumed.....89

Figure 5.15 The result of χ^2 analysis in the case of *d*-wave state in ^{13}Be as an initial state and the first excited state of ^{12}Be as a final state.....90

Chapter 1

Introduction

The field of exotic nuclei is currently one of the most active areas studied in nuclear physics. Recent advancements of equipment and facilities have provided unique opportunities to study nuclei near and beyond the neutron and proton drip lines. There are two major motivations to study exotic nuclei. One reason to study exotic nuclei is for nuclear astrophysics. The stellar evolution process begins with H and He atoms from the big bang [Rol88]. Starting out with hydrogen burning, the more complex atoms were formed via various nuclear reaction cycles such as the CNO (carbon-nitrogen-oxygen) cycle [Won90]. Exotic nuclei often play an important role within these reaction cycles and the information on those nuclei is crucial to explain the abundance of the elements and to determine the age of stars. Another motivation to study exotic nuclei is that unique tests of the fundamental laws of physics and nuclear models can be carried out by studying the properties of those nuclei.

Exotic nuclei are either neutron or proton rich. The current work is a study of ^{10}Li and ^{13}Be, which are light nuclei on the neutron dripline. The nuclei ^{11}Li and ^{9}Li are known to be bound nuclei and ^{11}Li is the heaviest particle stable Li isotope. The nucleus ^{11}Li is also known to consist of a two-neutron halo around a ^{9}Li core. Unlike other nuclei which have an uniform nuclear matter density, halo nuclei have a lower nuclear matter density region (halo) around the normal nuclear matter density region (core). The recent experimental ef-

forts to study the halo nuclei also stimulated the interest of theorists. Various model calculations for the halo nuclei have been reported. For the ^{11}Li case, structure information of ^{10}Li, which is an unbound nucleus, turns out to be crucial for the theoretical calculations as a subsystem of the halo nucleus ^{11}Li. One of the goals of the current experiment was to measure the ground state energy level of ^{10}Li. Since it is particle unbound, it is impossible to measure the energy in a direct way. We employed the technique of neutron sequential decay spectroscopy at 0° and extracted the ground state energy and width of ^{10}Li.

The situation in Be isotopes is similar to the Li isotopes. The nucleus ^{14}Be is the heaviest stable isotope and also considered a two-neutron halo nucleus whereas ^{13}Be is particle unstable. Again the n-^{12}Be interaction, or ^{13}Be is important for the understanding of ^{14}Be. Previous work and the relations of the ^{10}Li structure to the ^{11}Li model as well as ^{13}Be and ^{14}Be are discussed in the next chapter.

Chapter 2

Neutron Halo Nuclei

2.1 The Two-Neutron Halo Nucleus ^{11}Li

^{11}Li is the heaviest particle-stable nucleus among the Li isotopes. It has been known as a neutron drip-line nucleus since ^{10}Li is unbound toward one neutron decay and ^{12}Li is not bound either. ^{11}Li has a half-life of 8.2 ms for β^- decay to ^{11}Be. Tanihata *et al.* [Tan85] measured the interaction cross sections (σ_I) of lithium isotopes (^{6}Li, ^{7}Li, ^{8}Li, ^{9}Li, and ^{11}Li) and beryllium isotopes (^{7}Be, ^{9}Be, and ^{10}Be) on the targets of Be, C, and Al at 790 MeV/ nucleon using the novel technique of exotic isotope beams produced through projectile fragmentation in high energy heavy ion reactions. The extracted root mean square (rms) nuclear radii from the σ_I showed that ^{11}Li has an unusually large radius (R_I = 3.14 fm) compared to neighboring nuclei ($R_I \approx 1.2$ fm x $A^{1/3}$ [Kra88] (= 2.5 fm for ^{9}Li)). It was interpreted as a large deformation and/or a long tail in the matter distribution due to the weakly bound neutrons.

To investigate the nature of the large matter radius of ^{11}Li, different experiments were performed, for example momentum distribution measurements. Previous studies showed that the momentum distribution of fragmentation products have a Gaussian distribution which is isotropic in the projectile rest frame [Gre75]. The width of the Gaussian

distribution σ is related to the Fermi momentum or the temperature corresponding to the nuclear binding energy [Gol74] and the momentum distribution inside the projectile [Hüf81]. Goldhaber [Gol74] parameterized the width σ of the Gaussian shape momentum distribution by a single parameter σ_0 (reduced width) defined as

$$\sigma^2 = \sigma_0^2 \frac{F(A-F)}{A-1} \tag{3.1}$$

where F is the mass number of the fragment and A is the mass number of the projectile.

Kobayashi *et al.* [Kob88] measured the transverse momentum distribution of ^{9}Li from the fragmentation of ^{11}Li on a C target to investigate the structure of ^{11}Li. The secondary beams of ^{11}Li, as well as ^{8}He, and ^{6}He of 790 MeV/nucleon were fragmented on a C, and a Pb target and projectile fragments were measured at zero degrees with a magnetic spectrometer. The transverse-momentum distribution of ^{6}He fragments from the reaction ^{8}He + C (Figure 2.1 (a)) exhibited a Gaussian shape. For the He data, a reduced width of $\sigma_0 \sim 60$ MeV/c was extracted. The momentum distribution of ^{9}Li from the reaction ^{11}Li + C (Figure 2.1 (b)) showed a different structure. Two Gaussian distributions were superimposed in the ^{11}Li spectrum. The reduced width of the wider component was $\sigma_0 = 71$ MeV which is similar to the value of ^{12}C fragmentation data ($\sigma_0 \approx 78$ MeV) by Greiner *et al.* [Gre75]. The second component had an extremely narrow reduced width of $\sigma_0 = 17$ MeV. The momentum distribution of one-nucleon-removal fragments reflects the momentum distribution of the removed nucleon at the surface of the projectile [Hüf81]. The idea was extended to a several-nucleon-removal channel to interpret the two components in the momentum distribution of ^{9}Li. The narrow component was considered to originate from the removal of the two weakly bound outer neutrons in ^{11}Li. The broader component was interpreted as a result of the removal of normally bound neutrons, decay of excited ^{9}Li, and the decay of ^{10}Li.

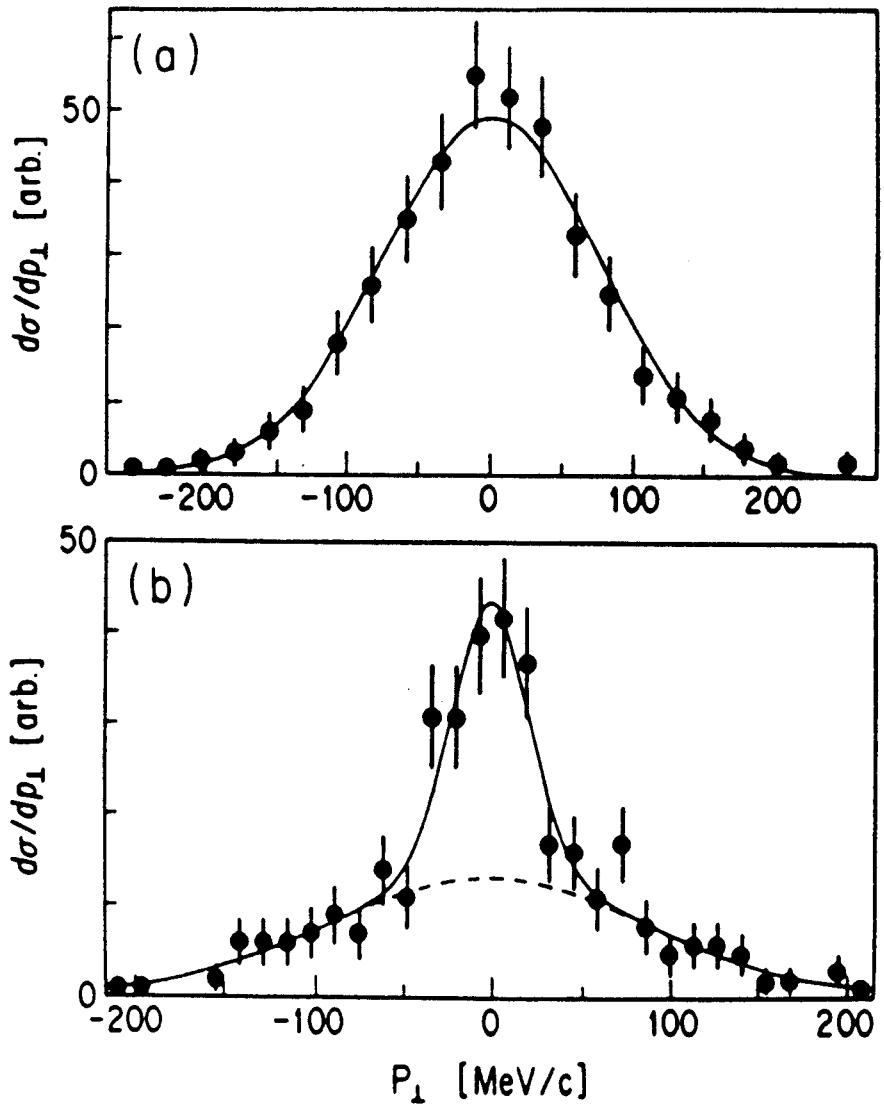

Figure 2.1: [Kob88] (a) Transverse-momentum distributions of ^{6}He fragments from reaction ^{8}He + C. The solid lines are fitted Gaussian distributions with a reduced width of σ_0 = 59 MeV/c. (b) Transverse-momentum distributions of ^{9}Li fragments from reaction ^{11}Li + C. The solid lines are fitted distributions with two Gaussian components. The dotted line is a contribution of the wide component in the ^{9}Li distribution. The reduced width of the two components are σ_0 = 71 MeV/c and σ_0 = 17 MeV/c, respectively.

A large root mean square radius, small momentum distribution width component in the projectile fragmentation, and a small separation energy of the two outer neutrons (S_n = 295keV [You93]), suggest the existence of a large two-neutron halo around the ^{9}Li core in ^{11}Li. This structural characteristic has subsequently been found in many other light neutron-rich nuclei (^{6}He, ^{11}Li, ^{11}Be, ^{14}Be, etc.) [Han95, Tho96].

Before the experimental discovery of the neutron halo, Migdal [Mig73] suggested that the force between two neutrons may lead to a bound state of the two neutrons and a nucleus even if a combination of the two do not form a bound state. Hansen and Jonson [Han87] interpreted Migdal's suggestion on ^{11}Li as a quasi-deuteron consisting of a ^{9}Li core coupled to a dineutron [^{2}n]. A radial square well potential was assumed for the ^{9}Li core and the binding energy of the dineutron was assumed to be zero. The external wave function of the dineutrons outside the core was approximated for the small binding energy B between the ^{9}Li core and the dineutron by

$$\psi(r) = (2\pi\rho)^{-1/2}\frac{\exp[-r/\rho]}{r}\left[\frac{\exp[R/\rho]}{(1+R/\rho)^{1/2}}\right] \tag{3.2}$$

where R is the radius of a square well potential, r is the distance between the ^{9}Li and the dineutron. The decay length ρ in Equation 3.2 is defined as $\rho = \hbar/(2\mu B)^{1/2}$ where μ is the reduced mass of the system and B is the binding energy. This simple model agrees well with the experimental results for the radius and the 2n separation energy (see Figure 2.2).

2.2 ^{10}Li And ^{11}Li Three-Body Models

After Hansen and Jonson's two-body calculation [Han87] for ^{11}Li, a number of three-body model calculations were performed to obtain a more detailed understanding of ^{11}Li. For the three-body calculations of ^{11}Li, detailed information about the ^{10}Li states are essential

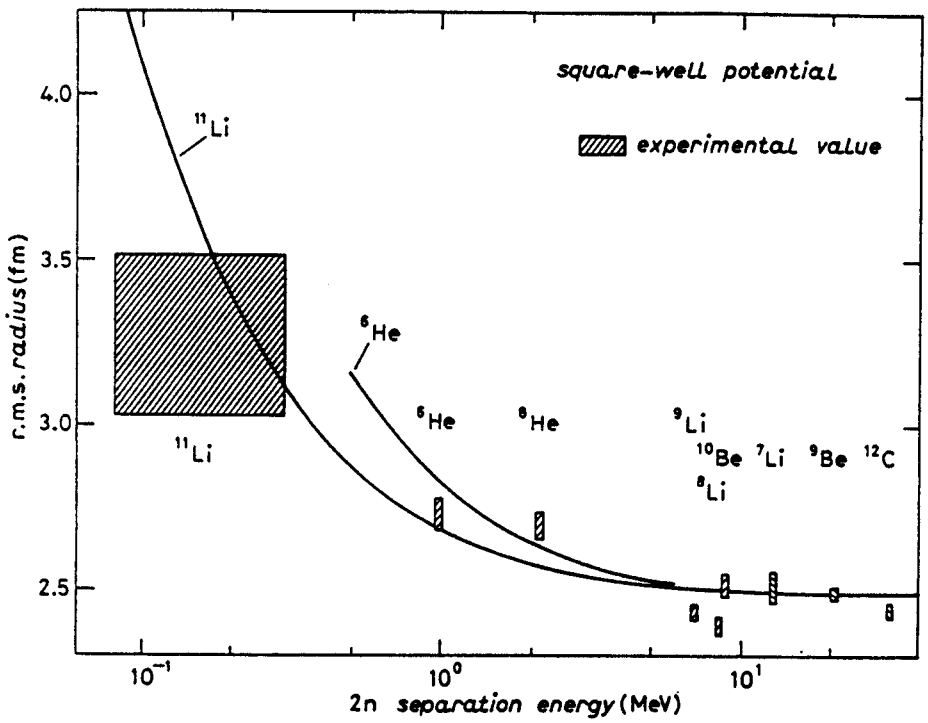

Figure 2.2: [Han87] The calculated relations between the matter r.m.s. radius and 2n separation energy with mass parameters corresponding to ^{11}Li and ^{6}He by Hansen and Jonson. The experimental values for radii and 2n separation energies were taken from [Tan85] and [Wap85].

input parameters.

Bertsch and Esbensen treated ^{11}Li as a three-body system consisting of two interacting neutrons together with a structureless ^{9}Li core [Ber91]. They used a two-particle Green's function technique to describe the two-neutron wave function. A Woods-Saxon potential, with a kinetic energy operator and a spin-orbit interaction were used for the single particle Hamiltonian. The numerical test was performed assuming the ground state of ^{10}Li to be a $\nu p_{1/2}$ state (see Figure 2.3). The result was compared with the available experimental data of the ^{10}Li ground state energy at 0.8 MeV [Wil75] and they obtained a two-neutron separation energy of 0.20 MeV which is approximately consistent with the available experimental value of 0.25 ± 0.01 MeV [Thi75, Wou88] at that time.

Bang and Thompson [Ban92] performed three-body calculations for ^{11}Li by applying the Faddeev three body equations [Lav73] using the super soft core potential SSCC

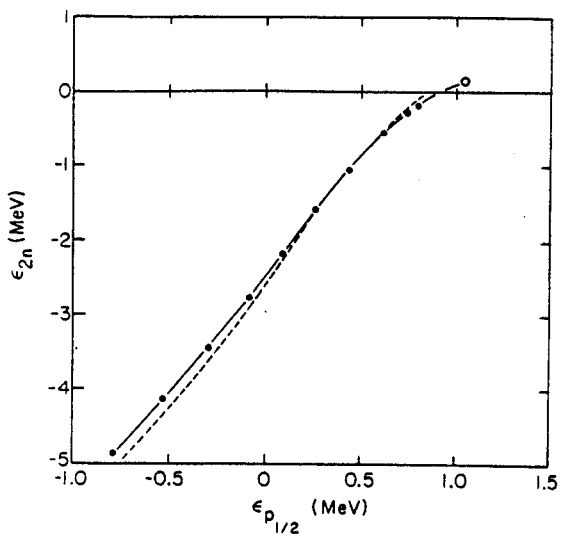

Figure 2.3: [Ber91] The dependence of the ^{11}Li two neutron separation energy to the ^{10}Li $1p_{1/2}$ state energy predicted by Bertsch and Esbensen. The solid line and dashed line show correlated and uncorrelated neutron cases, respectively.

[Tou75], or the Reid soft-core potential RSC [Rei68] for the neutron-neutron potential V_{nn}. Choosing parameters to give a $1p_{3/2}$ level at the energy of the ^{9}Li neutron separation energy (-4.1 MeV) and varying $1p_{1/2}$ resonance energy between 0.4 and 0.7 MeV, a Woods-Saxon potential and a spin-orbit term, or a Woods-Saxon potential and a pairing term were used for the core-neutron potential V_{cn}. Although they reproduced the main features of the halo in their results, some inconsistencies were found for fitting both the energies and the radius of ^{11}Li simultaneously.

Thompson and Zhukov [Tho94] performed a second Faddeev three-body calculation for ^{11}Li. It was shown that the presence of a near-threshold *s*-wave virtual state in the ^{9}Li + n two-body potential within the three-body calculation for ^{11}Li had an explicit effect on the calculated structure of the ^{11}Li halo. A Woods-Saxon potential was considered for the neutron-^{9}Li potential where the *s*- and *p*-wave strengths V_s and V_p along with the spin-orbit strength V_{SO} were varied to fit a particular $2s$ scattering length while maintaining the $1p_{1/2}$ resonance energy between +0.15 and +0.50 MeV. The $1p_{3/2}$ energy was kept constant at -4.1 MeV which is the neutron separation energy of ^{9}Li. Assuming a nearly 50% *s*-wave motion between the halo neutrons and the core, their results agreed very well with the experimental data obtained by Kobayashi *et al.* [Kob88] and Orr *et al.* [Orr92], see Figure 2.4. The interaction of the halo neutrons was accounted for by using the realistic super-soft-core nn potential (SSC). Figure 2.5 shows the results of this calculation and it will be compared with the experimental results presented in Chapter 5.

At the time of these calculations, the only available experimental data of the ^{10}Li ground state were the measurements by Wilcox *et al.* [Wil75] and Amelin *et al.* [Ame90]. Wilcox and collaborators studied ^{10}Li using the ^{9}Be(^{9}Be,^{8}B)^{10}Li reaction with a 121 MeV

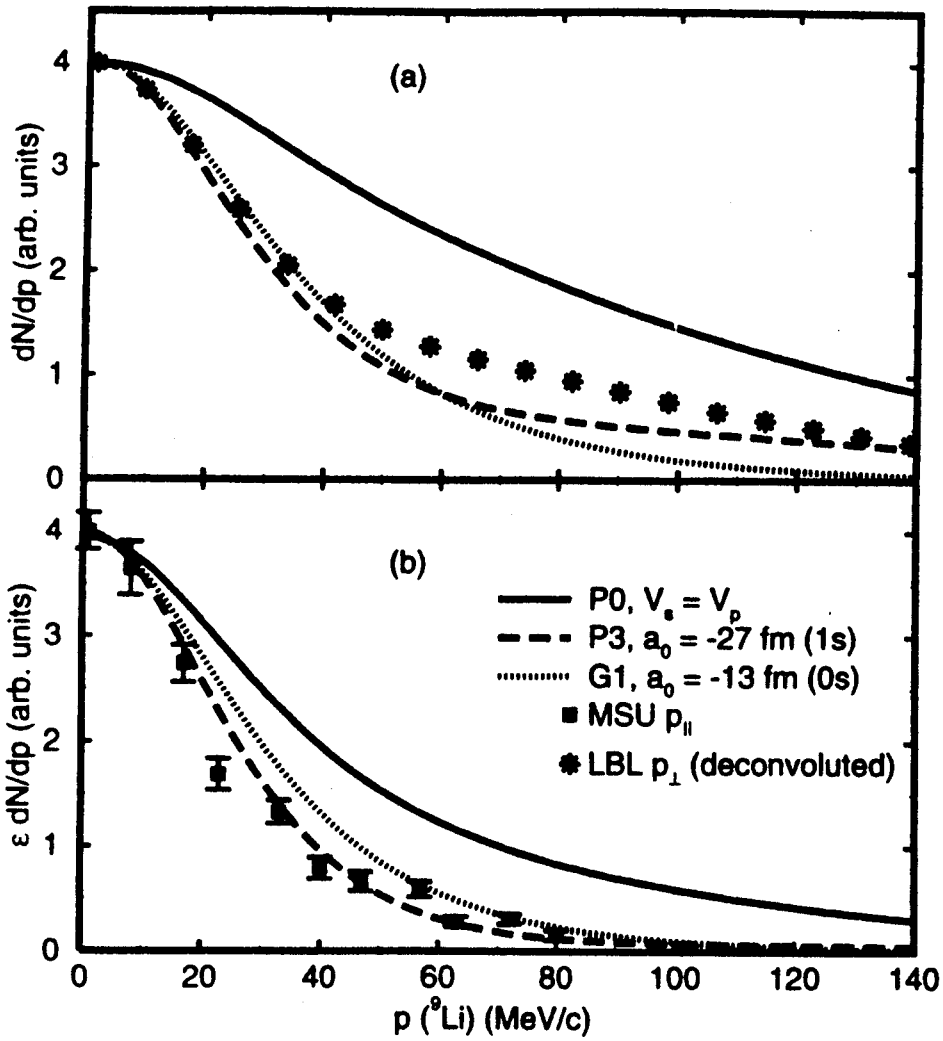

Figure 2.4: [Tho94] The comparison of the calculated ^{9}Li core momentum distributions from ^{11}Li fragmentation by Thompson and Zhukov and the experimental data by Orr *et al.* (square) and Kobayashi *et al.* (star). The calculation includes *s*-wave potential as well as *p*-wave potential in n-^{9}Li interaction.

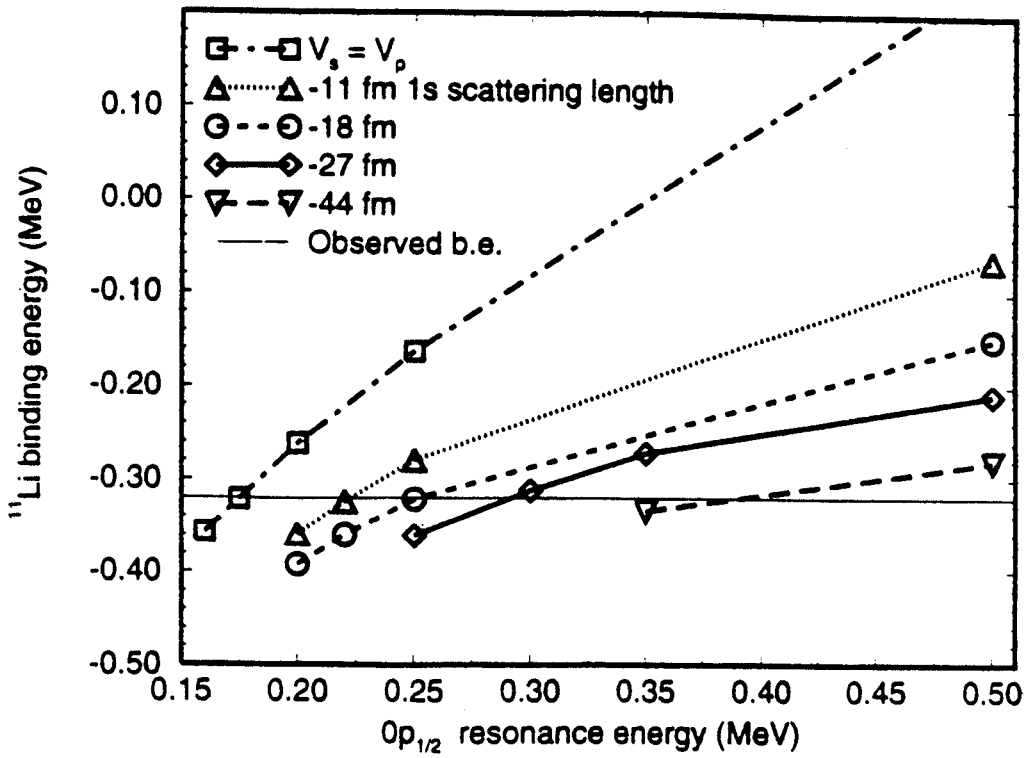

Figure 2.5: [Tho94] The calculated relation between ^{11}Li binding energy, $vp_{1/2}$ resonance energy, and $vs_{1/2}$ scattering length. The horizontal solid line shows the observed two-neutron binding energy of ^{11}Li by Kobayashi *et al.* [Kob92].

^{9}Be beam on a 0.68 mg/cm^2 ^{9}Be foil. The ground state was observed at S_n = -0.80 ± 0.25 MeV with a width of Γ = 1.2 ± 0.3 MeV (see Figure 2.6). Amelin *et al.* used the absorption of stopped π^- mesons by ^{11}B nuclei and observed the energy spectrum of protons near the kinematic limits of the reaction to study ^{10}Li. The resonance parameters of $E_r = 0.15 \pm 0.15$ MeV with a width of $\Gamma_0 < 0.4$ MeV were extracted assuming an *s*-wave state by fitting the Breit-Wigner resonance shape using the χ^2 test, see Figure 2.7.

2.3 Recent Reports of The ^{10}Li Ground State

Shortly after the first measurement of ^{10}Li by Wilcox, Barker and Hickey [Bar77] discussed the ground state configuration of ^{10}Li. The ^{10}Li structure was compared to the ^{11}Be configuration since both nuclei contain the same number of neutrons. The ground state of ^{11}Be is known to have a non-normal parity state ($J^\pi = 1/2^+$) and is considered to have $1s^4 1p^6 2s$ structure. The lowest normal parity state ($J^\pi = 1/2^-$) is at 0.32 MeV above the ground state which is considered to have a $1s^4 1p^7$ configuration. Since the energy of the lowest non-normal parity state relative to the lowest normal parity state increases as Z increases for the nuclei with N = 7 and Z > 4 (1.67 MeV for ^{12}B and 3.09 MeV for ^{13}C) [Tal60] (Figure 2.8), the ground state of ^{10}Li was expected to have non-normal parity state ($J^\pi = 1^-$ or 2^-) by extrapolation. A ground state level of the ^{10}Li was estimated using the available experimental data [Che70] of an $T = 2$ isobaric analog state of ^{10}Be. The result showed that it was expected close to ^{9}Li + n threshold and lower than the experimental data of the ^{10}Li state at 0.8 MeV by Wilcox *et al.* which was attributed to the lowest normal parity state.

The more recent experimental data reported by Bohlen *et al.* (Figure 2.9) [Boh93] and Young *et al.* (Figure 2.10) [You94] established the existence of a *p*-wave state around 500

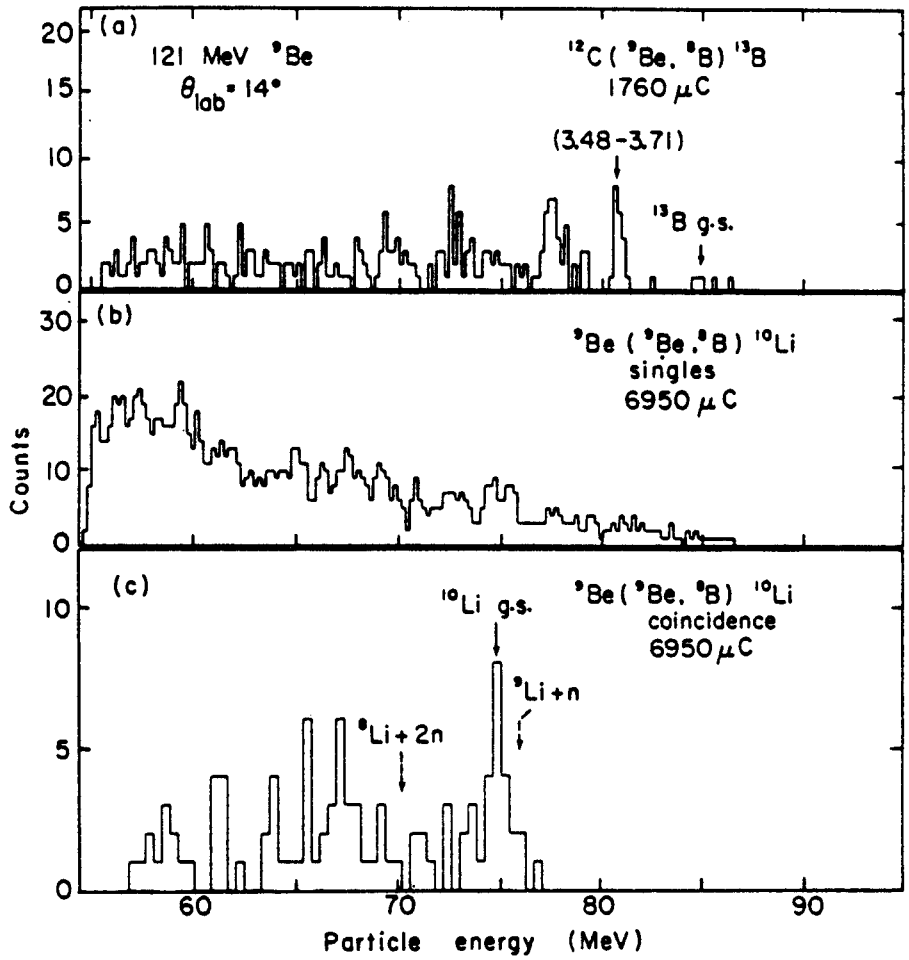

Figure 2.6: [Wil75] The energy spectra of ^{8}B was obtained from the following reactions using 121 MeV ^{12}C beam. (a) ^{12}C(^{9}Be,^{8}B)^{13}B is for an energy calibration, (b) ^{9}Be(^{9}Be,^{8}B)^{10}Li is from singles events, and (c) ^{9}Be(^{9}Be,^{8}B)^{10}Li is from coincidence events with ^{9}Li from the breakup of the recoiling ^{10}Li. The angle was at 14° in the laboratory.

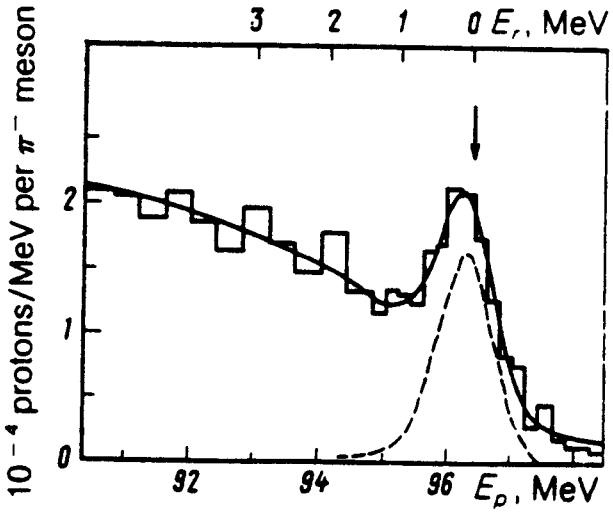

Figure 2.7: [Ame90] The spectrum of protons produced in absorption of stopped π^- mesons by ^{11}B nuclei. The arrow shows the resonance at $E_r = 0.15 \pm 0.15$ MeV and $\Gamma < 0.4$ MeV.

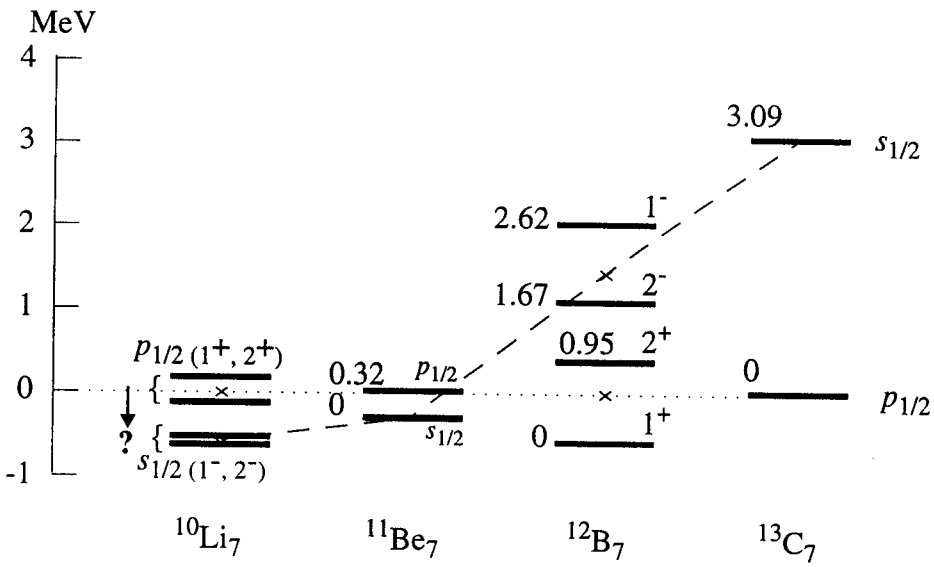

Figure 2.8: Competition between $s_{1/2}$ and $p_{1/2}$ levels among N=7 nuclei [Tal60]. The levels are shifted to match the lowest $p_{1/2}$ state. Extrapolation implies the non-normal parity ground state of ^{10}Li [Bar77].

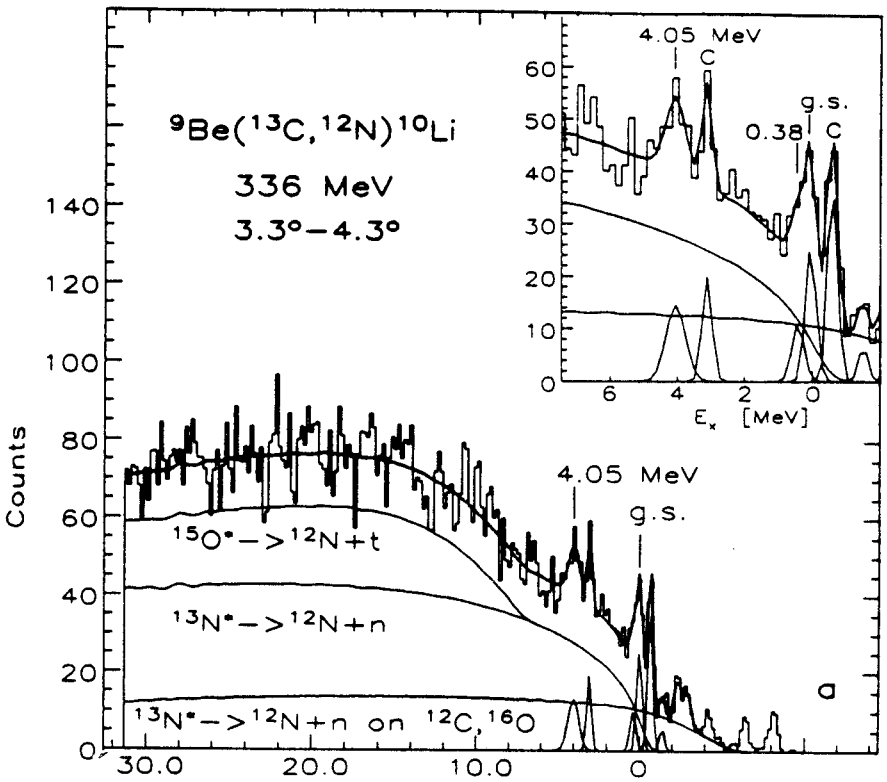

Figure 2.9: [Boh93] Energy spectra of ^{12}N from the reaction of ^{9}Be(^{13}C,^{12}N)^{10}Li by Bohlen *et al.* The ground state ($E_r = 0.42$ MeV) and the first excited state at $E_x = 0.38$ MeV ($E_r = 0.80$ MeV) are not completely resolved.

keV in ^{10}Li. Bohlen and collaborators [Boh93] used two different transfer reactions, ^{9}Be(^{13}C,^{12}N)^{10}Li at E_{Lab} = 336 MeV and ^{13}C(^{14}C,^{17}F)^{10}Li at E_{Lab} = 337 MeV, to study the states of ^{10}Li and concluded that $E_r = 0.42 \pm 0.05$ MeV, $\Gamma = 0.15 \pm 0.07$ MeV is the 1^+ ground state and $E_r = 0.80 \pm 0.06$ MeV, $\Gamma = 0.30 \pm 0.10$ MeV is the 2^+ first excited state. Young and collaborators [You94] observed a *p*-wave state at $E_r = 0.54 \pm 0.06$ MeV, $\Gamma = 0.36 \pm 0.02$ MeV using the reaction ^{11}B(^{7}Li,^{8}B)^{10}Li at E_{Lab} = 130 MeV. Evidence for a low-lying state in ^{10}Li was also seen at $E_r > 0.100$ MeV and $\Gamma < 0.23$ MeV.

Kryger *et al.* [Kry93] employed the method of sequential neutron decay spectroscopy (SNDS) at 0° and observed a central peak in the relative velocity spectrum of ^{9}Li + n coincidence events which indicates an existence of a low decay energy process (see Figure 2.11). ^{10}Li was created via fragmentation of an 80 MeV/nucleon ^{18}O beam on a 10 mg/cm^2 C target. The fragmentation products and the primary beam were separated from the

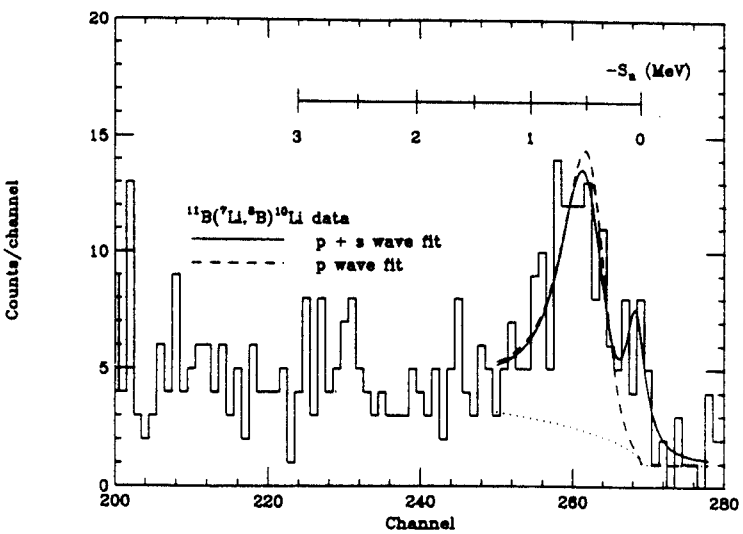

Figure 2.10: [You94] The energy spectrum from the transfer reaction ^{11}B(^{7}Li,^{8}B)^{10}Li by Young *et al.* It shows a strong evidence of the state at $E_r \approx 500$ keV.

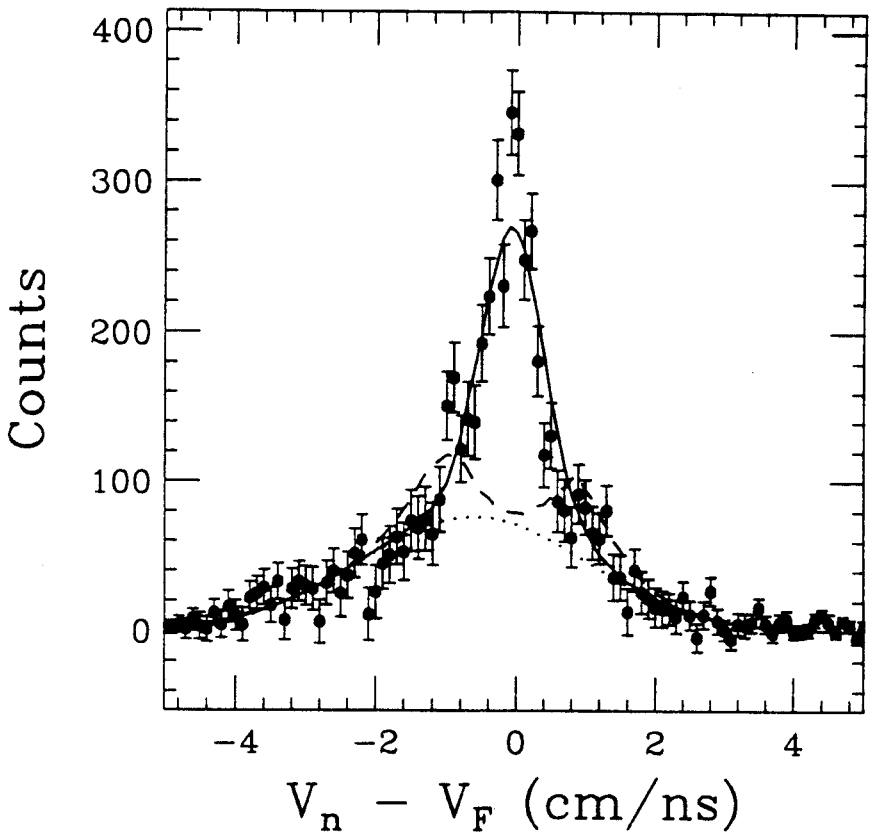

Figure 2.11: [Kry93] The relative velocity spectra of ^{9}Li + n coincidence events obtained with sequential neutron decay spectroscopy by Kryger *et al.* The dashed line is a simulated spectrum with the parameter by Wilcox *et al.* (E_r = 800 keV, l = 1) superimposed on the Gaussian background (dotted). The solid line is a simulated spectrum with the parameter by Amelin *et al.* (E_r = 150 keV, l = 0) plus the Gaussian background.

neutrons using a set of quadrupole magnets and a dipole magnet. The fragments and the neutrons were detected in coincidence. Since this method is only sensitive to the Q-value of the decay, the central peak in the spectrum could represent a decay from an excited state of ^{10}Li to an excited state of ^{9}Li, as well as a decay from the ground state of ^{10}Li to the ground state of ^{9}Li. Thus, this observation does not prove the existence of a low-lying s-wave state, however a limit on the decay parameters for each l (= 0 or 1) could be extracted assuming the central peak to originate from the decay to a ^{9}Li ground state. The results reported by Kryger *et al.* [Kry93] for the p-wave case were $E_r < 200$ keV for a width Γ_0 less than 500 keV and $E_r < 300$ keV for the width Γ_0 more than 500 keV and less than 1500 keV. For the s-wave case, $E_r < 300$ keV for the width Γ_0 less than 500 keV and $E_r <$ 450 keV for the width more than 500 keV and less than 1500 keV.

Zinser *et al.* [Zin95] used one nucleon stripping reactions of ^{11}Be and ^{11}Li to investigate the states of ^{10}Li. The secondary beams of 280 MeV/nucleon for ^{11}Li and 460 MeV for ^{11}Be on a 1.29 g/cm^2 carbon target were used for the reaction. The fragments were detected after a separation with a magnetic spectrometer. Neutrons were detected in coincidence with the fragments. The neutron data from the events $^{11}\mathrm{Be} + \mathrm{C} \rightarrow {}^{A}\mathrm{Z} + \mathrm{n} + \mathrm{X}$ and $^{11}\mathrm{Li} + \mathrm{C} \rightarrow {}^{9}\mathrm{Li} + \mathrm{n} + \mathrm{X}$ were selected and recorded as a distribution of the radial momentum p_r. Figure 2.12 shows the results of this experiment. As a first order approximation, the one proton stripping from the ^{10}Be core of the one neutron halo nucleus ^{11}Be most likely did not disturb the initial state of the s-wave halo neutron and it became an unbound neutron in ^{10}Li. Thus it was suggested that the ^{10}Li state seen by Kryger *et al.* and the narrow momentum distribution in the results were attributed to the s-wave neutrons in ^{10}Li. Also, one neutron stripping from the ^{11}Li beam, to create ^{10}Li, could be considered not to affect the ^{9}Li

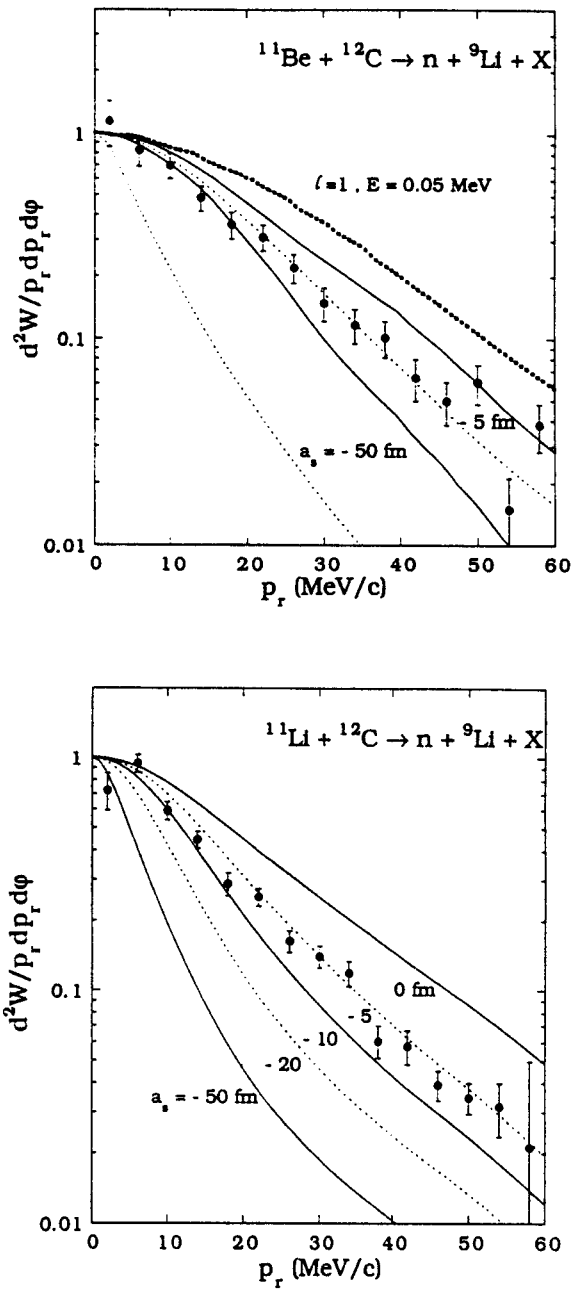

Figure 2.12: [Zin95] Radial momentum distributions of neutrons from ^{10}Li breakup reported by Zinser *et al.* ^{10}Li was created by one proton stripping from ^{11}Be (top) or by one neutron stripping from ^{11}Li (bottom). In the top figure, the top dotted line assumes an l = 1 resonance at 0.05 MeV. The two sets (a_s = -5 and -50 fm) of the calculations were shown with the ^{9}Li recoil widths σ_Q = 100 MeV/c (solid) and σ_Q = 0 MeV/c. In the bottom figure, two contributions were considered in the theoretical curves. One is diffraction (1/3 intensity) and the other is the intermediate state of ^{10}Li (2/3 intensity) which was assumed to be a pure *s* state.

core because of the weak binding between the halo neutron and the core. Thus it was very unlikely to excite the ^{9}Li core to the 2.7 MeV first excited state and the observed state must have been due to the ground state of ^{10}Li. The parameter Γ of a two-dimensional Lorentzian was used to parameterize the distribution, and the results from both ^{11}Be and ^{11}Li beams showed the same Γ = 36 MeV/c. The Woods-Saxon single-particle potential-well model was used for the fit and the depth of the *p* well was fixed to reproduce a resonance at 0.42 MeV [Boh93].

Ostrowski *et al.* (Figure 2.13) [Ost96] recently reported four states in ^{10}Li at E_r = 0.246 MeV, 1.458 MeV, 4.191 MeV, and 4.631 MeV and widths of Γ = 0.137 MeV, 0.107 MeV, 0.128 MeV, and 0.43 MeV, respectively. The ^{10}Be(^{12}C,^{12}N)^{10}Li was employed to populate the states of ^{10}Li. The energy of the ^{12}C beam was around 20~30 MeV/nucleon. A Breit-Wigner lineshape was used to fit the peaks in the spectra. The state reported by Bohlen *et al.* [Boh93] at E_r = 0.42 MeV was assumed to be the first excited state and the parameters were included in the process of fitting even if it was not clearly observed in the experimental spectrum (see Figure 2.13). The spins were assigned for the ground state (E_r = 0.24 MeV) and the first excited state (E_r = 0.42 MeV) to be 1^+ and 2^+, respectively, which were both the $\nu p_{1/2}$ configuration. Although the fitting parameter for the E_r = 0.42 MeV was taken from the Bohlen's result [Boh93], Ostrowski's result is contradicting from the Bohlen data, since the state at E_r = 0.8 MeV which was assigned to $J^{\pi} = 2^+$ in the Bohlen's report [Boh93] was not observed.

No defining parameters have been set for the ground state of ^{10}Li. The state at about 0.50 MeV with a *p*-wave emission reported by Bohlen *et al.* [Boh93] and Young *et al.* [You94] are at least in agreement, however the energies and/or angular momentum

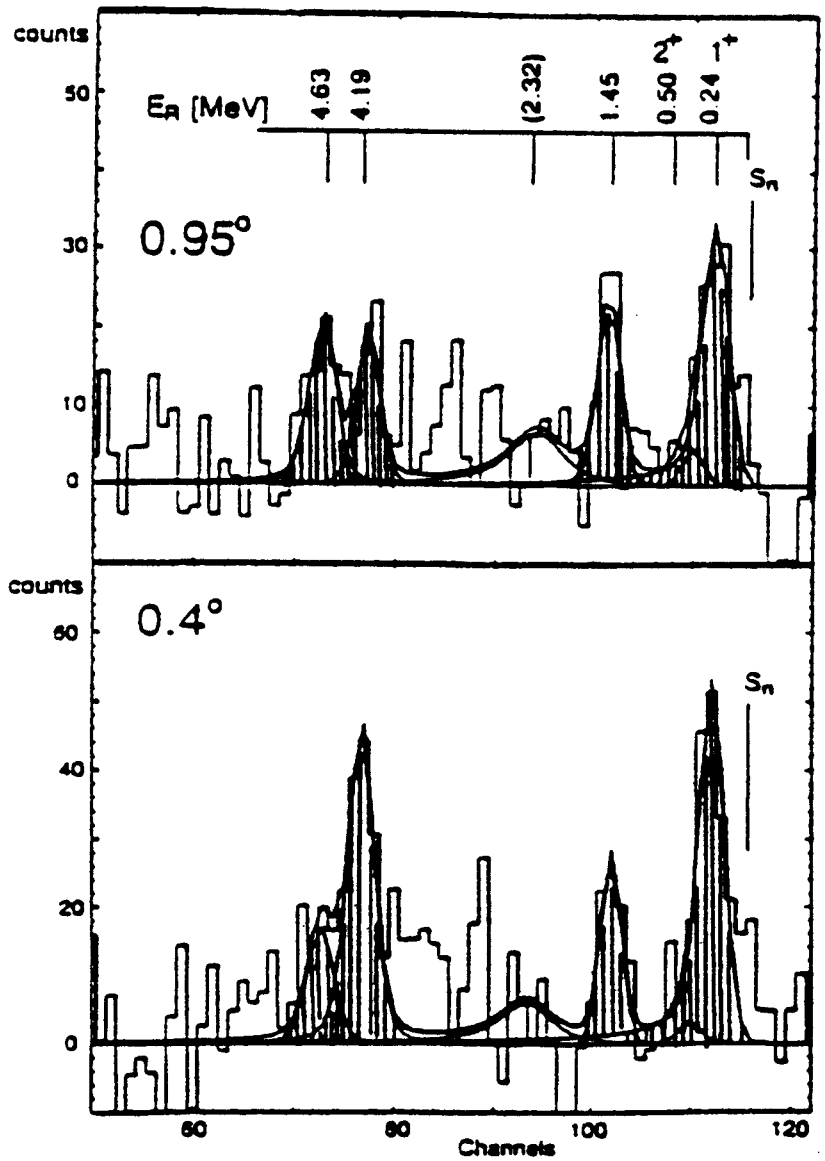

Figure 2.13: [Ost96] Spectra of the ^{10}Be(^{12}C,^{12}N)^{10}Li reaction by Ostrowski *et al.* Although the state reported by Bohlen *et al.* [Boh93] at E_r = 0.42 MeV was assumed to be there for fitting, it is not resolved from the ground state at E_r = 0.24 MeV. The state reported by Wilcox *et al.* at 0.8 MeV was not observed in these spectra.

assignments of the lower-lying state are still controversial.

2.4 ^{14}Be Three-Body Models and ^{13}Be Ground State

Similar to ^{11}Li, a ^{14}Be nucleus is considered to have a two neutron halo structure which consists of a ^{12}Be core and two weakly bound halo neutrons [Tho96]. The ground state of ^{13}Be has the same importance to the theoretical models of ^{14}Be as the structure of ^{10}Li does to the ^{11}Li three-body calculations [Tho96].

Ostrowski *et al.* [Ost92] performed an experiment to study ^{13}Be using the double-charge-exchange reaction ^{13}C(^{14}C,^{14}O)^{13}Be, E_{Lab} = 337.3 MeV. A highly enriched (98%) ^{13}C target as well as a ^{12}C target were used in the (^{14}C,^{14}O)-reaction. The ^{12}C target was used to calibrate and to determine the background. The states observed were at 2.01 MeV, 5.14 MeV, 8.53 MeV above ^{12}Be + n and Γ = 0.3 MeV, 0.4 MeV, 0.9 MeV, respectively. R-matrix calculations of the line width suggested the probable spin state for the lowest observed state to be $J^{\pi} = 5/2^{+}$ or $1/2^{-}$. A theoretical calculation by Poppelier *et al.* [Pop85] using the (0+1)$\hbar\omega$ shell-model, and a prediction by Lenske [Len91] using a Woods-Saxon potential with a density dependent pairing interaction, supported the $J^{\pi} = 5/2^{+}$ assignment for the state at 2.01 MeV. Although the latter calculation also predicted a low-lying $1/2^{+}$ ground state at around 0.9 MeV, it was not observed in this experiment. It was argued that the ground state was not observed in the spectrum, because of the low cross section of the $2s_{1/2}$ neutron-shell in multi-nucleon transfer reaction and the large *s*-state level width.

Penionzhkevich [Pen94] reported states in ^{13}Be using the ^{14}C(^{11}B,^{12}N)^{13}Be reaction. A new state at 0.9 MeV was observed as well as the previously reported state at 2.0 MeV.

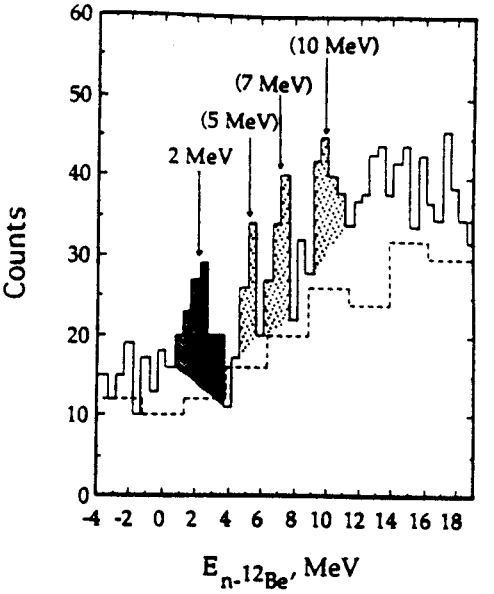

Figure 2.14: [Kor95] The proton spectrum from the reactions $CD^2(^{12}Be,p)$ (solid) and $C(^{12}Be,p)$ (dotted). The lowest state extracted reliably is at $E_r = 2$ MeV.

However, this ground state has not yet been confirmed by other experiments.

Korsheninnikov [Kor95] used a secondary beam of ^{12}Be from an ^{18}O primary beam on a 5 mg/cm^2 thick CD_2 target to study the states in ^{13}Be populated via the neutron transfer reaction $d(^{12}Be,p)$. Figure 2.14 shows the results obtained in this experiment which exhibits clear evidence for the known 2 MeV state as well as states at 5 MeV, 7 MeV, and 10 MeV above the neutron decay threshold. However, background due to the carbon in the target (dotted line in the figure) did not allow for a reliable measurement in the low-energy region of the spectrum.

Descouvemont [Des94] performed a ^{12}Be + n microscopic cluster model calculation for ^{13}Be. The Volkov force [Vol65] V2 and V4 were used for the nuclear part of the nucleon-nucleon interaction. The result of the calculations showed the existence of a slightly bound low-lying $1/2^+$ state at E = -9 keV for V2 and at E = -38 keV for V4, which are both

lower than the $5/2^+$ state (E = 2.01 MeV) reported by Ostrowski *et al* [Ost92]. It suggests that the inversion of $vd5/2^+$ and $vs1/2^+$ occurs.

As in the ^{11}Li [Tho94] case, Thompson and Zhukov [Tho96] performed similar three-body calculations of ^{14}Be. While the simple shell model predicts a $\nu(1d_{5/2})^2$ configuration for the ground state of ^{14}Be, an admixture of $\nu(s_{1/2})^2$ and $\nu(d_{5/2})^2$ configurations were assumed and the neutron-core interaction potentials for both $s_{1/2}$ and $d_{5/2}$ was considered. First, it was shown that a d-wave state at 2.1 MeV on ^{13}Be alone did not lead to the bound ^{14}Be nucleus which contradicted the experimental result (bound by 1.34 MeV [Aud93]). Among several combinations of the $2s$ and $1d$ neutron resonances, only a combination of a $2s$ virtual state with a large scattering length ($a_s \approx$ -130 fm) and another d-wave state at $E \approx$ 1.3 MeV which was lower than the known 2.1 MeV d-wave state, reproduced the experimental values of the two neutron binding energy and the matter radius of the ^{14}Be, simultaneously. More experimental results are awaited to confirm the low-lying structure of the ^{13}Be as an important step in the ^{14}Be three-body calculation.

Chapter 3

Experimental Details

3.1 Experimental Method

The primary goal of the present work was to determine the ground state energy of ^{10}Li. The technique of sequential neutron decay spectroscopy [Deá87] (SNDS) was employed to fragmentation products produced near 0°. Figure 3.1 shows a kinematic diagram of the ^{10}Li $\rightarrow$ ^{9}Li + n decay. If a ^{10}Li nucleus is produced by fragmentation, it initially has a non-zero

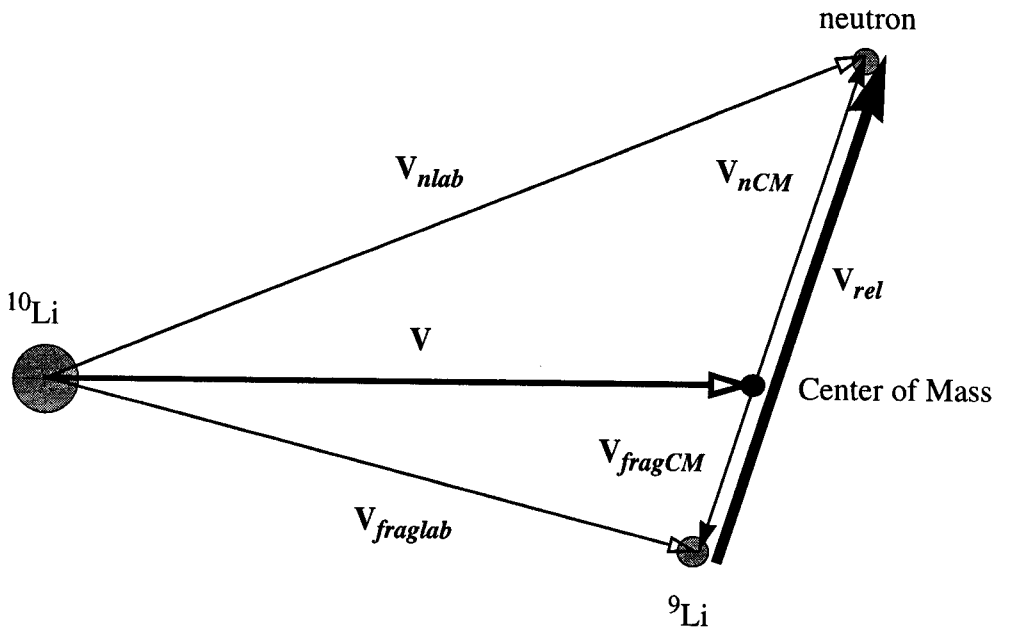

Figure 3.1: Kinematic diagram of the sequential neutron spectroscopy for the ^{10}Li decay.

momentum. **V** is the initial velocity vector of the ^{10}Li created by fragmentation in the laboratory system. ^{10}Li is a neutron unbound nuclei and has a very short lifetime (~ 10^{-21} s), thus if the initial velocity is at ~40% of speed of light (0.4c ≈ 12 cm/ns), one can assume that the decay, $^{10}\text{Li} \rightarrow {}^{9}\text{Li} + \text{n}$ is instantaneous since it can travel only ~1.3 x 10^{-12} m compared to the flight path (~ 5 m). The velocity vectors of the decay products neutron and ^{9}Li are $\mathbf{V}_{nlab}$ and $\mathbf{V}_{fraglab}$ in the laboratory system. $\mathbf{V}_{nCM}$ and $\mathbf{V}_{fragCM}$ are the velocity vectors of the neutron and the ^{9}Li nucleus in the center of mass system. Conservation of energy in the centre of mass system yields,

$$m_{^{10}\text{Li}}c^2 = m_{^{9}\text{Li}}c^2 + m_n c^2 + T_{^{9}\text{Li}} + T_n \tag{3.3}$$

where c is the velocity of light, m_x represent the rest masses of each particle, and T_x is the kinetic energy of each particle in the center of mass system. The kinetic energies are related to the decay energy (E_r) via:

$$E_r = T_{^{9}\text{Li}} + T_n \tag{3.4}$$

For a two particles system, we can write,

$$E_r = \frac{1}{2}\mu V_{rel}^2 \tag{3.5}$$

where μ is the reduced mass of the system and V_{rel} is the magnitude of the relative velocity vector between the neutron and ^{9}Li. Using the relationship given in Figure 3.1, we get:

$$\mathbf{V}_{rel} = \mathbf{V}_{nCM} - \mathbf{V}_{fragCM} \tag{3.6}$$

$$\mathbf{V}_{nCM} - \mathbf{V}_{fragCM} = \mathbf{V}_{nlab} - \mathbf{V}_{fraglab} \tag{3.7}$$

If the decay direction is nearly parallel to the center of mass velocity, Equation (3.6) and (3.7) can be written with a scalar relationship,

$$V_{rel} = V_{nlab} - V_{fraglab} \tag{3.8}$$

where V_{nlab} and $V_{fraglab}$ are the magnitude of the corresponding vectors.

During the actual data analysis, the relative velocity spectrum was obtained from the velocity information of the ^{9}Li and the neutrons. This information was then compared to Monte Carlo simulations to extract the mass of ^{10}Li.

3.2 Mechanical Setup

The experiment was performed at the National Superconducting Cyclotron Laboratory (NSCL). Figure 3.2 shows a floor plan of the NSCL. An ^{18}O beam with a kinetic energy of 80 MeV / nucleon was provided from the K1200 cyclotron. The primary beam bombarded a 94 mg / cm^2 thick ^{9}Be target located in front of the last quadrupole-dipole magnet combination in the beam transport system of the NSCL. Fragmentation in the target created various nuclei. Table 3.1 shows a example of a prediction of fragmentation products by the code INTENSITY [Win92] for the present case. Since the INTENSITY calculation does not include unbound nuclei, ^{10}Li is not included in Table 3.1. Figure 3.3 shows the schematic of the experimental setup. The ^{10}Li nuclei break up immediately after their creation in the target into one neutron and a ^{9}Li fragment. The dipole magnet was used to bend the primary beam and the fragments, respectively, away from the straight flight path of the neutrons into two properly adjusted separate beamlines. The first one at 11° was for the fragments and had a telescope detector array at the end. The primary beam then bent into the 14° beamline and was collected in a shielded Faraday cup at a distance of ~ 25 m to reduce the background. The neutrons from the breakup were detected by a liquid scintillator array located ~ 5.8 m down stream at 0°. The neutrons were extremely forward

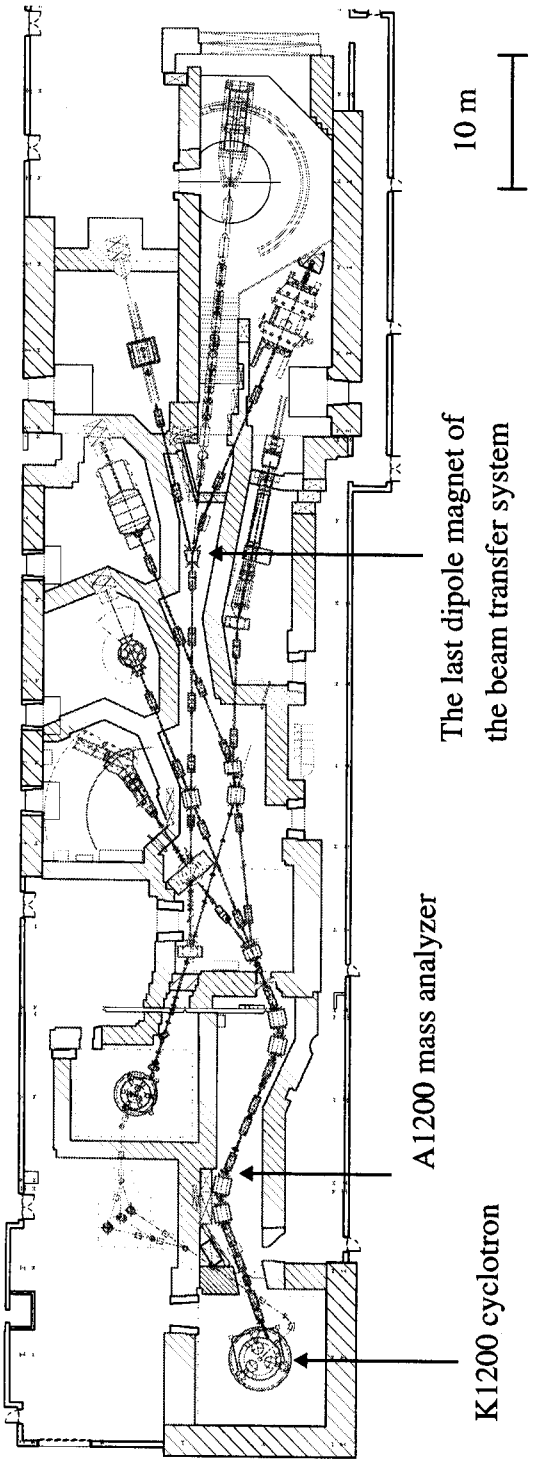

Figure 3.2: Floor plan of the National Superconducting Cyclotron Laboratory.

Table 3.1: A example of an output file of the INTENSITY [Win92] calculation for an 80 MeV/nucleon ^{18}O beam (intensity = 10 pnA) with a 94 mg/cm^2 ^{9}Be Target.

Fragment (charge)	B-rho [Tm]	Energy [MeV/A]	Rate [#/s]
^{3}He(2+)	1.8448	70.320	3449
^{4}He(2+)	2.4620	70.441	10734
^{6}He(2+)	3.6962	70.561	4368
^{8}He(2+)	4.9305	70.621	42
^{6}Li(3+)	2.4587	70.260	26191
^{7}Li(3+)	2.8701	70.337	27933
^{8}Li(3+)	3.2816	70.396	11892
^{9}Li(3+)	3.6930	70.441	2147
^{11}Li(3+)	4.6118	73.424	7
^{7}Be(4+)	2.1468	69.973	18431
^{9}Be(4+)	2.7640	70.158	63463
^{10}Be(4+)	3.1089	71.833	33108
^{11}Be(4+)	3.4534	73.201	7810
^{12}Be(4+)	3.7976	74.340	891
^{14}Be(4+)	4.4856	76.127	2
^{8}B (5+)	1.9583	69.664	3940
^{10}B (5+)	2.4813	71.510	103566
^{11}B (5+)	2.7570	72.912	147398
^{12}B (5+)	3.0326	74.079	95884
^{13}B (5+)	3.3079	75.064	30550
^{14}B (5+)	3.5831	75.908	5137
^{15}B (5+)	3.8582	76.638	495
^{9}C (6+)	1.8315	69.340	254
^{10}C (6+)	2.0618	71.112	5530
^{11}C (6+)	2.2917	72.556	48809
^{12}C (6+)	2.5214	73.756	185978
^{13}C (6+)	2.7510	74.770	326916
^{14}C (6+)	2.9804	75.637	284789
^{15}C (6+)	3.2097	76.388	133050
^{16}C (6+)	3.4389	77.043	35185
^{17}C (6+)	3.6681	77.622	372
^{12}N (7+)	2.1554	73.373	6501
^{13}N (7+)	2.3522	74.420	64781
^{14}N (7+)	2.5490	75.315	300347
^{15}N (7+)	2.7456	76.090	698891
^{16}N (7+)	2.9421	76.767	897715
^{17}N (7+)	3.1386	77.363	692143
^{18}N (7+)	3.3350	77.892	15899
^{19}N (7+)	3.5314	78.365	120

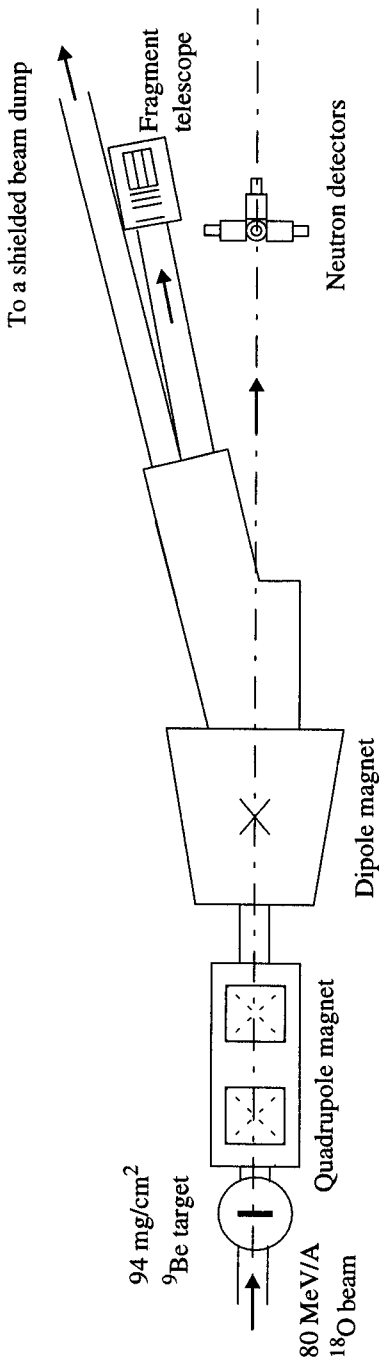

Figure 3.3: Top view of the experimental setup.

focused due to the high primary beam energy. ^{9}Li fragments were detected in coincidence with the neutrons at the end of beam pipe bent by 11° with respect to the central neutron fright path. The fragment flight path distance from the target to the fragment telescope was ~ 6.0 m. The quadrupole magnets and the dipole magnet were tuned to optimize the detection rate of ^{9}Li and other charged nuclei with a mass-to-charge ratio equal to three (^{6}He, ^{12}Be, ^{15}B).

The detector system and the signal processing electronics are described in the following sections.

3.3 Neutron Detectors

Five liquid scintillator (NE213) detectors were used to detect the neutrons. Each neutron detector had a cylindrical shape, and Figure 3.4 (a) shows their dimensions. Figure 3.4 (b) shows the arrangement of five detectors.

The intrinsic efficiency of the neutron detectors was energy dependent. It was estimated with the code KSUEFF [Cec79] and the result is shown in Figure 3.5. The efficiency over the energy range of the current experiment is ~10%.

The solid angle coverage of the neutron detectors in the laboratory was 1.15 msr. However neutrons from the breakup were forward focused and the solid angle coverage of the detectors in the center of mass frame of the neutron decay system was much higher than in the laboratory frame because of the high incident energy of the primary beam. In the case of the ^{10}Li breakup, the solid angle coverage of the neutrons in the center of mass frame of a neutron and a ^{9}Li is 100% of 4π up to decay energy of $E_r \approx 18$ keV decreasing to 0.8% of 4π at decay energy of $E_r \approx 1000$ keV.

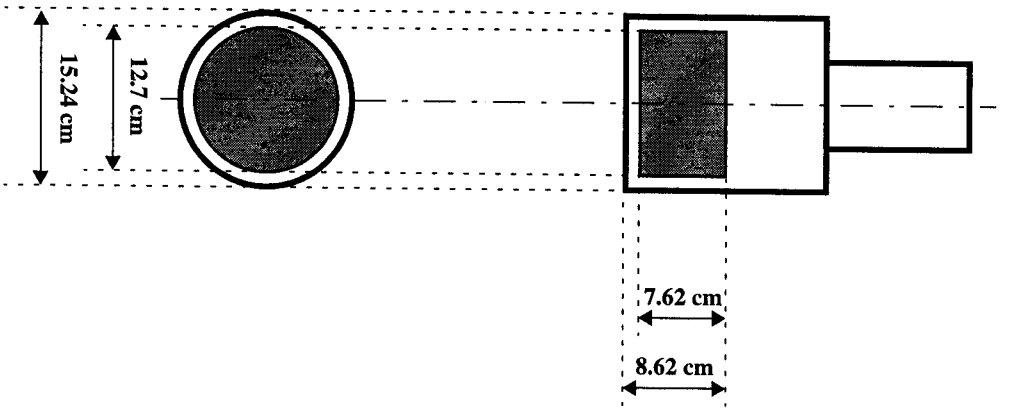

(a) Neutron detector dimension

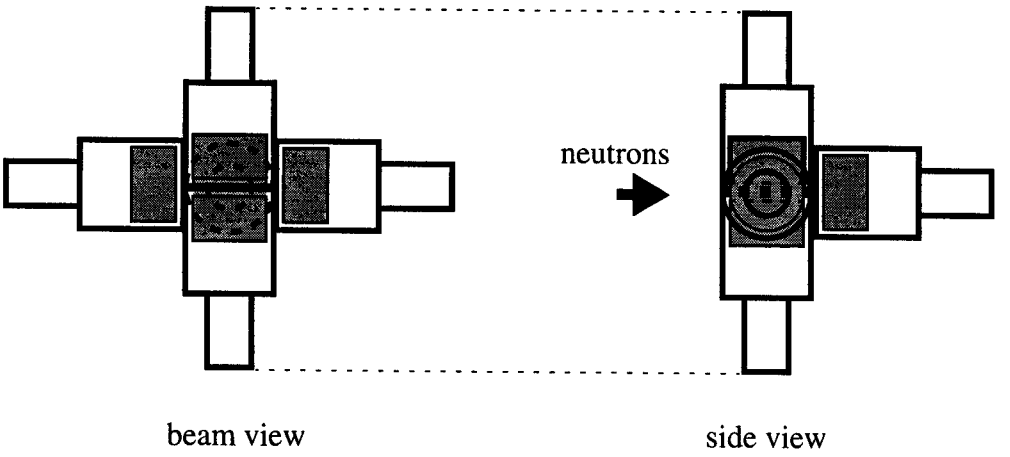

(b) Neutron detector array configuration

Figure 3.4: The dimensions of one neutron detector and the configuration of the whole detector array. The gray area shows the neutron sensitive part.

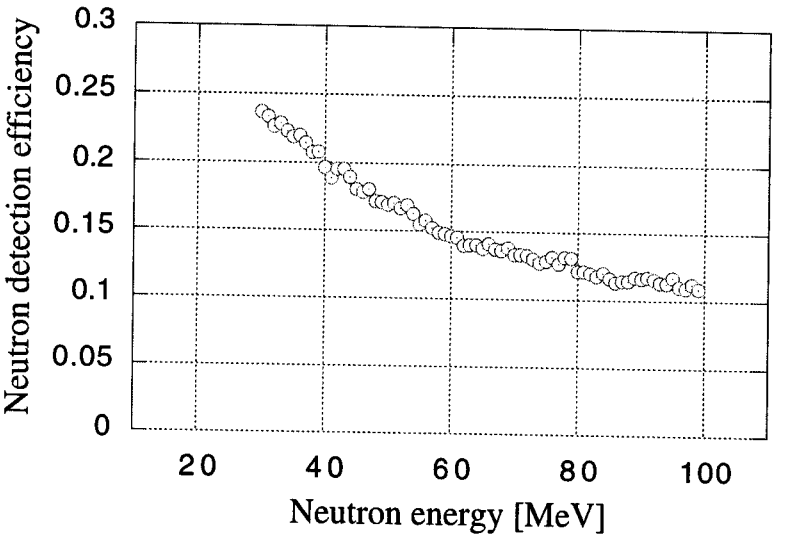

Figure 3.5: Simulated efficiency curve of the neutron detector with a sideway geometry. It was calculated with the code KSUEFF [Cec79].

There was a geometrical constraint on the location of the neutron detectors by the iron core aperture of the dipole magnet. The configuration of the neutron detectors were chosen to maximize the coverage of the solid angle of this window. The sensitive part of the neutron detectors covered 76% of the window area.

The energy dependent solid angle coverage in the center of mass and the energy dependent intrinsic efficiency were folded with the fragment acceptance (see Chapter 4) and obtained as an efficiency plot by the simulation code (see Chapter 4). Figure 3.6 shows the folded neutron efficiency curve for ^{10}Li decay in the form of the relative velocity spectrum.

3.4 Fragment Telescope

The fragment telescope consists of a fast plastic timing detector, three fourfold segmented silicon ΔE detectors, and nine CsI(Tl) scintillator crystals with a photo diode readout for

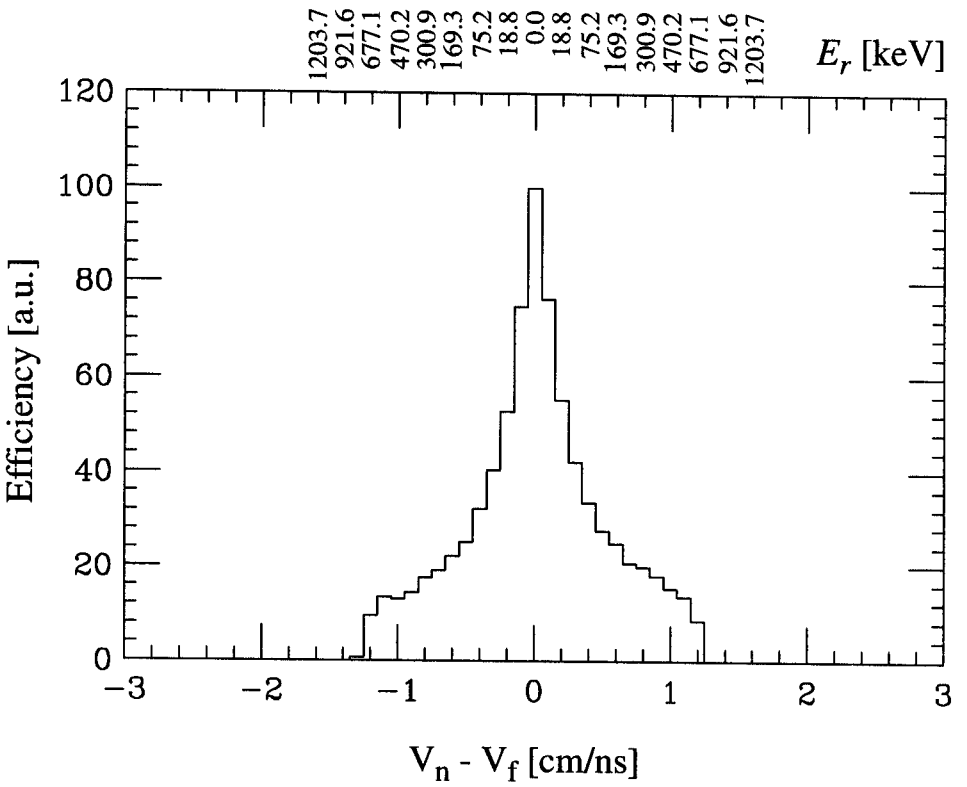

Figure 3.6: Efficiency plot of the neutron detection for the ^{10}Li neutron decay for the decay energy range of 0.00 MeV < E_r < 1.00 MeV. The energy dependent solid angle coverage of the neutron detectors, the energy dependent neutron detector efficiency, and fragment detector acceptance are folded as a total neutron detection efficiency. The upper abscissa indicates a corresponding decay energy.

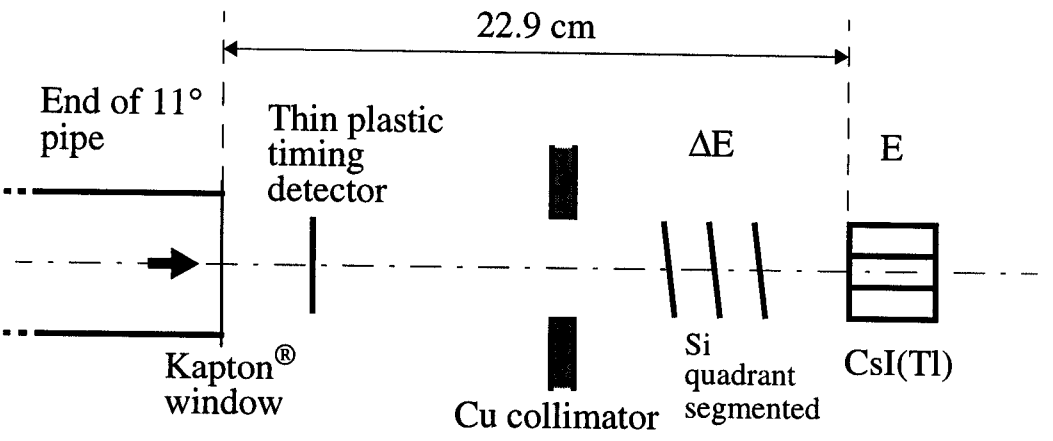

Figure 3.7: Schematic of the fragment telescope.

each of the crystals. Figure 3.7 shows the schematics of the telescope. The end of the 11° beamline was sealed with a 0.0279 mm thick Kapton® window and the telescope was operated in air.

The thin plastic timing detector consisted of a 0.0254mm thick fast scintillating plastic foil (BC400, Bicron Corp.) with a plexi glass light guide frame coupled to a photomultiplier tube.

A copper collimator was placed after the timing detector. With a thickness of 2.54 cm it left a square opening of 5.0 cm x 5.0 cm. It was placed in front of the ΔE and E detectors to eliminate events which were glazed or reflected from the beamline pipe. It also allowed to maximize the good event rate in the ΔE and E detectors during the tuning of the magnets.

Three quadrant segmented Si detectors were used to measure the energy loss. They were located at a distance of 12 cm behind the timing detector. They had an effective area

of 5 cm x 5 cm and an effective thickness of 1016 μm (ΔE1), 486 μm (ΔE2), and 478 μm (ΔE3), separately (Figure 3.8). The detectors were tilted by 7° with respect to the central fragment trajectory in order to avoid 'channelling' of the fragments in the crystal layers. Three detectors were used to get a sufficient isotope separation for the Beryllium fragments, ^{10}Be,^{11}Be, and ^{12}Be in the ΔE - E plot by adding up the individual energy loss pulse heights.

Nine 1.7 cm x 1.7 cm x 5.0 cm CsI(Tl) detectors were used to stop and detect the total energy of the fragments (Figure 3.9). Each of them was wrapped with white reflective blotter paper (HATF10710, Millipore Corp.) on the long sides and the polished front face was covered with a 1.5 μm thick aluminized Mylar® foil. The thickness of the aluminum layer was less than 0.1 μm. Photo diodes (S3590-03, HAMAMATSU) were attached with silicone rubber glue (RTV615, GE) at the back end of each crystal and covered with white

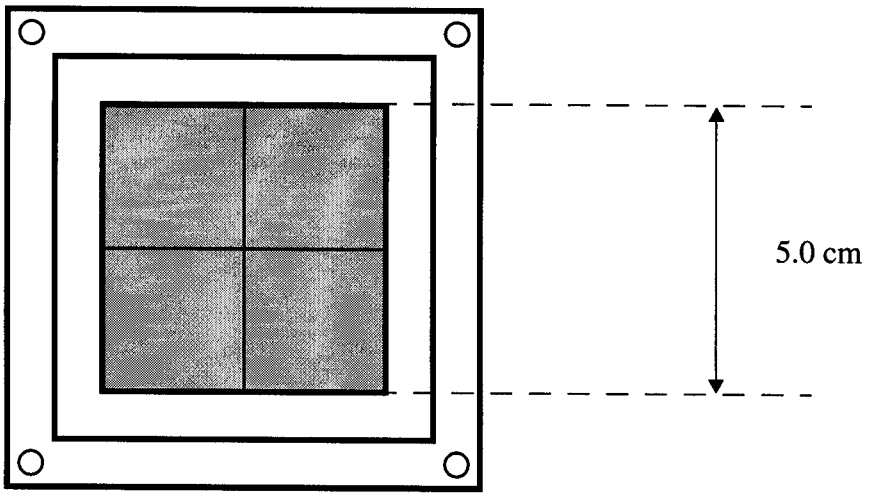

Figure 3.8: Front view of one of the ΔE Si detectors. The gray area shows the sensitive region. The crossed lines on the gray area indicates the segmentation lines.

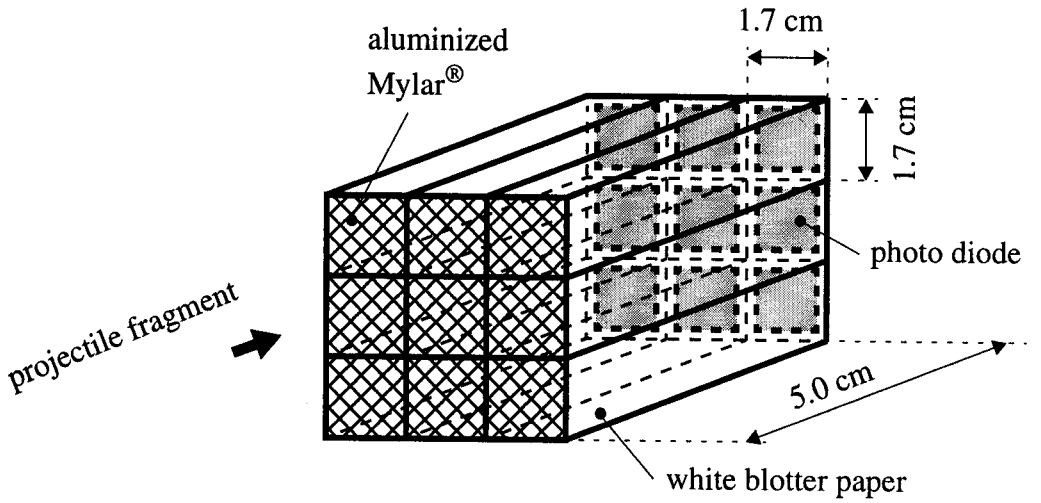

Figure 3.9: Structure of CsI(Tl) E detector array. Each of the nine crystals were wrapped with white blotter paper independently to optically isolate them from each other.

Teflon® tape for light sealing and for improving light reflection.

3.5 Electronics and Data Acquisition

Figure 3.10 displays the schematics of the electronics used for the signal processing. The photo diodes attached to the CsI(Tl) crystals E detector had a full depletion voltage of 70 Volts and a maximum voltage of 100 Volts. They were reversely biased with 80 Volt through the preamplifiers. The signal picked up by the preamplifier was passed to the linear amplifier with a 3 μs shaping time. The peak height of the outputs of the linear amplifiers was proportional to the kinetic energy of the detected projectile fragment. These energy signals were recorded with a peak sensitive ADC (AD811, ORTEC). The fast time signal outputs of the linear amplifier were sent to Constant Fraction Discriminators (CFD: TC455, TENNELEC) to create TDC stop signals relative to the K1200 cyclotron RF time and to

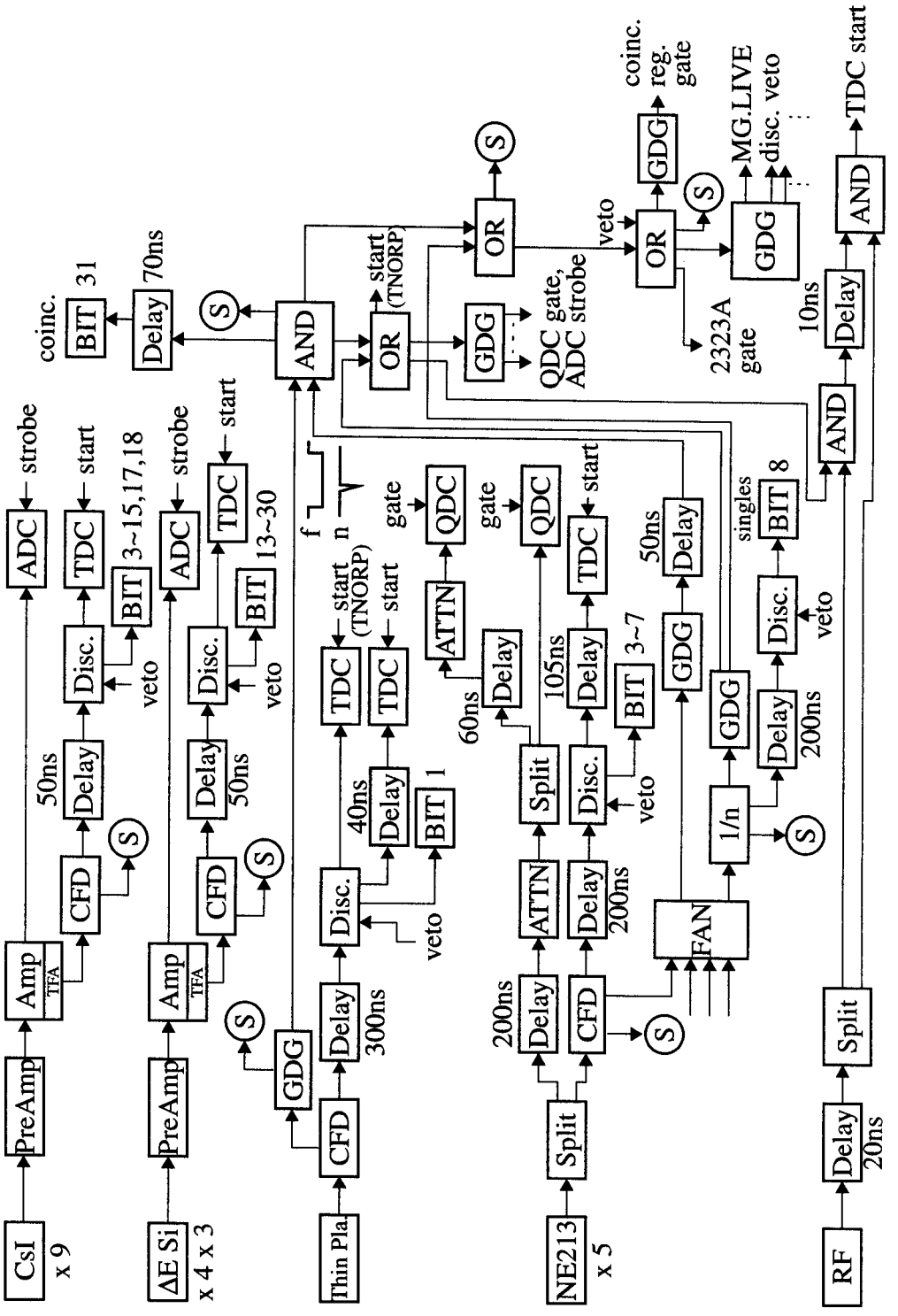

Figure 3.10: Diagram of the electronics.

create a bit for each E signal.

Basically the same signal processing was used to operate the three quadrant ΔE Si detectors. The shaping time of the linear amplifiers was set to 1 μs for the ΔE detectors. ΔE1, ΔE2, and ΔE3 detectors were biased with 90 Volts, 30 Volts, and 42 Volts, respectively.

The fast plastic timing scintillator was attached to a photomultiplier tube. The signal from the tube was fed to a CFD, and one of the outputs was used as part of the fragment - neutron coincidence condition. The pulse width of the CFD output for the fast plastic timing detector signal, which was fed to the coincidence AND, was ~ 200 ns. The other outputs of the CFD were used to set a bit for each event detected in the fast plastic detector and to generate a stop signal for a TDC to measure the time of flight relative to the cyclotron RF and the neutron time signal, respectively.

The neutron liquid scintillator detectors were also equipped with photomultiplier tubes. The signals from the tubes were split into an energy and time branch. The energy signal from each detector was integrated in two separate charge sensitive ADC (QDC) channels. Two differently gated signal charge integrations (tail and total) were necessary to achieve pulse shape discrimination between γ-rays and neutrons. Details of this technique will be discussed in Chapter 4. In the time branch, the signal from the neutron detectors were sent to a CFD and created time signals. They were passed to TDC stops and bits for each neutron detector as well as a bit for downscaled neutron singles. A short (~ 5 ns) signal was also created from the time signals and was fed to the neutron-fragment coincidence AND. Since it was much shorter than the other coincidence condition signal from the thin fast plastic detector (~ 200 ns), time of the neutron - fragment coincidence signals was dominated by the neutron time. The downscaled singles formed one event type of the master gate, togeth-

er with the main event type of coincidence events.

The RF time signal from the K1200 cyclotron was used as a time reference. The original RF signal had a sinusoidal shape and a frequency of 18.4 MHz, leading to repeated beam bursts at $\Delta t = 54.4$ ns. The RF signal was used to start all of the TDCs except the TDC for the TNORP (see 4.2.3) signals, in coincidence with a "master gate" signal consisting of the neutron singles and neutron-fragment coincidences. A veto signal blocked the data acquisition during the busy time of the frontend processor.

Finally, accepted events were written to 8 mm tapes and analyzed online, using the standard NSCL data acquisition system [Fox89, Fox92].

Chapter 4

Data Analysis

4.1 Overview

The off-line analysis of the data was performed with the NSCL data analysis program SARA [Fox89, Fox92]. The experiment consisted of four parts. First, fragment singles were recorded for energy calibration of the E detectors and gain matching of ΔE detectors. The second part included neutron singles runs for gain matching of the neutron detectors and calibration of the neutron times. In the third part, coincidence events of neutrons and fragments were measured to obtain the relative velocity spectra. For the forth part, shadow bar runs were conducted to measure the neutron background. The calibration of the energies (E), energy losses (ΔE), and time of flights (TOF) were performed off-line. Subsequently, calibrated ΔE-E particle identification (PID) histograms were created. Software gates were drawn for three different elements (He, Li, and Be) on the ΔE-E particle identification (PID) plot and the data was filtered into three sets based on these gates. Individual isotope (^{6}He, ^{9}Li, and ^{12}Be) gates were obtained from the filtered data using both the ΔE-E and the ΔE-TOF plot. Neutrons were separated from γ-rays by pulse shape discrimination technique (see section 4.3.1). A relative velocity spectrum of ^{7}He → ^{6}He + n was created from the filtered data. The neutron decay energy and the width of ^{7}He are well known

[Ajz88] and thus could be used as a calibration reaction. The time zero constants for the neutron TOF of each neutron detector in the data analysis code were adjusted to match the centers of the spectra with the simulations. The relative velocity spectra of $^{10}Li \rightarrow {}^{9}Li + n$ and $^{13}Be \rightarrow {}^{12}Be + n$ were then obtained from the filtered data and compared to the Monte Carlo simulations to extract the decay energies and the widths.

4.2 Calibration of Detectors

4.2.1 Calibration of the Fragment Telescope

The resolution of the E detectors was crucial because the energy information of the fragments was used to calculate the fragment velocity and also indirectly the neutron velocity. For the energy calibration of the CsI(Tl) energy detectors and the gain matching of an energy loss in the Si quadrant segmented detectors, calibration beams of isotopes with mass-to-charge ratio equal to three (^{6}He, ^{9}Li, and ^{12}Be) were used. The calibration beams were

Table 4.1: Calibration beam energies for different target thicknesses.

^{27}Al target thickness [mg/cm^2]	Bρ [T•m]	Kinetic energy of a fragment [MeV]		
		^{6}He	^{9}Li	^{12}Be
370	3.797	445.8	668.7	891.6
247	3.834	454.2	681.4	908.5
177	3.865	461.5	692.2	922.9
81	3.909	471.6	707.4	943.2
33	3.929	476.1	714.2	952.2
3.4	3.941	479.1	718.6	958.2

created by fragmentation of a primary ^{18}O beam with a kinetic energy of 80 MeV/nucleon on various Al targets. The A1200 mass analyzer was used to separate isotopes with mass-to-charge ratio equal to three. A momentum slit located at image1 in the A1200 was used to limit the momentum spread of the calibration beam to 0.25% (FWHM) and 1.0% (FWHM). This corresponds to 0.5% (FWHM) and 2.0% (FWHM) spread in energy.

Six ^{27}Al targets with different thicknesses were used to produce six different energies of calibration beams. The magnetic rigidities (Bρ) of the secondary beam were calculated using the code INTENSITY [Win92]. The different ^{27}Al target thicknesses, the Bρs of the A1200 mass analyzer, and corresponding total kinetic energies of the fragments of the calibration beam are shown in Table 4.1. The total kinetic energy of the calibration beam was calculated using the relation between kinetic energy T [MeV], mass number of the nucleus A, atomic number of the nucleus Z, and Bρ [T-m],

$$T = A\sqrt{u^2 + \left(B\rho\frac{299.7925Z}{A}\right)^2} - uA \qquad (4.1)$$

where

$$u = 931.49432 \text{ [MeV]}. \qquad (4.2)$$

Two-dimensional histograms of the fragment energy loss versus the fragment time of flight which was measured between the cyclotron RF and a thin plastic timing detector (ΔE1,2,3 vs. TOF), and the fragment energy loss versus the fragment total energy (ΔE1,2,3 vs. E) were created from the data to identify the isotopes in the calibration beam. Examples are shown in Figure 4.1 and Figure 4.2. For the ΔE detectors, the number of charge carriers created within a detector of small thickness Δx is proportional to the specific energy loss dE/dx and Δx [Kno89]. The specific energy loss of nonrelativisitic charged particles of mass m and charge Ze is expressed in Bethe's formula:

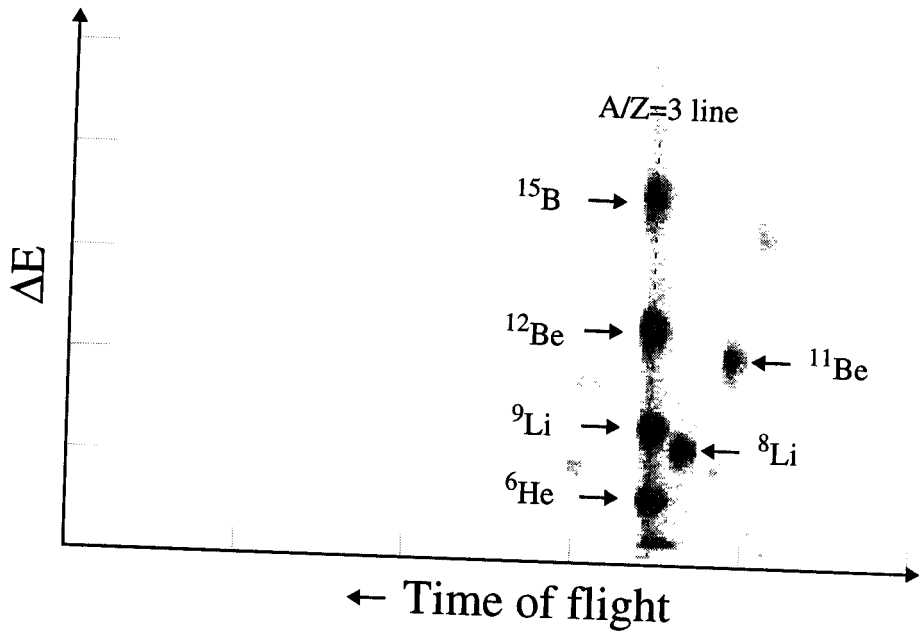

Figure 4.1 Two dimensional histogram of energy loss in the ΔE2 detector's quadrant number 1 versus time of flight of the fragments. m/q = isotopes are selected using the A1200 mass analyzer.

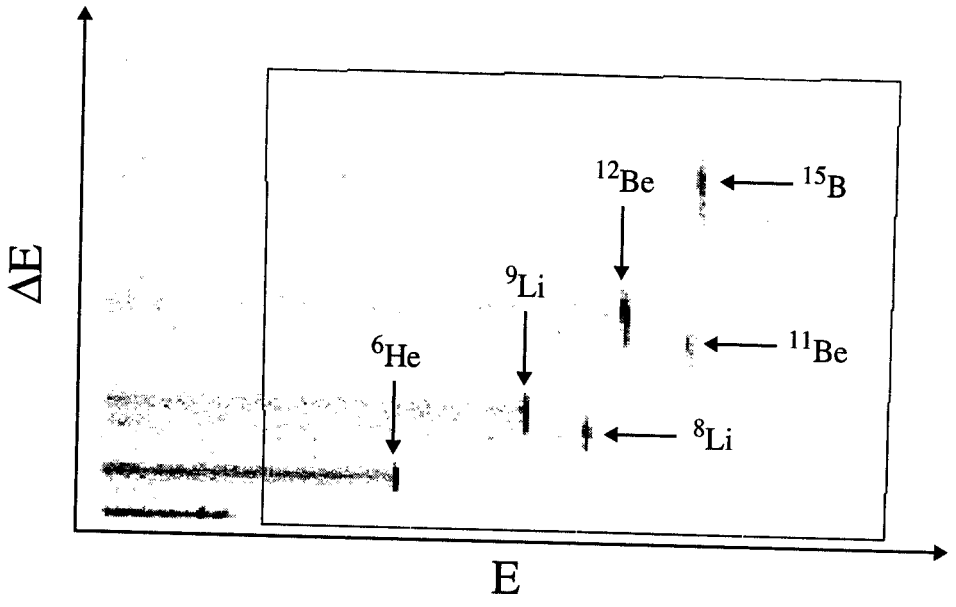

Figure 4.2: Two dimensional histogram of energy loss in the ΔE2 detector's quadrant number 1 versus total energy in the E3 detector of the fragments. The large square gate in the plot was applied to select the valid signal for a projection.

$$\frac{dE}{dx} = C_1 \frac{mZ^2}{E} \ln C_2 \frac{E}{m} \tag{4.3}$$

where C_1 and C_2 are constants. It shows that the energy loss is very sensitive to the mZ^2 value but only mildly dependent on the particle energy E. For the E detectors, it is obvious that the number of charge carriers created within a detector is proportional to the total kinetic energy E of the incident charged particles. This different dependence of the signal in the ΔE and E detectors allowed the isotope separation.

The A1200 selects isotopes according to their momentum over charge ratio. The force F_{MAG} on a charge q moving with velocity v in magnetic flux B is,

$$F_{MAG} = qvB \tag{4.4}$$

where F_{MAG}, v, and B are all perpendicular to each other. This charged particle moves along the circular trajectory with a radius ρ because of this force and the centripetal force F_{cen} of circular motion can be expressed in the form:

$$F_{cen} = \frac{mv^2}{\rho}. \tag{4.5}$$

Since $F_{MAG} = F_{cen}$,

$$qvB = \frac{mv^2}{\rho} \tag{4.6}$$

which leads to

$$B\rho = \frac{mv}{q} = \frac{p}{q}. \tag{4.7}$$

The centroid of the velocity distributions are equal for all the isotopes in a secondary beam. For a given Bρ value of the A1200 isotopes with the same mass-to-charge ratio m/q have the same velocities v. For example, isotopes with m/q = 3 were selected and they all had the same time of flight (the same velocities v) as shown in Figure 4.1.

In the figure, some isotopes with m/q ≠ 3 are also observed (^{8}Li, ^{11}Be, etc.). In the ^{8}Li case, the mass number is 1 less than the chosen m/q = 3 groups. From Equation 4.7, the

velocity v of ^{8}Li has to be greater than the chosen group to yield the same Bρ to be selected. ^{8}Li was observed in Figure 4.1 at the shorter time of flight (higher velocity v) side than ^{9}Li. The energy of those particles are expressed as $E = p^2/2m$ and as can be seen in Figure 4.2, ^{8}Li has larger energy since the selected ^{8}Li group has lower mass number than ^{9}Li and the same momentum as ^{9}Li.

A projection of the two dimensional gates on $m/q = 3$ isotopes on the E axis is shown in Figure 4.3. The location of the peaks for each isotopes for the six different energies were fitted quadratically by a least square method as a function of the kinetic energy of the calibration beams to extract calibration constants for ^{6}He, ^{9}Li, and ^{12}Be isotopes, individually. The energy resolution of the E detectors was ~ 0.5% (FWHM). These fits are shown in Figure 4.4, 4.5, and 4.6 (^{6}He, ^{9}Li, and ^{12}Be). The energy detector E2 showed an abnormal behavior and it was thus omitted from the later data analysis.

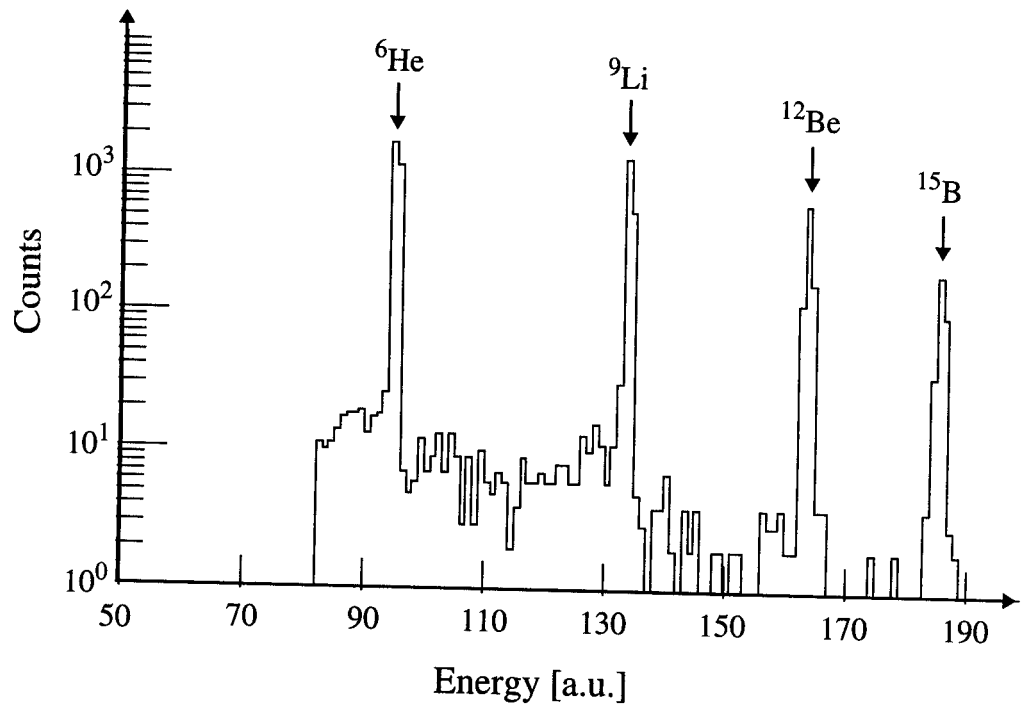

Figure 4.3: Energy spectrum of the calibration beam with an A/Z=3 gate.

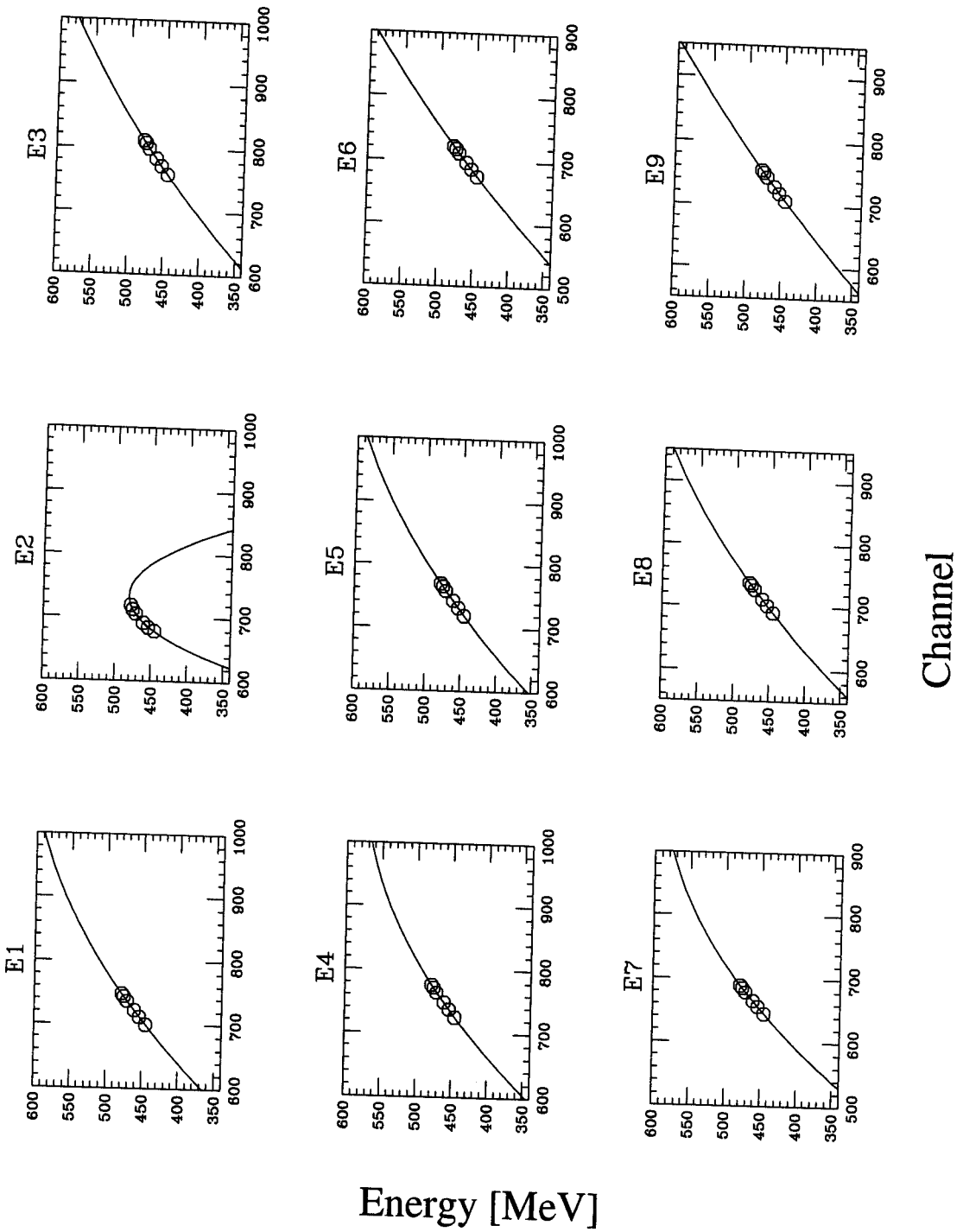

Figure 4.4: Quadratic fitting for energy calibration of the ^{6}He fragment for each E detector. The E2 detector was omitted due to its nonlinear behavior.

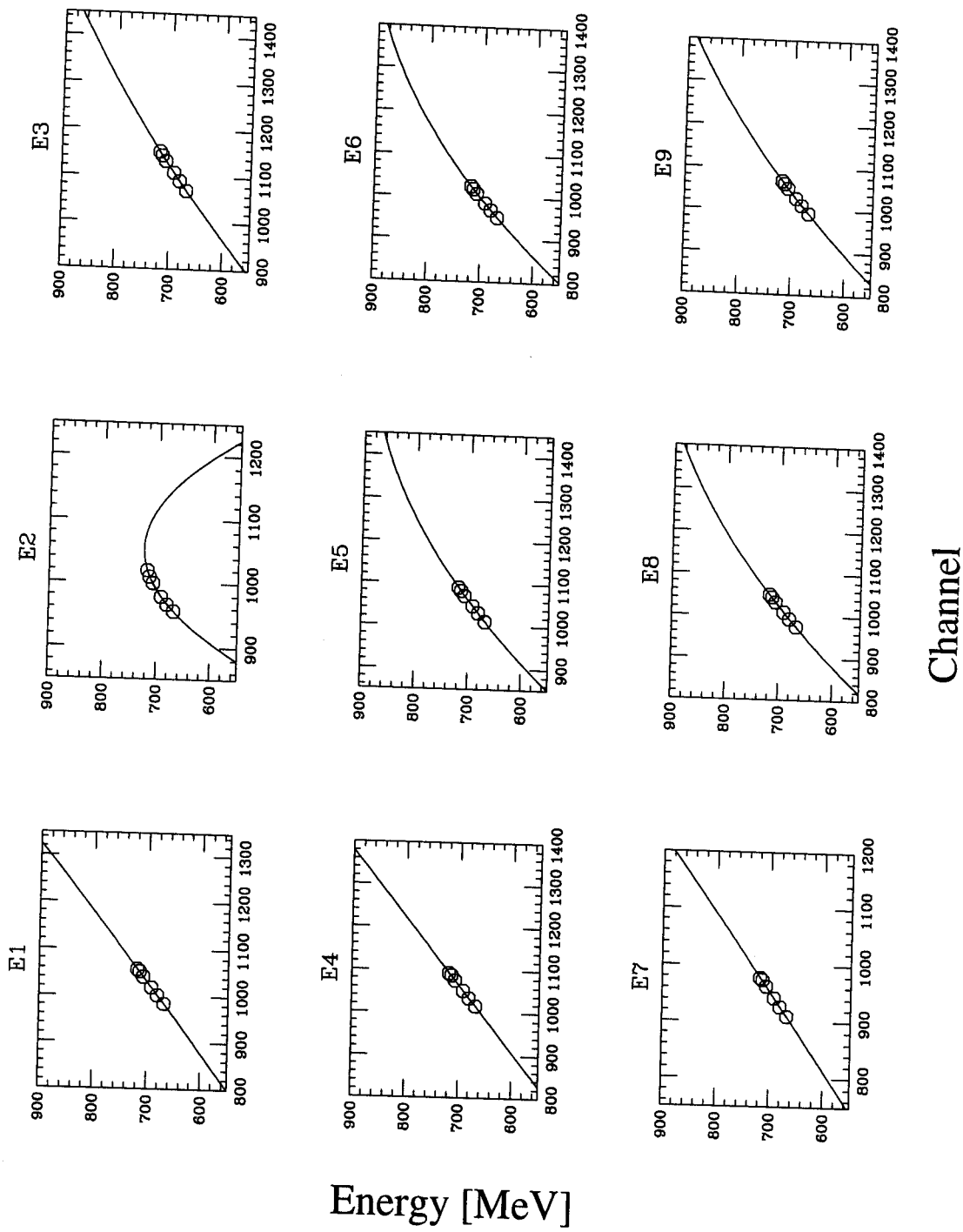

Figure 4.5: Quadratic fitting for energy calibration of the ^{9}Li fragment for each E detector. The E2 detector was omitted due to its nonlinear behavior.

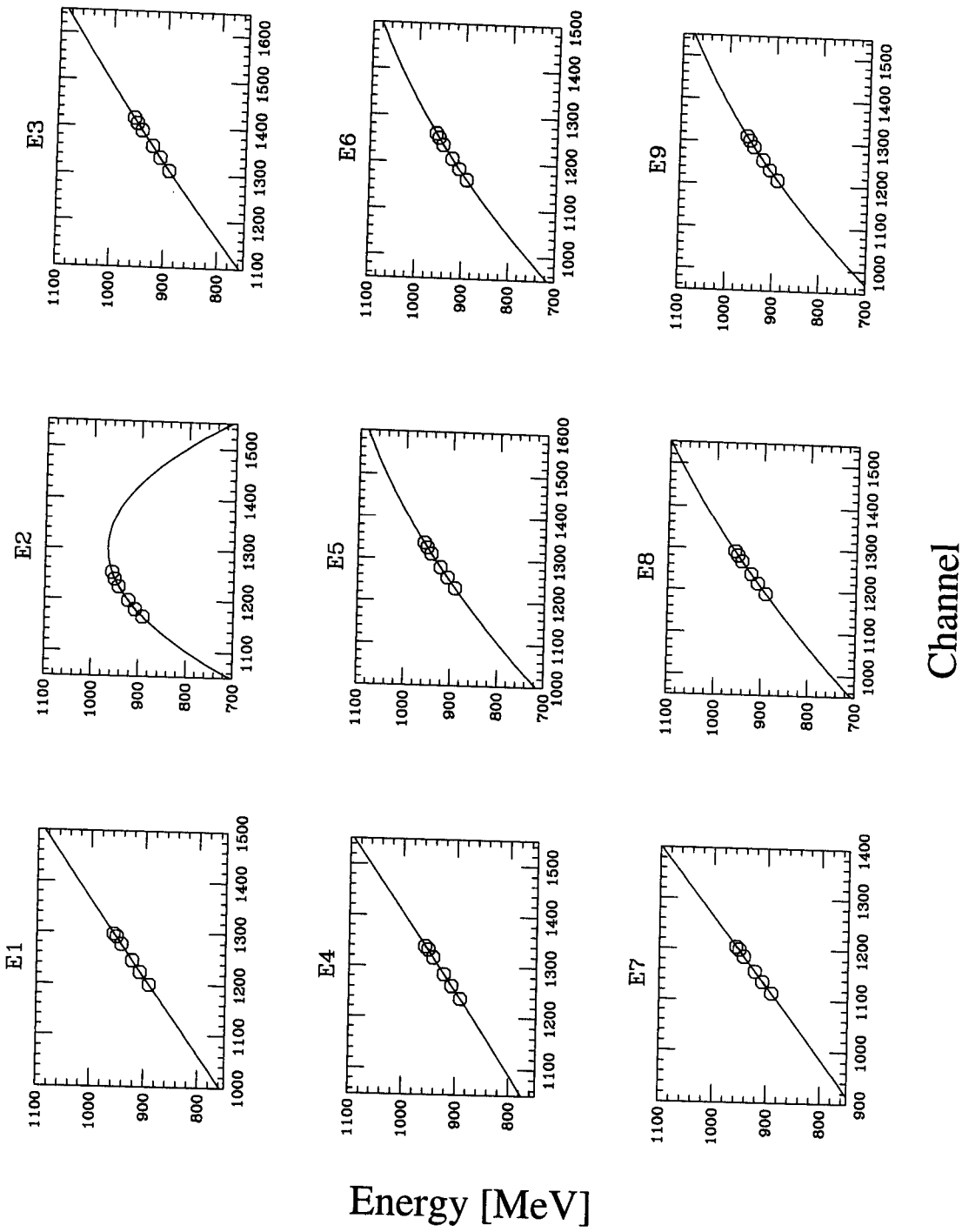

Figure 4.6: Quadratic fitting for energy calibration of the ^{12}Be fragment for each E detector. The E2 detector was omitted due to its nonlinear behavior.

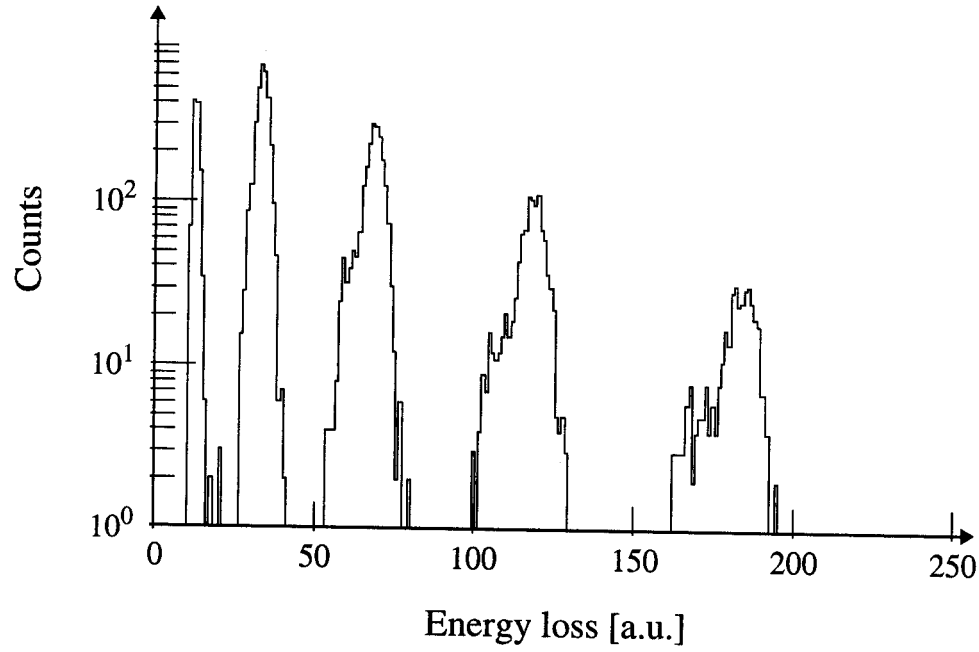

Figure 4.7: Energy loss spectrum of the calibration beam with A/Z=3 gate.

The code STOPX [Oak92] was used to calculate the energy loss of the calibration beams in the ΔE detectors. Peak channel positions in the one dimensional ΔE spectra of ^{6}He, ^{9}Li, and ^{12}Be isotopes were recorded (Figure 4.7) and fitted quadratically as a function of the calculated energy loss by the least square method. The calculated energy loss of the three isotopes were used together to align the peak positions of the same isotope between the all ΔE detectors. Using the constants obtained from the fitting, pseudo parameters were created in the data analysis code for each ΔE1, 2, and 3 signals to align the peaks of the isotopes on the one dimensional pseudo parameter plots. Then the plots of ΔE1, ΔE2, and ΔE3 pseudo parameters were added to obtain a total ΔE information and used for the particle identification in the two dimensional plots (ΔE-E, ΔE-TOF).

4.2.2 Neutron Detector Calibration

The scintillation material (NE 213) in the neutron detectors is sensitive to both neutrons and γ-rays. We used pulse shape discrimination [Hel88] to identify neutrons and γ-rays. The total pulse (total) and the tail of the pulse (tail) from the photomultiplier tubes of neutron detectors were integrated separately (Figure 4.8). The same gate width of 400 ns was used to integrate the charge of those two channels but a different part of the signal was integrated by delaying one signal with respect to the other by 60 ns (see Figure 3.10). Because of the difference of the interactions in the scintillation material, a neutron signal has a larger tail compared to a γ-ray signal with a similar pulse height. This difference separates two particles on the two dimensional plot of tail vs. total signals. A ^{239}Pu-Be neutron-γ-ray source (0 ~ 10 MeV for neutrons and 4.44 MeV for γ-rays) and a ^{60}Co γ-ray source (1.173 MeV

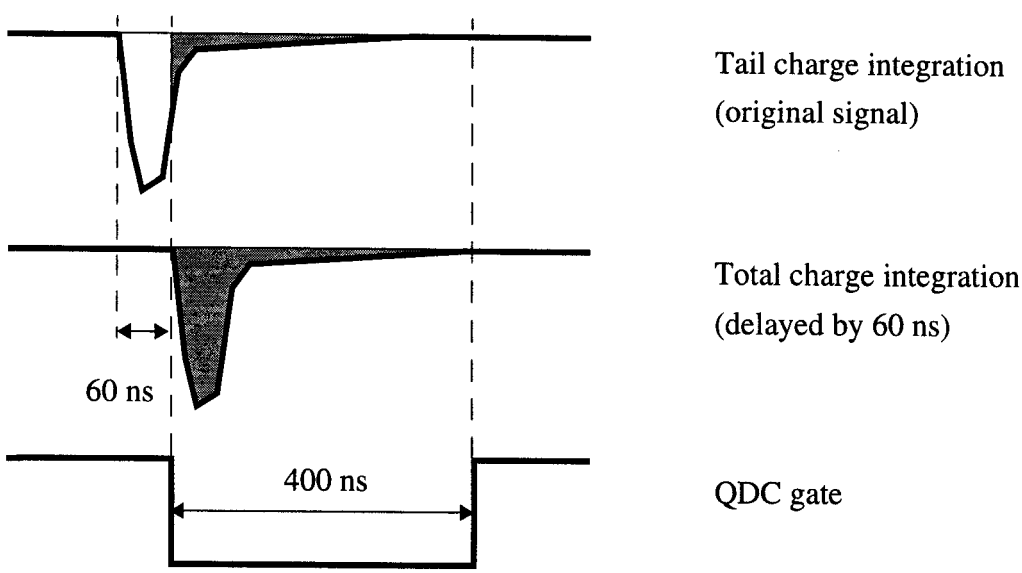

Figure 4.8: Timing diagram of the neutron signals and the QDC gate. Shaded areas show the integrated part of the neutron signal.

and 1.332 MeV) were used to obtain the two dimensional plot shown in Figure 4.9 and the tail gate time and attenuation ratio of total signal were adjusted to maximize the separation of the two groups.

The gains of the five individual neutron detectors were matched with a ^{60}Co γ-ray source (1.173 MeV and 1.332 MeV) and a ^{239}Pu-Be neutron-γ-ray source (4.44 MeV). The projection of the condition around the γ-ray group of the two dimensional plot on the energies is shown in Figure 4.10. The high voltage biases were adjusted to match the compton edges of the five neutron detectors for the ^{60}Co (0.963 MeV and 1.118 MeV) and for the ^{239}Pu-Be (4.198 MeV). Those were -1440 V (N1), -1400 V (N2), -1450 V (N3), -1400 V (N4), and -1400 V (N5). For the experiment the neutron detector signals were then attenuated to be able to accommodate the highest neutron energy signals (~ 80 MeV) within the dynamic range of the QDC.

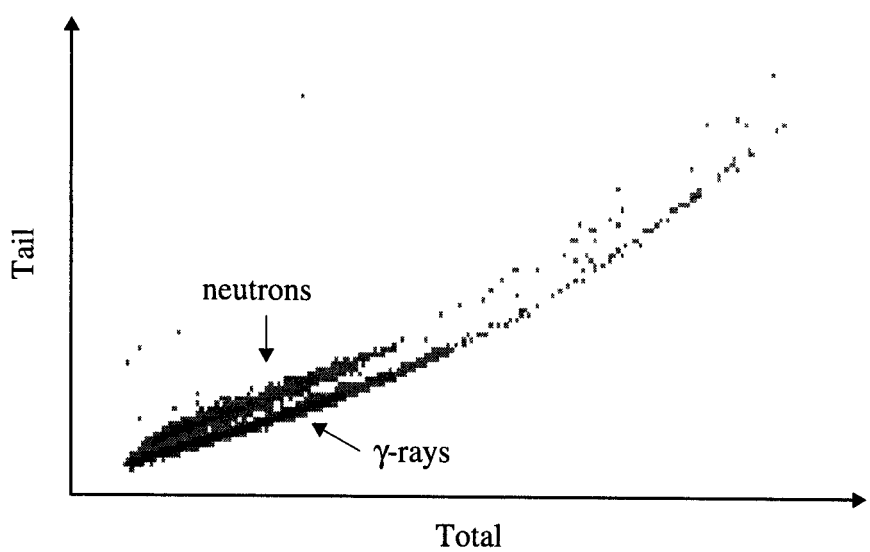

Figure 4.9: Two dimensional plot of the neutron detector signal. A ^{239}Pu-Be source was used to supply γ-rays and neutrons along with ^{60}Co γ-ray source.

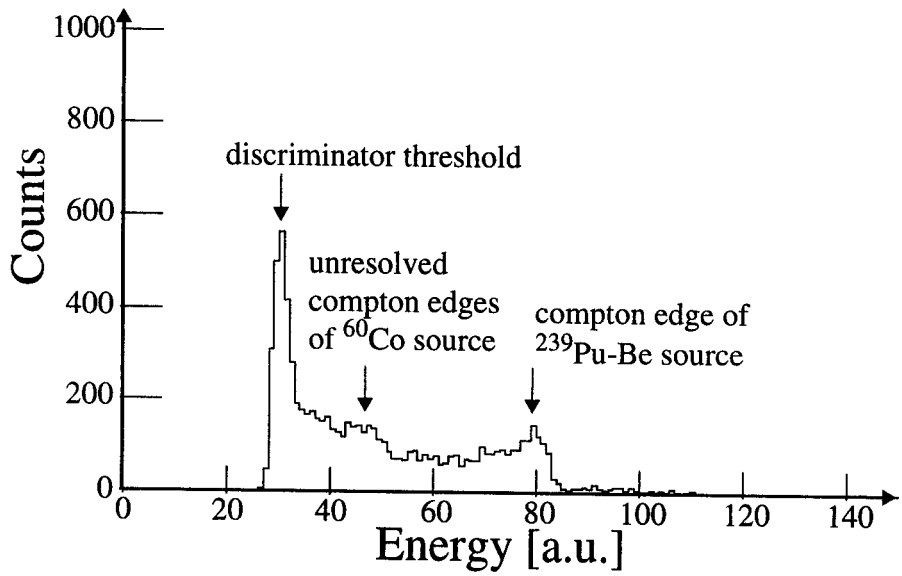

Figure 4.10: Compton edges of a ^{60}Co source and a ^{239}Pu-Be source in a one dimensional plot of the neutron total signal. It was obtained by using the γ-ray condition established in the two dimensional plot (Figure 4.9).

4.2.3 Time Calibration

All TDCs were calibrated with a time calibrator electronics module which created a calibrated time signal (multiple of 10.0 ns) over the TDC range (~ 200 ns). Six positions of the calibration peak for each TDC were recorded and linearly fitted as a function of time in ps. All TDCs had a time gain of ~ 100 ps/ch. The fragment time information was used for the particle identification.

The 'or' of all neutron detectors started a TDC which was stopped by a coincidence fragment in the thin fast plastic detector and recorded in a TDC (TNORP). If t_n is a neutron TOF and t_f is a fragment TOF, then TNORP is defined as

$$TNORP = (t_f + C_f) - (t_n + C_n) \qquad (4.8)$$

where C_f and C_n are constants. Rearranging this equation yields,

$$t_n = t_f - TNORP + C_f - C_n \tag{4.9}$$

Equation 4.9 was used to calculate the TOF of the neutrons (t_n) in the data analysis code. This method had an advantage over the neutron TOF relative to the RF signal of the K1200 cyclotron, because the RF time resolution was larger than 1 ns.

To determine the constants C_f and C_n for each neutron detector, the following procedures were taken. First, the constants C_f are all zero since the fragment time t_f was an absolute flight time of the coincident fragment from the target to the fragment telescope. The fragment time t_f was calculated from the known fragment flight distance (597.0 ± 1.0 cm) and the fragment velocity v which was calculated from the fragment energy information E_f from the E detectors. E_f is expressed as,

$$E_f = mc^2(\gamma - 1) \tag{4.10}$$

$$\gamma = \frac{1}{\sqrt{1 - \left(\frac{v}{c}\right)^2}} \tag{4.11}$$

where m is the particle rest mass, v is the particle speed in the lab frame, and c is the speed of light. Solving Equation 4.10 and 4.11 for the velocity v, we get

$$v = c\sqrt{1 - \left(\frac{mc^2}{E_f + mc^2}\right)^2}\,. \tag{4.12}$$

This calculated fragment velocity v was also used in Equation 3.8 as $V_{fraglab}$ to obtain the relative velocity V_{rel}.

The constants C_n for each neutron detector were determined by observing the peak position of the time reference γ-rays in the RF-neutron TOF spectra in the neutron singles mode. The primary beam bombarded a thick Cu beam stopper and emitted the γ-rays instantly at the time of the incident beam. Since a γ-ray travels at the speed of light and the flight distance between the target and the neutron detectors (580.0 ± 1.0 cm for N1 and N3,

579.0 ± 1.0 cm for N2 and N4, and 592.0 ± 1.0 cm for N5) are known, we could calculate the time offset of the TDC's.

4.3 Coincidence Fragment Spectra

All the neutron-fragment coincidence data was filtered into three groups (He, Li, and Be) and were copied to three 8 mm tapes, one for each group. Filtering conditions were established in two dimensional plots of the gain matched energy loss versus the calibrated energy (ΔE-E) for each fragment group since each isotope, ^{6}He, ^{9}Li, and ^{12}Be had its own energy calibration constants, respectively. No gate was applied to the two dimensional plot of the neutron detector signal (tail vs. total) for the filtering.

When coincidence events are recorded, it is inevitable to record chance coincidence events (randoms) simultaneously since the coincidence gate triggered by the fragments is ~ 200 ns wide and once it is opened, any type of neutron detector signal can satisfy the coincidence condition (see Figure 3.10 and 4.11). The RF signal from the K1200 triggered a TDC start for measuring the fragment time only when a master gate trigger existed. The master gate consisted of coincidences of neutrons with fragments or downscaled neutrons where the time was determined by the neutrons. The neutron detector signal times could have a ~ 200 ns range to be considered as a coincidence event and the gate for the RF was ~ 100 ns wide (see Figure 4.11). If the fragment time spread is considered, the possible neutron time range to satisfy the coincidence condition would be ~ 150 ns. The time relations (Figure 4.11) show that one of four different RF triggers could start the TDC. The most prominent peak (reals) in the fragment TOF spectrum contained the fragments from both real and random coincidence events. Reals and randoms gates for the each isotope (^{6}He,

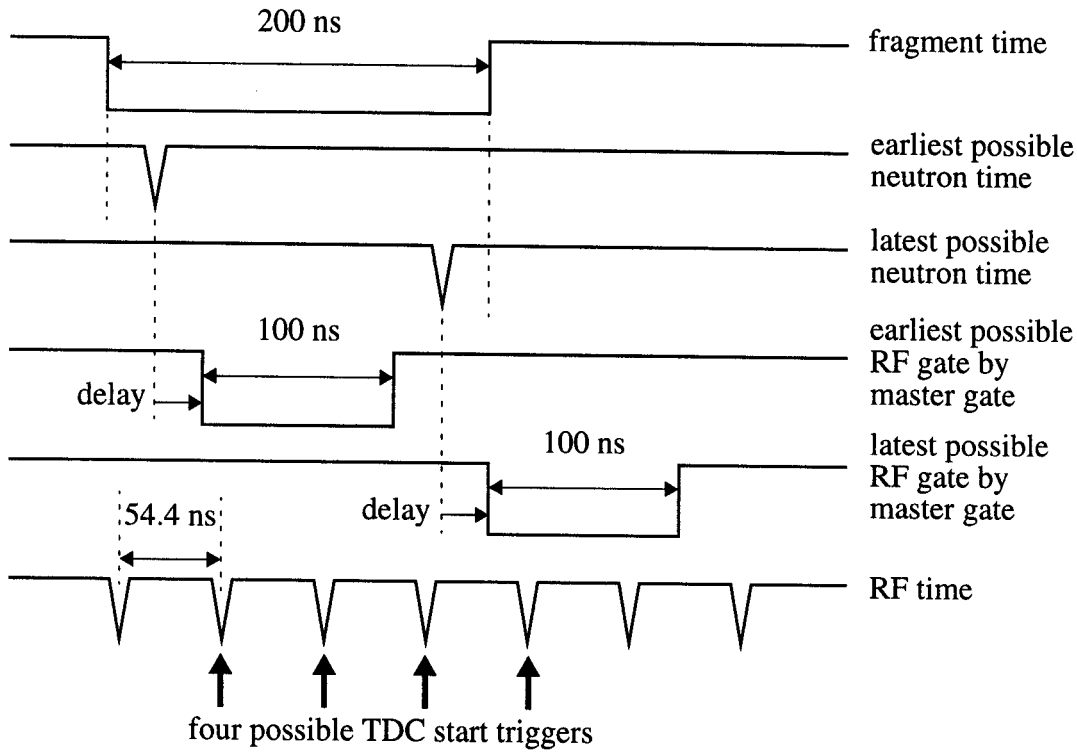

Figure 4.11: The relation of the fragment time signal, the neutron detector signal, and the RF time signal. The earliest and latest possible neutron signal have margins of ~ 25 ns from the edge of the fragment signal to take a fragment time spread into account.

^{9}Li, and ^{12}Be) in ΔE vs. TOF plots as well as individual isotope gates (^{6}He, ^{9}Li, and ^{12}Be) in E vs. ΔE plots were established using each filtered data sets. It was necessary to subtract the randoms from the reals to extract the shape of the relative velocity spectrum only from the real coincidence events.

4.3.1 He group

The filtered data of the He group was used to observe the known state of ^{7}He. To select the ^{6}He group from the one neutron decay of ^{7}He, energy loss versus total energy plot (ΔE-E, Figure 4.12) and energy loss versus time of flight plot (ΔE-TOF, Figure 4.13) were used. The ^{6}He isotope gate, the ^{6}He reals gate, and the ^{6}He randoms gate are indicated in the figures. The ^{6}He nucleus has a long enough lifetime (~ 807 ms) to be observed in the fragment telescope. The neighbors of the ^{6}He (^{5}He and ^{7}He) are both unbound which makes it easy

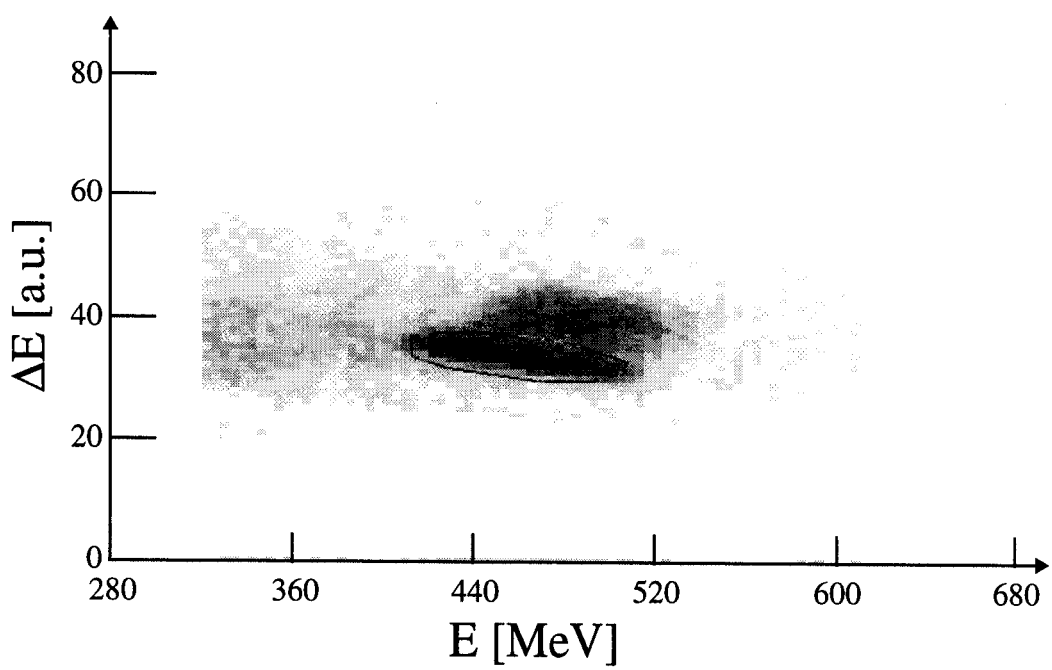

Figure 4.12: ΔE_1 (first quadrant of ΔE) vs. E3 plot of He group. The oval contour shows a ^{6}He gate.

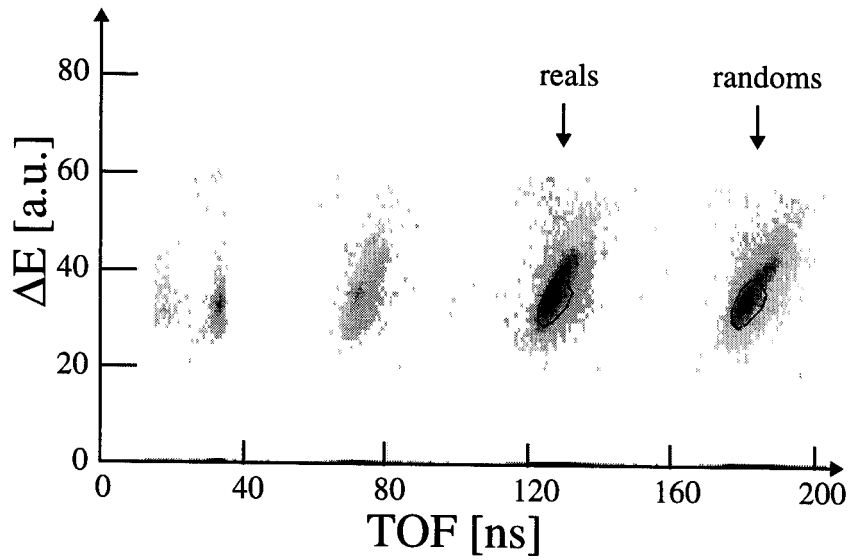

Figure 4.13: ΔE_1 (first quadrant of ΔE) vs. TOF (thin plastic time) plot of He group. The contour gates show the ^{6}He reals gate and the ^{6}He randoms gate.

to isolate the ^{6}He group in the two dimensional plots.

4.3.2 Li Group

To study ^{10}Li states, the coincidence events of a neutron and a ^{9}Li were separated from the other events. Similar to the ^{7}He case, energy loss versus total energy plot (ΔE-E, Figure 4.14) and energy loss versus time of flight plot (ΔE-TOF, Figure 4.15) were used. ^{10}Li itself was not observed on the ΔE-E and the ΔE-TOF plot because it is a neutron unbound nucleus. ^{8}Li and ^{9}Li have long enough lifetimes (~ 838 ms and ~178 ms) to be detected in the fragment telescope. Like in the ^{7}He case of the previous section, the reals and the randoms of the ^{9}Li were selected by the gates in the ΔE-TOF spectra.

The ΔE-E plots were handled similar to the ^{7}He case except that E5, one of the CsI(Tl) E detectors was excluded since it did not have a sufficient isotope separation between the

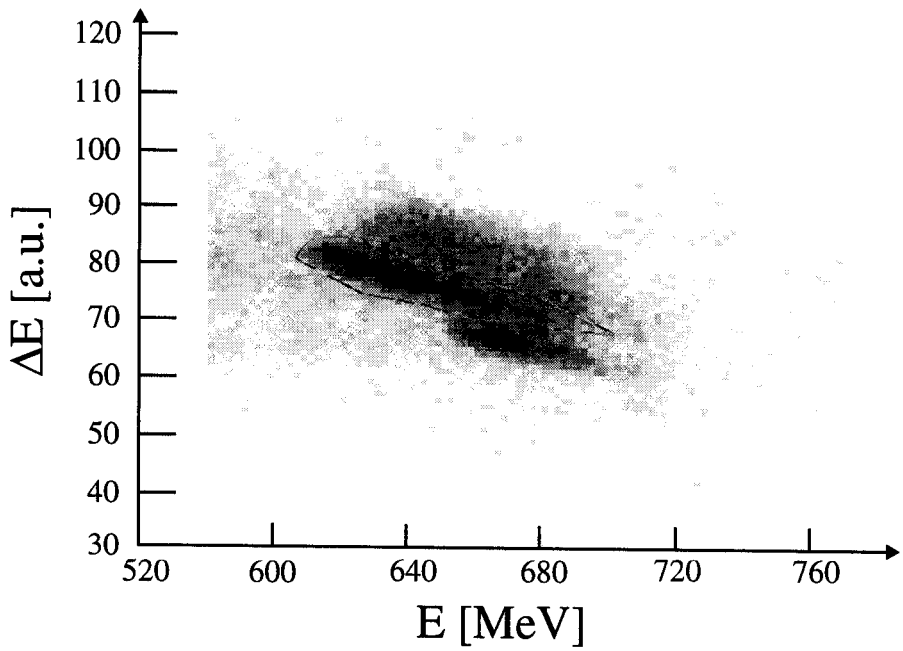

Figure 4.14: ΔE_1 (first quadrant of ΔE) vs. E3 plot of the Li group. The contour shows a ^{9}Li isotope gate.

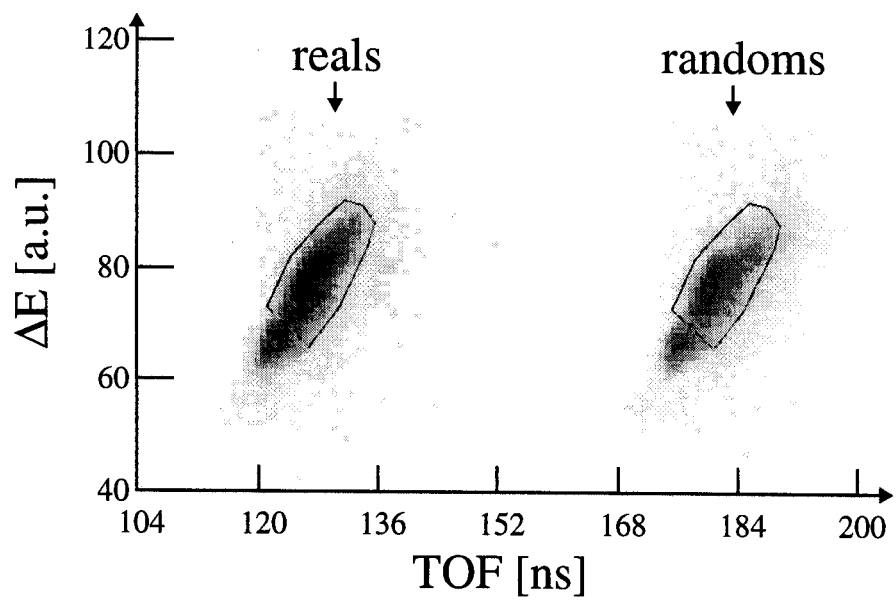

Figure 4.15: ΔE_1 (first quadrant of ΔE) vs. TOF (thin plastic time) plot of Li group. The contour gates show the ^{9}Li reals gate and the ^{9}Li randoms gate.

^{8}Li and ^{9}Li group. This was probably due to abnormal scattering at the center of the ΔE detectors (see Figure 3.8), since the E5 detector was located right behind the center crossing of the segmentation lines of the ΔE detectors (see Figure 3.9). Thus, the E5 related Li data was omitted in the later analysis.

4.3.3 Be Group

The filtered data of the Be group was used to select neutron decay events of ^{13}Be. Energy loss versus total energy plot (ΔE-E, Figure 4.16) and energy loss versus time of flight plot (ΔE-TOF, Figure 4.17) were used to select the^{12}Be group from the one neutron decay of ^{13}Be. Unlike ^{13}Be, the neighbors ^{11}Be and ^{12}Be have long enough lifetimes (~ 14 s and ~ 24 ms) to be detected in the fragment telescope. The E5 related Be data were also omitted in the later analysis from the same reason mentioned in the Li section.

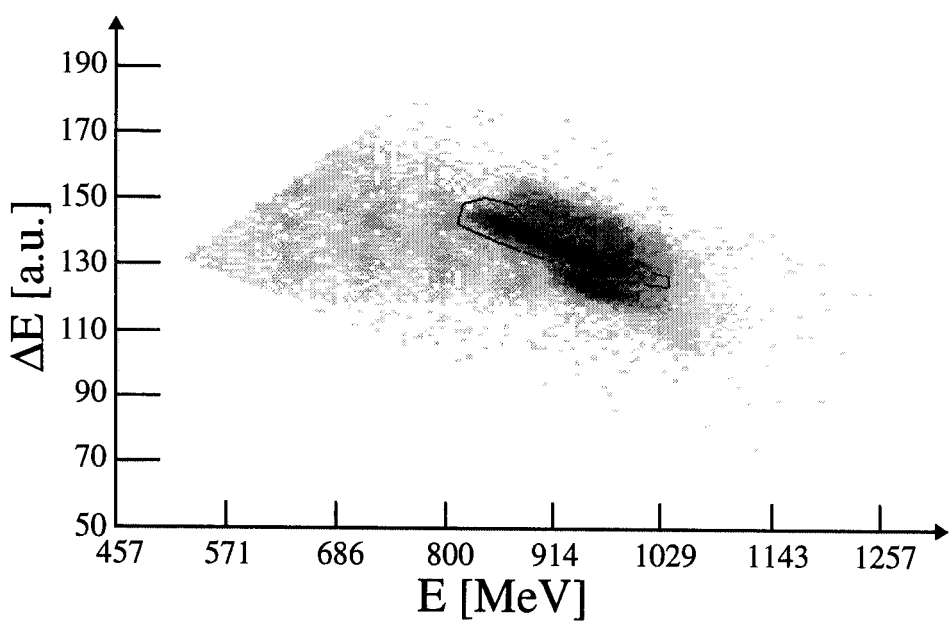

Figure 4.16: ΔE_1 (first quadrant of ΔE) vs. E3 plot of the Be group. The contour shows a ^{12}Be isotope gate.

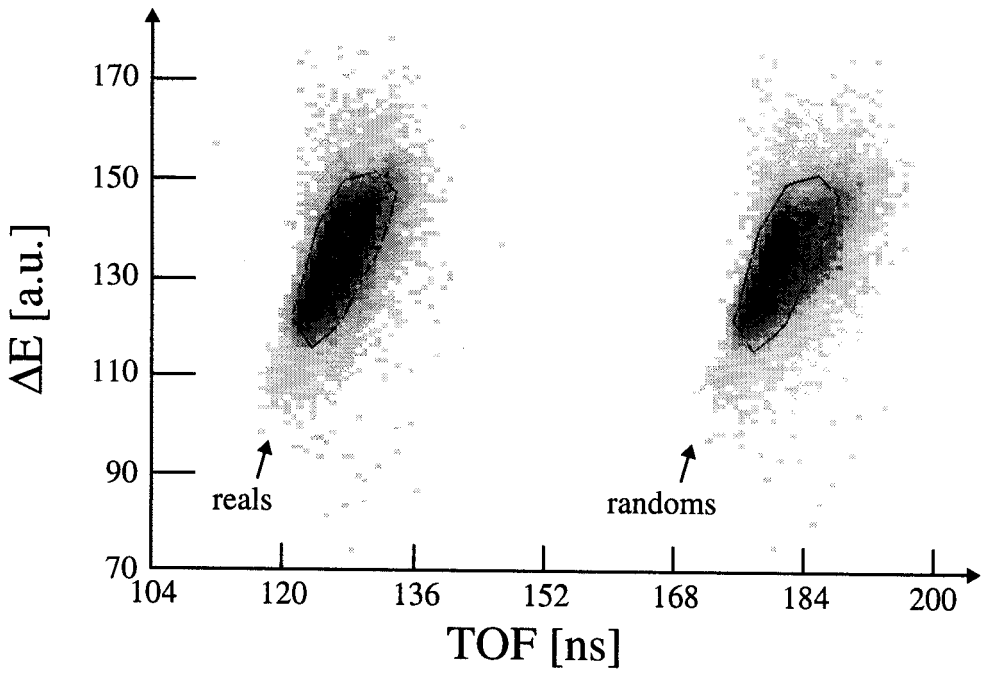

Figure 4.17: ΔE_1 (first quadrant of ΔE) vs. TOF (thin plastic time) plot of Be group. The contour gates show the ^{12}Be reals gate and the ^{12}Be randoms gate.

4.4 Simulation of Experiment

Monte Carlo simulations were performed to calculate the relative velocity spectrum for the one neutron decay of ^{7}He, ^{10}Li, and ^{13}Be, respectively. The decay of each fragment was initially considered in the center of mass (CM) frame of the daughter fragment and the neutron. The decay direction was assumed to be isotropic in the CM frame and a Breit Wigner lineshape of the form [Lan58]

$$\frac{d\sigma}{dE} = \frac{\Gamma(E)}{(E-E_r)^2 + \frac{1}{4}[\Gamma(E)]^2} \tag{4.13}$$

where

$$\Gamma(E) = \frac{kP_l(E)}{k_r P_l(E_r)}\Gamma_0 \tag{4.14}$$

was used. $P_l(E)$ was the l-dependent neutron penetrability function, and $\Gamma_0 = \Gamma(E = E_r)$ was

the width at the resonance energy E_r.

The decay energy of each event was transformed into the center of mass velocity of the neutron and the fragment, and then into the laboratory frame velocity of the neutron and the fragment. In the next step, the decay direction of the fragment in the laboratory frame, was compared with the data in an acceptance file which was calculated using the RAYTRACE [Kow87] code. It contained the data of valid directions of the fragment velocity in the laboratory frame at the target to reach the fragment telescope. The magnet settings of the quadrupole and the dipole, the location of the 11° beam pipe and the Cu collimator (see Figure 3.3, 3.7) were considered in the calculation. The events which had fragment velocity directions outside this acceptance were excluded. The direction of the neutron velocity in the laboratory frame was checked and only the events which hit the neutron detector array were used to calculate the relative velocity. The neutron detector efficiency was taken into account for the histogramming of the relative velocity spectrum by looking up an efficiency file which contained efficiency factors for each neutron energy. This file was created by the KSUEFF [Cec79] code.

A simulation for the neutron decay of ^{7}He was executed first to set the parameters of the Monte Carlo simulations and constants in the data analysis code, since ^{7}He has a well established ground state energy (E_r = 440 ± 30 keV) and width (Γ_0 = 160 ± 30 keV) [Ajz88].

The input parameters of the simulation were set in the following way. The TOF resolution (σ = 0.057ns) of the daughter fragment ^{6}He was calculated from the energy resolution of the CsI(Tl) E detectors because it was calculated from the energy information. The centroid of the momentum distribution (2733.3 MeV/c for ^{7}He) and the width of the

scattering angle (70.47 mrad for ^{7}He) of the fragmentation product at the target (^{9}Be, 94 mg/cm^{2}) were predicted using INTENSITY. The momentum spread of the fragmentation product (σ = 3.54% for ^{7}He) for the simulation was set to match the actual spread of experimental data of the coincidence runs. After setting these parameters, the TOF resolution of the neutron was found by reduced chi-square (χ_{ν}^{2}) minimization of the fit of the calculated relative velocity spectrum to the measured spectrum. Figure 4.18 shows the minimum of a neutron TOF resolution at $\sigma \sim 0.70$ ns.

For the decay of ^{10}Li to ^{9}Li + n and ^{13}Be to ^{12}Be + n, the simulations were carried out for different combinations of decay energy, width, and angular momentum. The TOF resolution of the fragment and the neutron were fixed to the value which was established from the ^{7}He neutron decay simulation. The centroid of the momentum distribution (3901.9 MeV/c for ^{10}Li and 5068.8 MeV/c for ^{13}Be) and the width of the fragment scattering angle

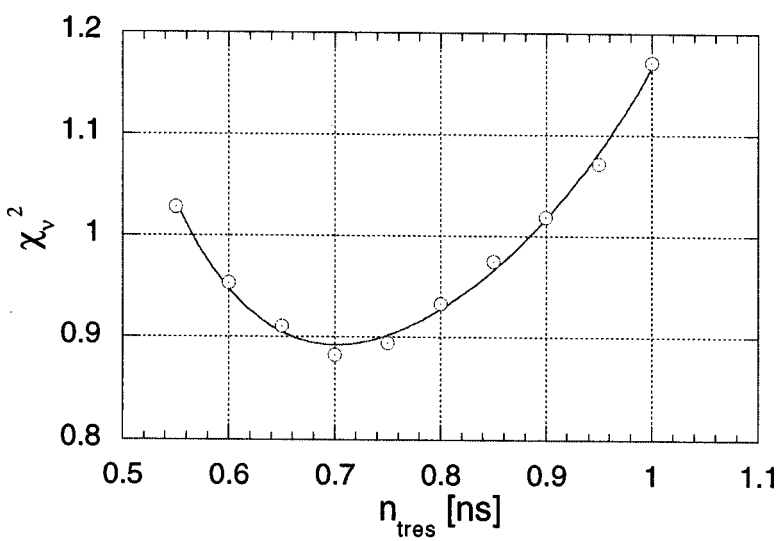

Figure 4.18: χ_{ν}^{2} versus neutron TOF resolution plot. χ_{ν}^{2} is for the fit of the ^{7}He neutron decay simulation and the data. The minimum χ_{ν}^{2} of (best fit) is at $t_{nres} \sim 0.70$ ns.

(53.90 mrad for ^{10}Li and 42.38 mrad for ^{13}Be) were also calculated by INTENSITY. The middle of the momentum distribution of the fragmentation products (σ = 3.38% for ^{10}Li and σ = 3.22% for ^{13}Be) were obtained in a same way as in the ^{7}He case.

Chapter 5

Results and Discussion

5.1 Selection of The Valid Events

The valid events for the relative velocity ($V_{rel} = V_n - V_f$, Equation 3.8) spectra were selected with the ΔE-E isotope gates, with the ΔE-TOF isotope gates for reals and randoms, and with the neutron gates on the two dimensional plot of the neutron signals (see previous chapter). Relative velocity spectra were obtained for each isotope, for each neutron detector, and for reals and randoms by scanning the filtered data for the same Z group. The relative velocity spectra of randoms were subtracted from the reals, and all the subtracted spectra for the different neutron detectors were summed to obtain the total relative velocity spectrum for each isotope.

5.2 The Relative Velocity Spectrum of ^{7}He

^{7}He has a $vp_{3/2}$ ground state with a neutron separation energy of S_n = -440 ± 30 keV and a Γ = 160 ± 30 keV width [Ajz88]. Figure 5.1 shows the relative velocity spectrum for ^{6}He + n coincidence events which were collected simultaneously with the ^{9}Li + n and the ^{12}Be + n events. The open circles with the error bars in the figure represent the data and the solid line is the simulated decay of the ground state of ^{7}He (dotted) superimposed upon an

estimated background (dashed). The known decay energy and width were used in the simulation. The two peaks in the relative velocity spectrum correspond to forward (positive V_n-V_f) and backward (negative V_n - V_f) emitted neutrons. V_n - V_f = 0.0 cm/ns indicates zero decay energy (Q-value is zero).

The precise source of the background for the neutron-fragment coincidence events is unknown. The background has previously been investigated using the distribution for a thermal neutron source of the form $\sqrt{E}\exp(-E/T)$ [Deá87]. This thermal source lead to a near-Gaussian shape background in the Monte Carlo simulation, thus Heilbronn [Hei90] treated them in general as a simple broad Gaussian which had a centroid at some nonzero relative velocity value. This approach was also adapted in the present case. The parameters of the background Gaussian were obtained by fitting the data to the simulation which assumed to be a sum of a broad Gaussian and the ground state decay simulation of ^{7}He, leaving the centroid, width, and amplitude of the Gaussian and the amplitude of the decay simulation as fitting parameters.

In Figure 5.2, the solid line shows the calculated lineshape by the Breit-Wigner form (Equation 4.12) with the l-dependent neutron penetrability factor, which was used for the simulation of the ground state decay of ^{7}He. The neutron separation energy of S_n = -440 keV, width of Γ = 160 keV, and l = 1 were used for the calculation. The result for the l = 0 with the same parameter as the l = 1 case is shown in the figure with the dashed line for comparison. The lower energy part of the l = 1 lineshape is clearly suppressed compared to the l = 0 case because of the l dependent penetrability factor.

Previously, Kryger *et al.* [Kry93] employed the same experimental method of sequential neutron decay spectroscopy (SNDS) at 0° to investigate the ground state of ^{10}Li. Kryger

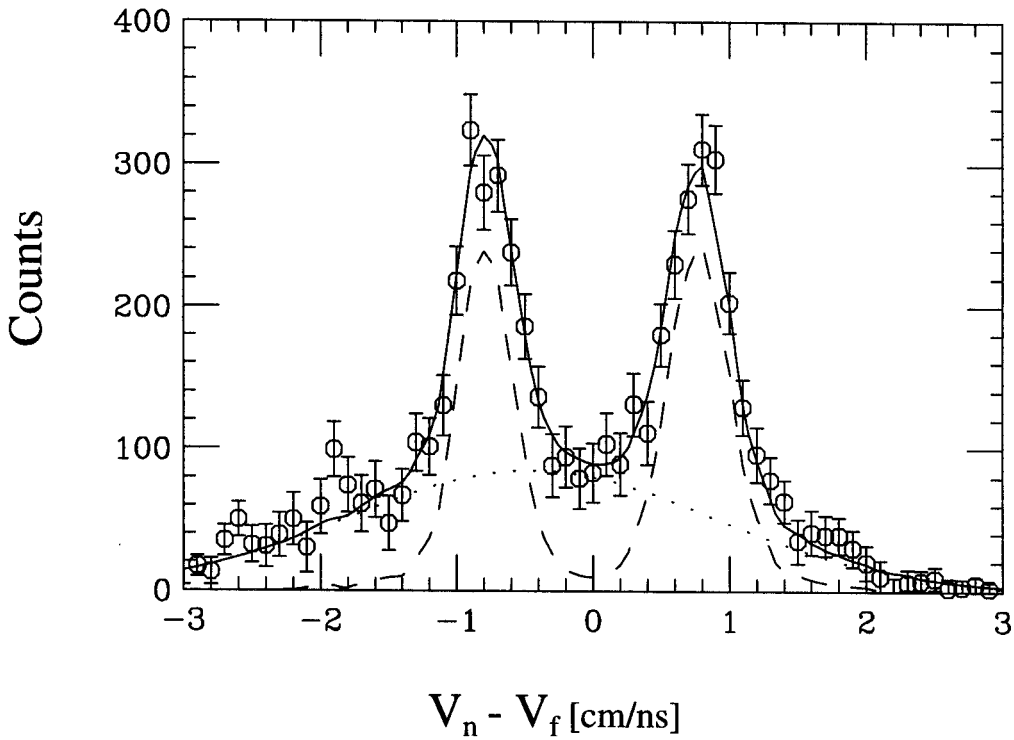

Figure 5.1: The relative velocity spectrum for ^{6}He + n coincidence events. The circles with the error bars are the data. The dashed line shows the estimated background. The dotted line is the simulated decay of ground state of ^{7}He without the background and the solid line is a sum of the background and the simulation.

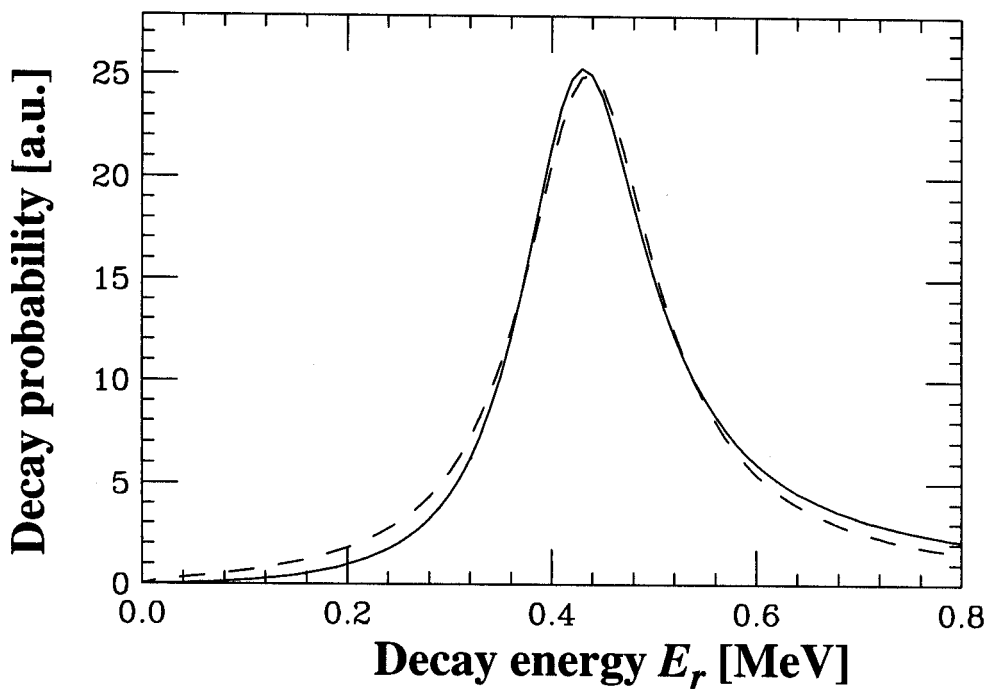

Figure 5.2: The Breit-Wigner lineshapes of ^{7}He state at $E_r = 440$ keV with the width of $\Gamma = 160$ keV. The solid line shows the actual case with the angular momentum $l = 1$. For the comparison, $l = 0$ case is shown with the dashed line. The low energy region of the peak for the $l = 1$ case is suppressed compared to the $l = 0$ case.

et al. used the cyclotron RF as the start for the TOF for both the neutrons and the fragments to calculate the neutron velocity V_n and the fragment velocity V_f and obtained the relative velocity V_{rel} (= V_n - V_f). The time resolution for the neutron TOF and the fragment TOF were both $\sigma_{tn} = \sigma_{tf} = 0.89$ns. The current experiment used the fragment energy information from the E detectors to calculate the V_f to utilize the superior energy resolution (0.49%, FWHM), corresponding to a fragment TOF resolution of $\sigma_{tf} = 0.057$ns. The fragment TOF, calculated from the energy, and the TNORP were used to calculate the TOF of neutrons yielding a resolution of $\sigma_{tn} = 0.70$ ns. The resolution was thus significantly improved for the current experiment. The width of the peaks of ^{6}He + n coincidence events were also used to confirm the experimental resolutions. Figure 5.3 shows a comparison of the relative velocity spectrum calculation using the different timing resolution. The dotted line shows the perfect resolution case (neutron TOF resolution; $\sigma_{tn} = 0.00$ ns, fragment timing resolution; $\sigma_{tf} = 0.00$ ns). The dashed line shows the spectrum with the resolution of the setup used by Kryger *et al.* ($\sigma_{tn} = 0.89$ ns, $\sigma_{tf} = 0.89$ ns). The solid line shows the spectrum with the resolutions of the current experiment ($\sigma_{tn} = 0.70$ ns, $\sigma_{tf} = 0.057$ ns). As one can see from the figure, the width of the peaks in the relative velocity spectrum of the data is broadened by an finite experimental time resolutions. The current experiment clearly shows the improvement in the resolution of the relative velocity.

5.3 The Relative Velocity Spectrum of ^{10}Li

The first measurement by Wilcox *et al.* was reported in 1975 observing a lowest ^{10}Li unbound state at $E_r = 800 \pm 250$ keV and $\Gamma = 1200 \pm 300$ keV. Then the presence of a *p*-wave state at $E_r = 420 \pm 50$ keV and $\Gamma = 800 \pm 60$ keV was reported by Bohlen *et al.* [Boh93]

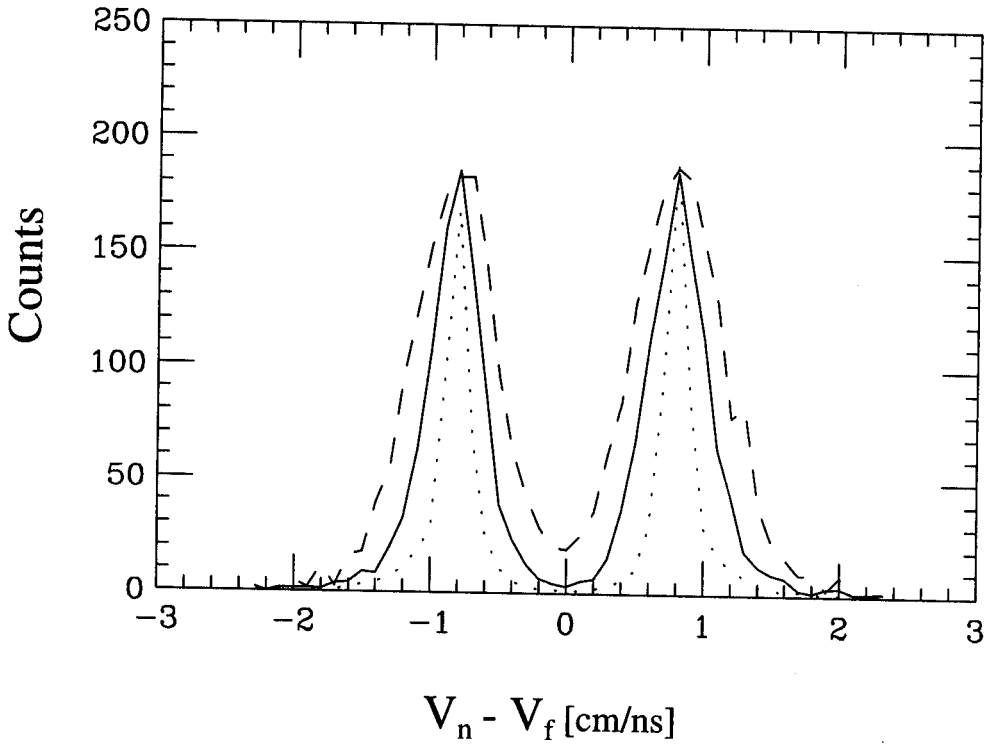

Figure 5.3: The relative velocity spectrum simulation of $^7He \rightarrow {}^6He + n$ decay for the different time resolutions. The dotted line shows a case of perfect resolution ($\sigma_{tn} = 0.00$ ns, $\sigma_{tf} = 0.00$ ns). The solid line shows a case of a current experimental resolution ($\sigma_{tn} = 0.70$ ns, $\sigma_{tf} = 0.057$ ns). The dashed line shows a case of the experiment by Kryger *et al.* ($\sigma_{tn} = 0.89$ ns, $\sigma_{tf} = 0.89$ ns).

and interpreted as the ground state. However, a low-lying *s*-wave state at $E_r = 150$ keV and $\Gamma_0 < 400$ keV by Amelin *et al.* [Ame90] and also by Kryger *et al.* [Kry93] were reported as the ^{10}Li ground state. Young *et al.* [You94] observed a *p*-wave state similar to Bohlen's value ($E_r = 538 \pm 60$ keV) and, in addition, evidence of the lower lying state ($E_r \sim 100$ keV). Ostrowski *et al.* recently reported a new value ($E_r = 240$ keV) as a *p*-wave ground state [Ost96]. Our newly obtained data allowed us to determine if this state could potentially correspond to the state observed by Kryger *et al.*

Figure 5.4 shows the relative velocity spectrum of the ^{9}Li and neutron coincidence events. The dotted line indicates an estimated broad Gaussian background. The dashed lines show a simulated *p*-wave state (side peaks) at $E_r = 538$ keV, $\Gamma_0 = 358$ keV, corresponding to the result reported by Young *et al.* [You94] and a simulated *s*-wave state (central peak) at $E_r = 50$ keV, $\Gamma_0 = 241$ keV. The positions of the side peaks in the data matches the simulation with the Young's value quite well, however the statistics is not sufficient to extract the values from a fit to the data. The *p*-wave state reported by Bohlen *et al.* ($E_r =$ 420 keV) was also tried for the simulation and yielded similar side peaks in the relative velocity spectrum as the Young's state ($E_r = 538$ keV). Therefore, we consider these two states as one state. In the new report by Ostrowski *et al.*[Ost96], this state was also assumed as a first excited state for a fitting purpose. Thus the state at $E_r = 538$ keV (Young's value) was assumed and included in the subsequent χ^2 fitting procedures.

To extract the decay energy and the width of the initial state for the central peak, simulations were performed and fitted to the data. For the ^{10}Li initial state, neutron decays corresponding to states of $l = 0$ case and $l = 1$ case were considered. Each central peak simulation had a certain combination of the decay energy E_r, the width Γ_0, and the l value

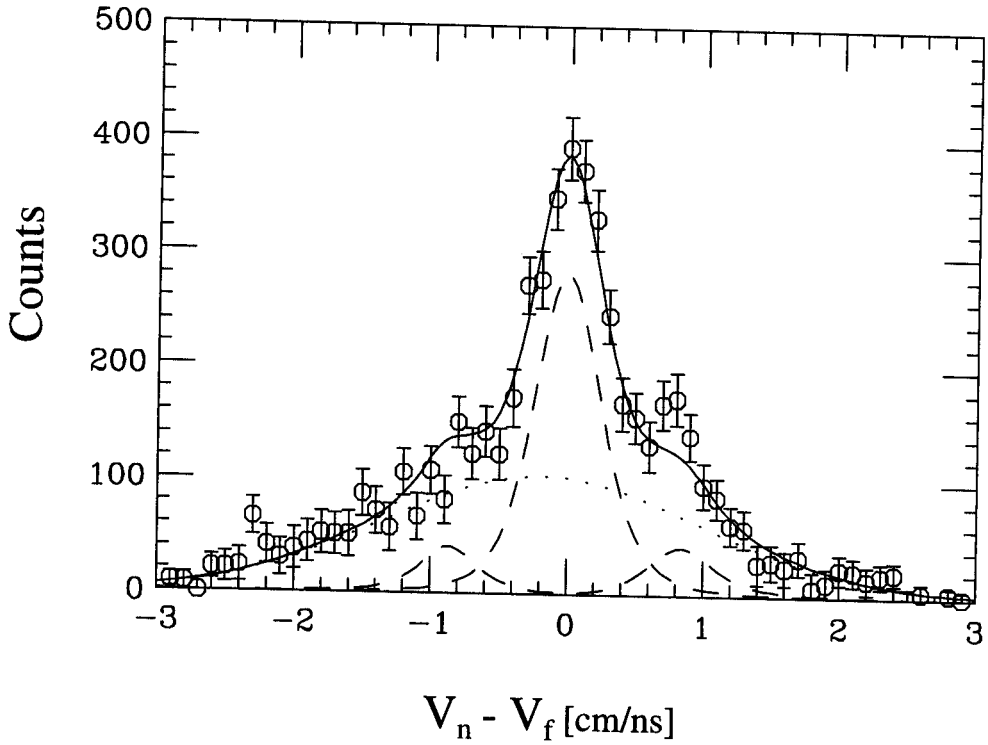

Figure 5.4: The relative velocity spectrum of ^{10}Li $\rightarrow$ ^{9}Li + n. The convention of the data point and the Gaussian background are the same as the ^{7}He spectrum. The dashed side peaks are the simulation of the p-wave state at E_r = 538 keV reported by Young *et al.* The dashed central peak is the simulation with l = 0, E_r = 50 keV, Γ_0 = 241keV. This is the fit at χ^2_ν minimum for the s-wave neutron.

of the initial state neutron in ^{10}Li. The output file of the central simulation was used along with the $p_{1/2}$ state at 538 keV for the fitting. The amplitude of these two simulations and the parameters of the Gaussian background (amplitude, centroid, and width) were set to be free parameters and the best fit was searched to minimize the reduced chi-square χ^2_ν with a computer routine [Bev69].

χ^2_ν surfaces as a function of Γ_0 and E_r were extracted in Figure 5.6 and 5.9. The overall minimums of the reduced chi-square $\chi^2_{\nu min}$ are indicated with x. The reduced chi-square value $\chi^2_\nu = \chi^2_{\nu min} + 0.5$ was considered to be a tolerance limit of a good fit. The upper limits of the width Γ_0 for each decay energy E_r were calculated by setting the spectroscopic factor θ^2_l to the theoretical limit which is unity in a formula of a broad resonance [Rol88],

$$\Gamma_l(E) = \frac{2\hbar}{R_n}\left(\frac{2E}{\mu}\right)^{1/2} P_l(E, R_n)\theta^2_l \qquad (5.1)$$

where $E = E_r$ in this case since $\Gamma_0 = \Gamma(E = E_r)$ was used for the simulation parameter, R_n is the nuclear radius, and P_l is the l dependent penetrability factor. This limit is referred to as the Wigner limit. The solid lines shows the Wigner limit and the dashed lines correspond to constant χ^2_ν values of $\chi^2_{\nu min} + 0.5$, $\chi^2_{\nu min} + 1.0$, and $\chi^2_{\nu min} + 1.5$ as indicated in the figures.

In the relative velocity spectrum, the distance along the abscissa from 0.0 cm/ns is directly related to the relative decay energy E_r as described in Equation 3.3. Therefore, the existence of the central peak inside the two side peaks of the 538 keV p-wave state in the relative velocity spectrum implies another state with a lower decay energy than the p-wave state and/or with a very broad width.

The widths of the peaks in the relative velocity spectra are related to the width of the initial state and the final state of the decay as well as the experimental resolution. For the

final states, only the bound states matter for the analysis. ^{9}Li has only two bound states which are the ground state and the first excited state (E_x = 2.691 MeV). As final states of the ^{10}Li neutron decay, the widths of these two states are very narrow [Ajz88], and their contribution to the width of the peaks in the relative velocity spectra were negligible compared to the contribution from the width of initial states and the finite experimental resolution.

The present experimental method was only sensitive to the Q-value of the reaction and not to the quantum numbers of the observed state, thus the single central peak of the data in the spectrum could be interpreted in more than one way. Figure 5.5 shows a level diagram of different possible cases of ^{10}Li to ^{9}Li + n decay to interpret the result. The first scenario is illustrated in (a). The central peak could be a decay from a state of ^{10}Li to the ground state of ^{9}Li. In the second scenario which is illustrated in (b), the central peak could

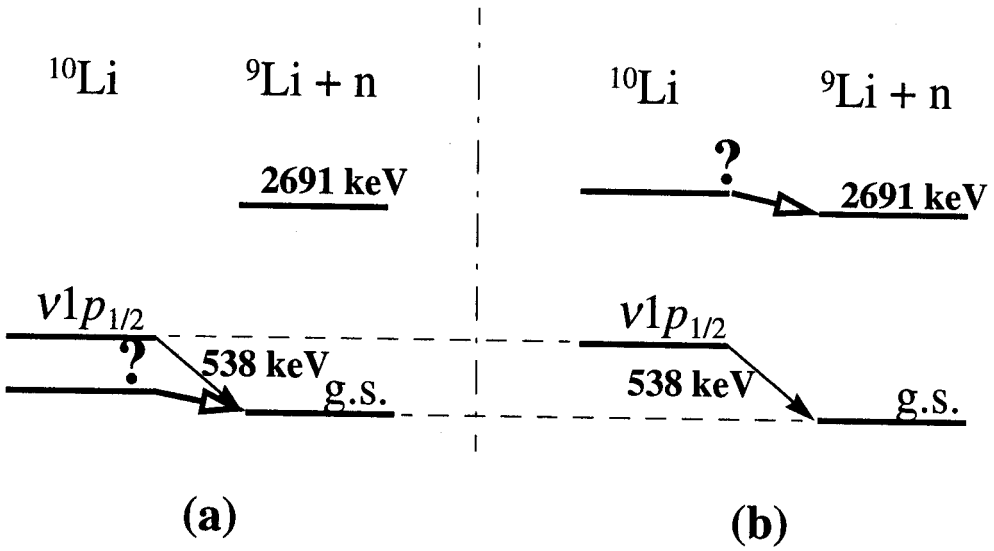

Figure 5.5: The level diagram of the possible two cases of the neutron decay of ^{10}Li.

be due to the decay from an excited state of ^{10}Li to the first excited state of ^{9}Li at $E_x = 2.691$ MeV.

5.3.1 The *s*-wave Case

If the initial state of the decay is assumed to be an *s*-wave, the minimum of the reduced chi-square is $\chi^2_{\nu min} = 1.034$ at $E_r = 50$ keV and a decay width of $\Gamma_0 = 241$ keV (see Figure 5.6).

If the case (a) of the Figure 5.5 is assumed, the decay energy E_r would be equal to the neutron separation energy S_n of the ^{10}Li. Then the limits established in Figure 5.6 can be compared to the limits determined by Kryger *et al.* [Kry93] which are also indicated in the figure as vertical and horizontal solid lines. The current result yields a more stringent limit than Kryger's result because of the improved experimental resolution and the consideration of the Wigner limit. The present result is consistent with a recent measurement of the break-up of ^{11}Be [Ish96]. This reconstructed spectrum for ^{10}Li could be explained with an *s*-wave at $E_r = 350 \pm 150$ keV and a width of $2.2\ ^{+3.0}_{-0.5}$ MeV.

Since a broad resonance was assumed for the central peak and the side peaks in the relative velocity spectrum, the Breit-Wigner lineshape was used for the analysis of the current data. However, *s*-wave neutron decay does not have a barrier and thus is not a real resonance. Therefore the low-lying *s*-wave state was also analyzed using the scattering length as a parameter. Zinser *et al.* measured the one neutron stripping of ^{11}Li and measured the transverse momentum distribution of the neutrons in coincidence with ^{9}Li. They interpreted their result as evidence of the *s*-wave ground state of ^{10}Li and described the result with an *s*-wave scattering length of $a_s = -20$ fm or less, equivalent to an excitation energy below 50 keV. The current result of the resonance energy at $E_r = 50$ keV and $\Gamma_0 = 241$ keV corresponds to an *s*-wave scattering length of $a_s = -40.0 \pm 5.0$ fm. This number was obtained

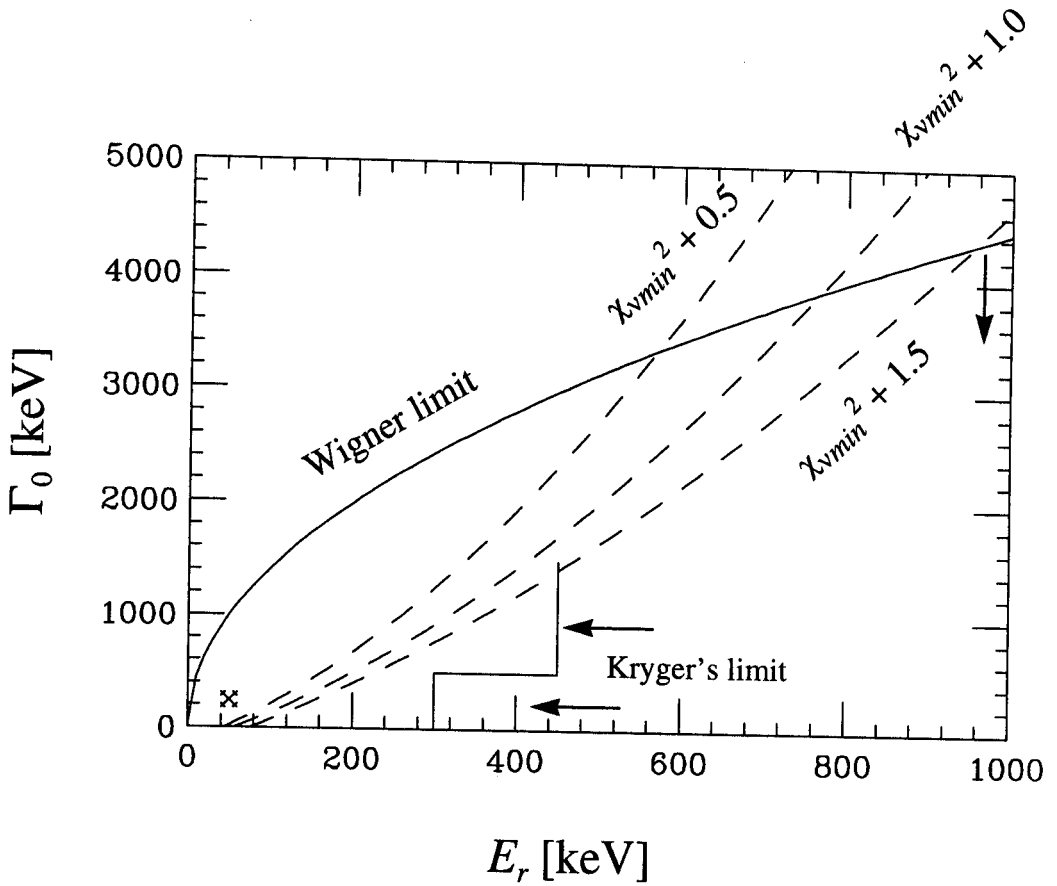

Figure 5.6: The valid region of the E_r and Γ_0 space based on the χ^2 analysis and Wigner limit for *s*-wave initial state of ^{10}Li.

by comparing the widths of the central peak simulation by Hansen [Han96] for the various scattering lengths to the width of the current central peak simulation at the resonance energy and the width for the overall reduced chi-square minimum $\chi^2_{\nu min}$. The current result of s-wave scattering length lies within the range of the Zinser's result (a_s < -20 fm).

This interpretation of the result as a low-lying s-wave ^{10}Li ground state at E_r = 50 keV and Γ_0 = 241 keV is favored by the reports of theorists by Barker and Hickey [Bar77] and Thompson and Zhukov [Tho94].

The data are compared to the calculation by Thompson and Zhukov. They used Woods-Saxon potential [Tho94] for the neutron-^{9}Li interaction and varied the parameters to calculate the ^{11}Li binding energy. The cases for a superposition of $(1p_{1/2})^2$ and $(2s_{1/2})^2$ configurations of the ^{11}Li valence neutrons were calculated. Figure 5.7 shows a comparison between their calculations and the current result.

When the fitting parameter space was explored to extract the central peak parameters for the current analysis, the p-wave initial state for the side peaks were fixed to the value which were adopted from Young *et al.* [You94]. It was E_r = 538 ± 60 keV and Γ_0 = 358 ± 20 keV. The most current report of the two neutron separation energy of ^{11}Li by Young *et al.* (S_{2n} = 295 ± 35 keV) [You93] is combined with the $1p_{1/2}$ resonance energy report by Young *et al.* and indicated as a dotted rectangular in Figure 5.7. This experimentally determined valid region is slightly outside the range of the result of three body calculations by Thompson and Zhukov [Tho94] (see Figure 2.5). The limits of a_s = -40.0 ± 5.0 fm for the present work are also indicated as the dashed lines which again were interpolated from the calculations by Thompson and Zhukov. Thus the scattering length of a_s = -40.0 ± 5.0 fm agrees well with the $1p_{1/2}$ resonance energy and the 2n-separation energy as shown by the

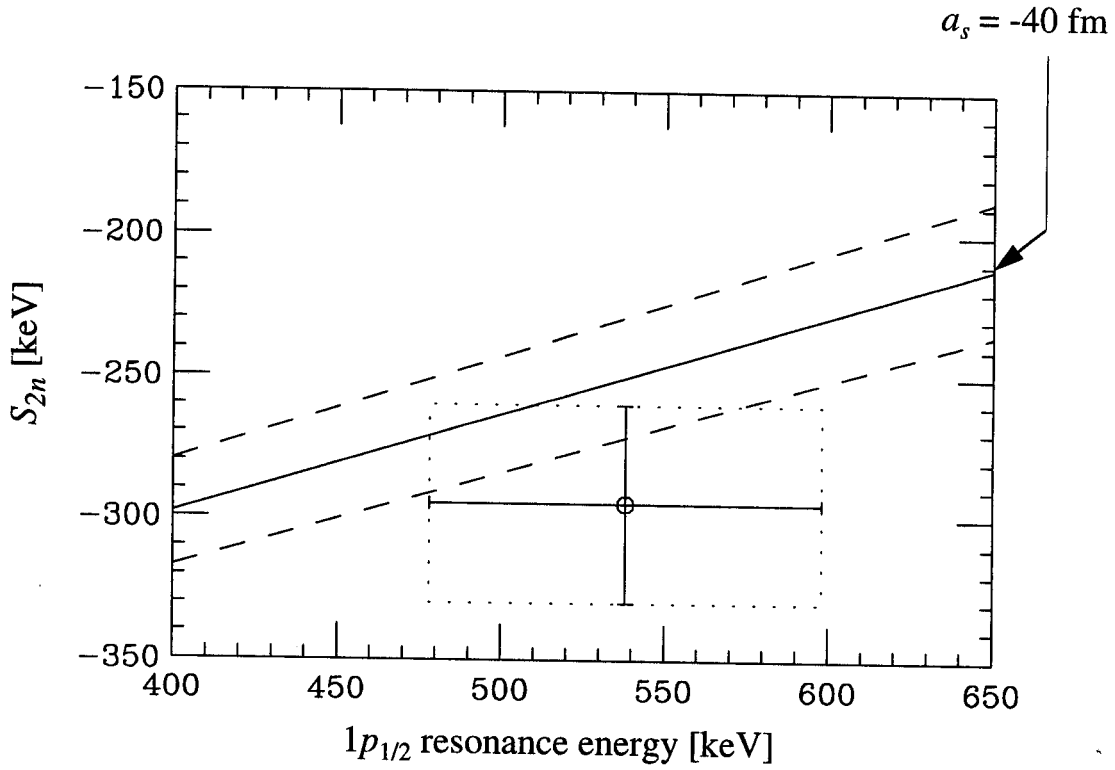

Figure 5.7: The result of the calculations with the Faddeev three body function for the ^{11}Li binding energy as a function of $1p_{1/2}$ resonance energy and the scattering length of the $1s_{1/2}$ low-lying state. The current result a_s = -40.0 fm is indicated with the solid line.

overlap over the valid regions.

The lineshapes of the low-lying s-wave state at E_r = 50 keV (a_s = -40 fm) and Γ_0 = 241 keV, and p-wave state at E_r = 538 keV and Γ_0 = 358 keV which were used to simulate the best fit of the data were plotted in Figure 5.8. The relative population of the s-wave and p-wave are 33% and 67%, respectively. Although, the p-state is populated strong, due to the energy dependent efficiency (see Figure 3.6), it appears substantially weaker in the spectrum.

The case (b) of the Figure 5.5 is still a possibility, however it is unlikely since the recent report by Zinser *et al.* [Zin95] showed strong evidence for the s-wave state in the ^{10}Li to be close to the threshold. In addition, there are no other reports for a state at $E_r \approx 2700$ keV where the state would be if it decays to the first excited state of ^{9}Li.

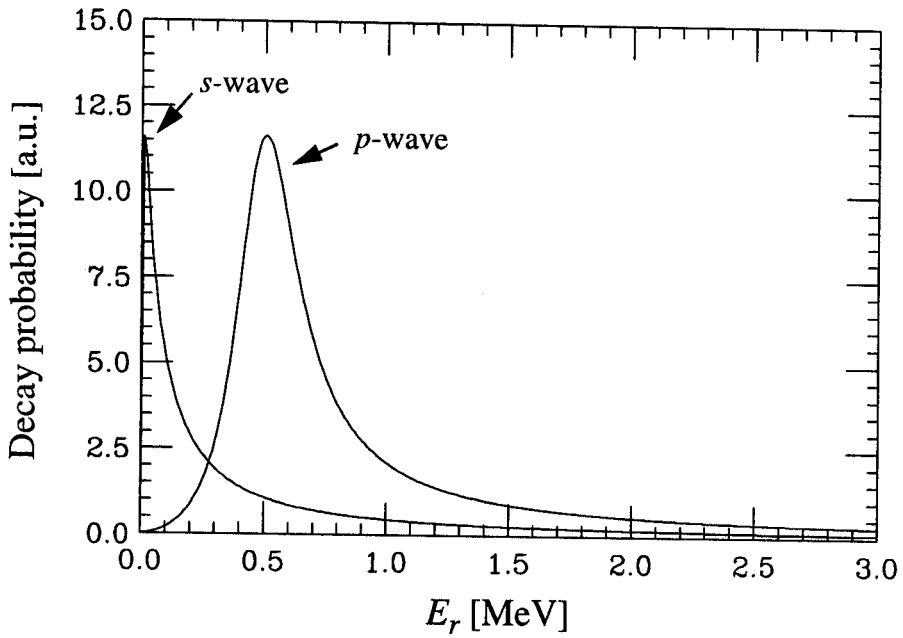

Figure 5.8: The ^{10}Li lineshapes used for the best fit of the simulation to the data. The relative population of the s-wave and p-wave is 33% and 67%, respectively.

5.3.2 The *p*-wave Case

If the initial state of the ^{10}Li neutron decay is assumed to be a *p*-wave state, the valid region of the decay energy versus decay width space can be confined as shown in the Figure 5.9. The overall minimum of the reduced chi-square $\chi^2_{\nu min} = 1.1308$, is at $E_r = 50$ keV and a decay width of $\Gamma_0 = 1.6$ keV (indicated with the x in the figure). Like the previous section, the solid line shows the Wigner limit and the dashed line indicates the surface of the reduced chi-square at $\chi^2_\nu = \chi^2_{\nu min} + 0.5$, $\chi^2_\nu = \chi^2_{\nu min} + 1.0$, and $\chi^2_\nu = \chi^2_{\nu min} + 1.5$.

If the case (a) of the Figure 5.5 is assumed, the decay energy E_r would be equal to the neutron separation energy S_n of the ^{10}Li. The reduced chi-square minimum is interpreted as the ^{10}Li *p*-wave state of $E_r = 50$ keV and $\Gamma_0 = 1.6$ keV. The statistical limit $\chi^2_\nu < \chi^2_{\nu min} + 0.5$ and the Wigner limit set the limit of the ^{10}Li *p*-wave state at $E_r < 64$ keV and $\Gamma_0 < 56$ keV. These states of ^{10}Li are much lower than the known *p*-wave state of ^{10}Li at $E_r \sim 500$ keV [You94, Boh93] and the newly reported value $E_r = 240$ keV by Ostrowski *et al.* [Ost96]. Thus the central peak observed in the current data does not correspond to the *p*-wave state at $E_r = 240$ keV observed by Ostrowski *et al.* The existence of this state cannot be ruled out, and it could be present in the data. However the resolution is not sufficient to separate it from the central peak.

Case (b) of Figure 5.5 seems unrealistic. A state at $E_r \approx 2700$ keV would most likely have a much larger width since it can decay not only to the first excited state but also to the ground state. Also, there has been no report for the state at $E_r \approx 2700$ keV from other experiments [Boh93, Ost96].

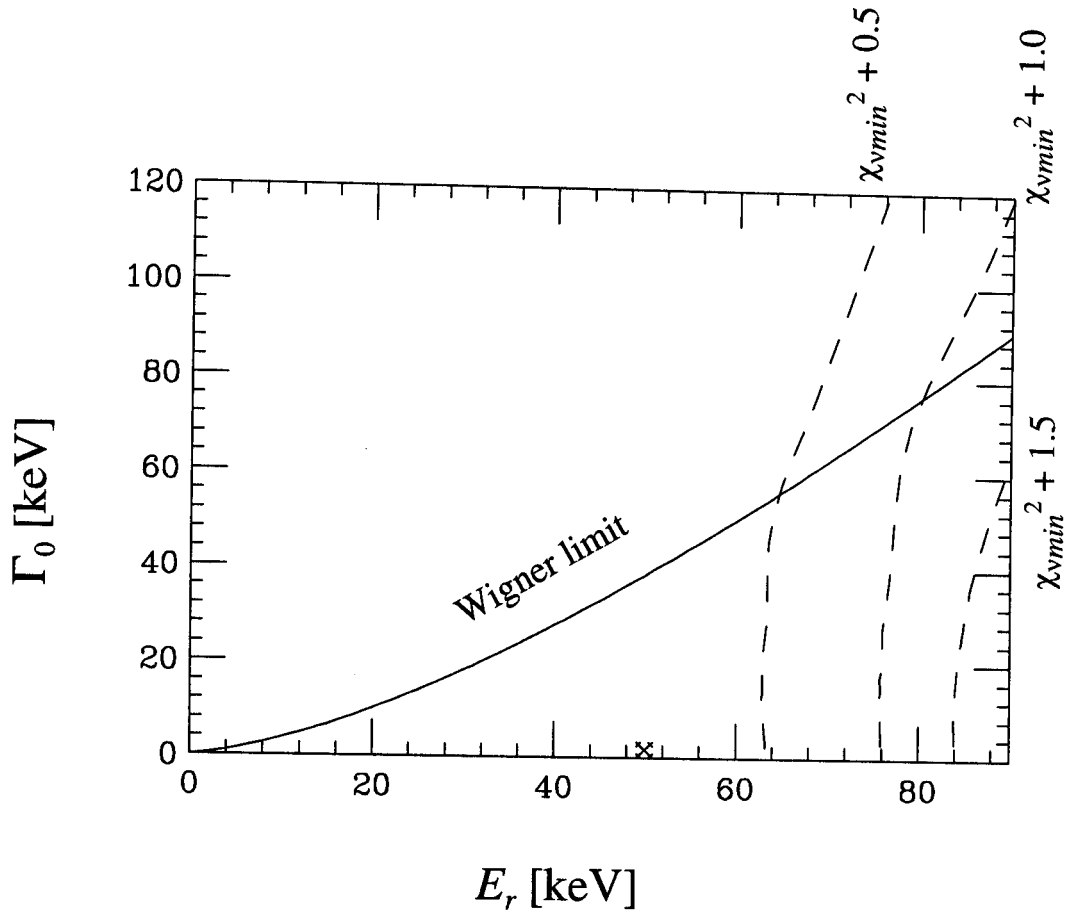

Figure 5.9: The valid region of the E_r and Γ_0 space based on the χ^2 analysis and Wigner limit for p-wave initial state of ^{10}Li.

5.4 The Relative Velocity Spectrum of ^{13}Be

There have been several attempts to measure the ground state of ^{13}Be. Ostrowski *et al.* [Ost92] employed the reaction ^{13}C(^{14}C,^{14}O)^{13}Be at E_{Lab} = 337 MeV and observed a state of S_n = -2.01 MeV and Γ_0 = 0.32 MeV as the lowest observed state. Penionzhkevich [Pen94] reported a state at a lower decay energy of 900 keV using the reaction ^{14}C(^{11}B,^{12}N)^{13}Be. The neutron transfer reaction d(^{12}Be,p) was used by Korsheninnikov *et al.* [Kor95] and in addition to other excited states the 2 MeV state was observed. Thus, the state at $E_r \approx 2.0$ MeV seems to be established, however the existence of the low-lying state is not confirmed though the existence of an intruder *s*-wave state at lower energies have been suggested by theoretical calculations [Len91, Des94, Tho96].

The relative velocity spectrum of the ^{12}Be + n coincidence events is shown in Figure 5.10. The open circles with the error bars show the data and the dotted line indicates the estimated broad Gaussian background. The spectrum has a single central peak and evidence of small side peaks around ± 2.0 cm/ns. The simulation for the side peaks was performed in the same manner as in the ^{10}Li case assuming the $d_{5/2}$ state of E_r = 2.01 MeV and Γ_0 = 0.32 MeV [Ost92] of ^{13}Be. The dashed line with two side peaks on the spectrum indicates the simulated $d_{5/2}$ state. Since the presence of the *d*-wave state at $E_r \approx 2.0$ MeV is in agreement with the previous experiments and the peak positions of the simulation and the small side peaks of the data matches well, the known $d_{5/2}$ state was assumed to be in the spectrum even though the statistics of the data for the side peaks was not sufficient to extract the resonance parameters.

Similar to the ^{10}Li case, the central peak in the relative velocity spectrum implies a lower energy decay and/or a very wide width of the initial state. It is known that the widths of

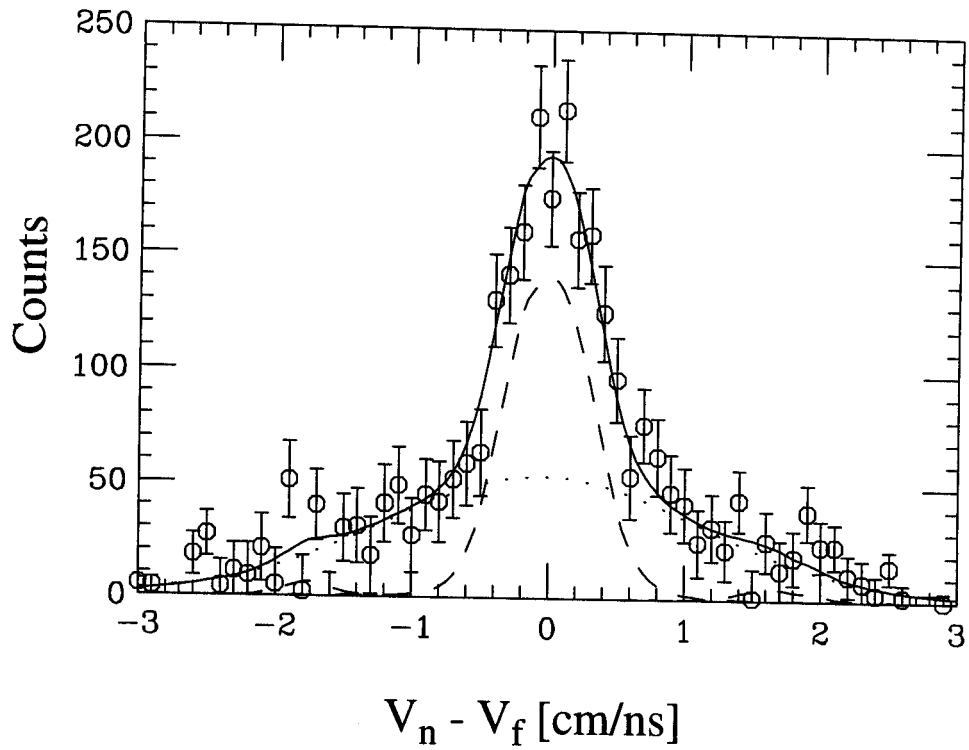

Figure 5.10: The relative velocity spectrum of the ^{12}Be + n coincidence events.

the ground state, the first and the second excited state of the ^{12}Be are narrow [Ajz80]. Thus the contribution of the final state width to the peak width in the relative velocity spectrum was negligible compared to the width of the initial state and the width broadening due to the experimental resolution.

Figure 5.11 shows a level diagram of the decay of $^{13}\text{Be} \rightarrow {}^{12}\text{Be} + \text{n}$. The energy levels of the ^{12}Be in this diagram were taken from reference [Ajz80]. Two decay scenarios can be considered to interpret the central peak in the relative velocity spectrum of ^{13}Be. They are illustrated in Figure 5.11. In case (a) of the figure, the ground state of ^{12}Be is considered to be the final state of the decay whereas in case (b) the first excited states at $E_x = 2.10$ MeV was assumed to be the final state.

In either case, the initial state was assumed to be an *s*-wave or *d*-wave since the ^{13}Be consists of a ^{12}Be core which has a filled *p* shell [Tho96] for neutrons. The case (a) or (b) of the decay process, and *s* or *d*-wave state as a initial state of the decay were assumed to extract the decay energy and the width of a ^{13}Be state from the central peak in the $^{12}\text{Be} + \text{n}$ coincidence events. The χ^2 analysis and the Wigner limit were employed to obtain the result as in the ^{10}Li case. The individual cases will be discussed in the following sections.

5.4.1 The *s*-wave Case

Figure 5.12 shows a result of the χ^2 analysis if the central peak in the relative velocity spectrum was assumed to have a *s*-wave state as an initial state. The format of the figure is the same as the ^{10}Li case. The x indicates the reduced chi-square minimum in the decay energy versus decay width plot. The reduced chi-square minimum position indicates that the state is at $E_r = 75$ keV and the decay width $\Gamma_0 = 110$ keV. The limits extracted from Figure 5.12 for the low-lying *s*-wave state are consistent with theoretical predictions [Ost92, Des94,

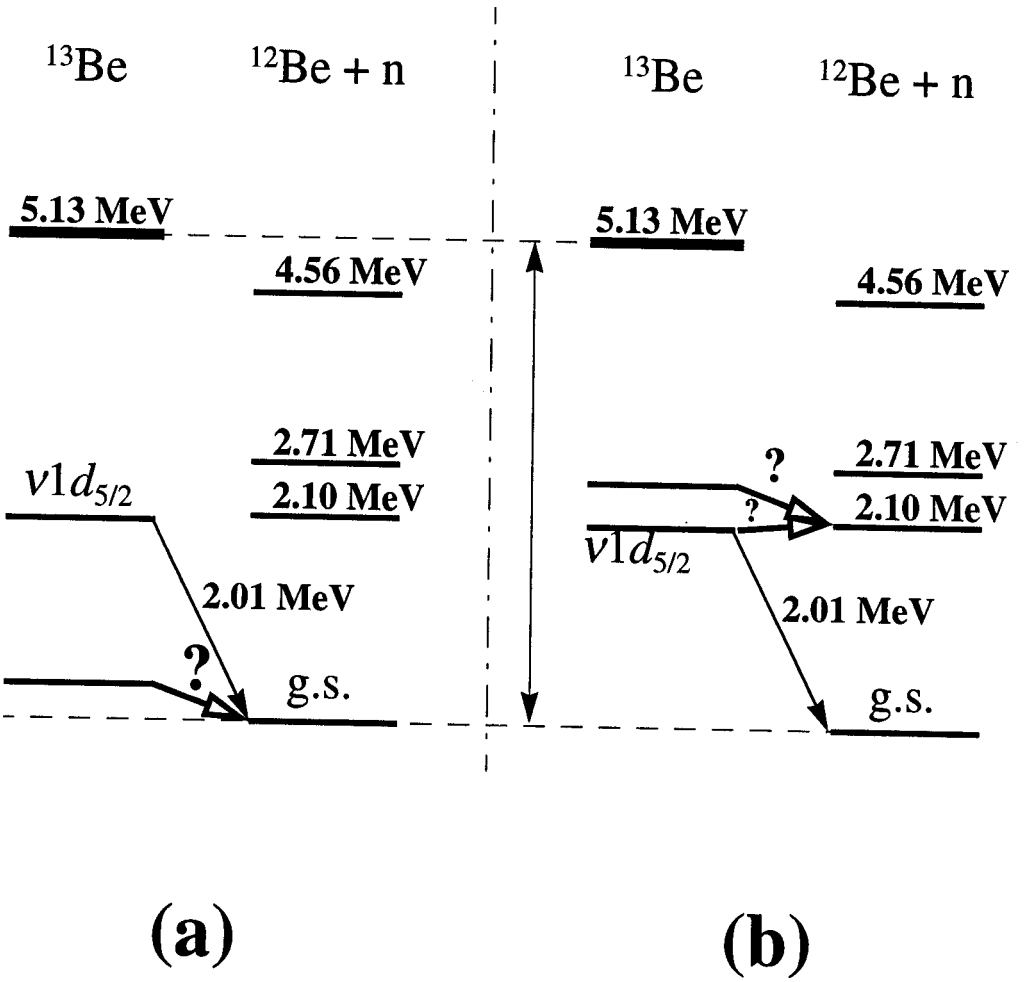

Figure 5.11: The level diagram of the possible two cases of the neutron decay of ^{13}Be.

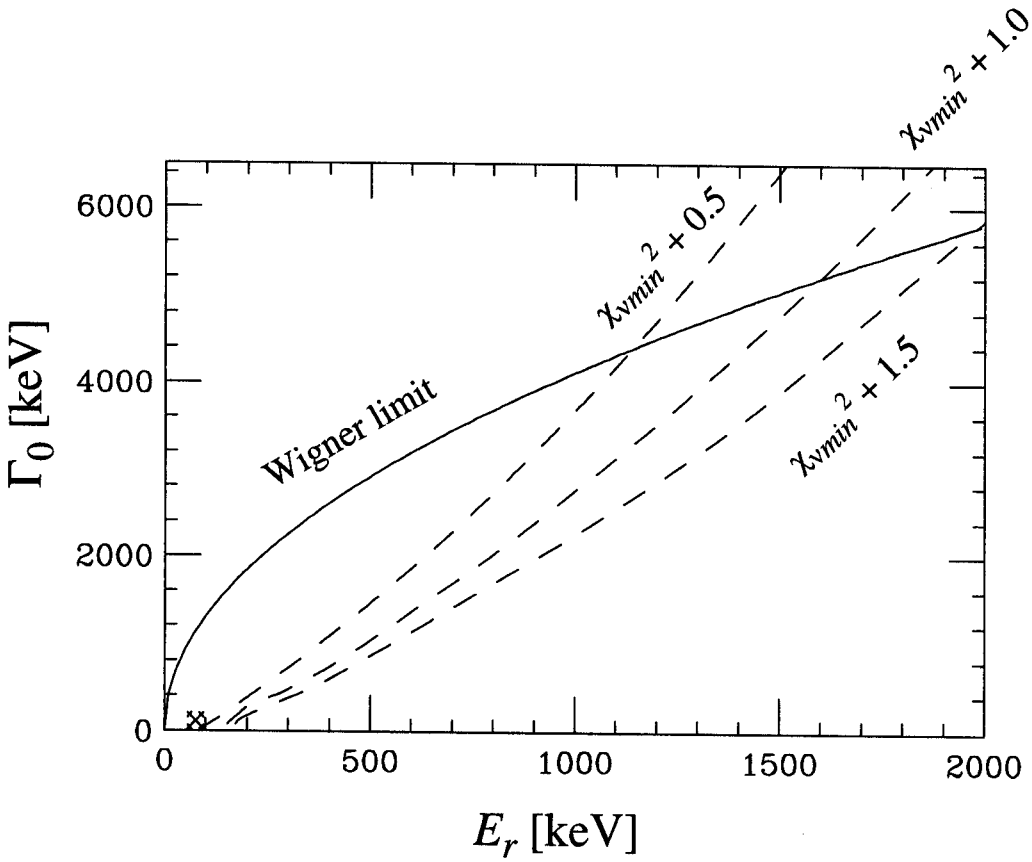

Figure 5.12: The valid region of the E_r and Γ_0 space based on the χ^2 analysis and the Wigner limit for *s*-wave initial state of ^{13}Be.

Tho96]. Lenske [Ost92] calculated the low lying *s*-wave state at $E_r \approx 900$ keV, whereas Descouvemont [Des94] predicted a slightly bound *s*-wave state ar $E_r = -9$ keV or -38 keV. Thompson and Zhukov [Tho96] calculated *s*-wave state very close to the threshold with a scattering length of $a_s \approx -130$ fm ($E_r < 10$ keV). From the constraint of $\chi^2_{\nu min} + 0.5$ and the Wigner limit, the maximum possible value for the state of this case is at $E_r \approx 1200$ keV and $\Gamma_0 \approx 4400$ keV.

The lineshapes of the best fit of the low-lying *s*-wave state at $E_r = 75$ keV and $\Gamma_0 = 110$ keV, and the known $5/2^+$ state at $E_r = 2010$ keV and the width of $\Gamma_0 = 320$ keV are shown in Figure 5.13. The relative population of the *s*-wave and *d*-wave are 44% and 56%, respectively. Although, the *d*-state is populated strong, due to the energy dependent efficiency (see Figure 3.6), it appears substantially weaker in the spectrum. These values are only estimates since the efficiency for the decay of the *d*-wave state is very low.

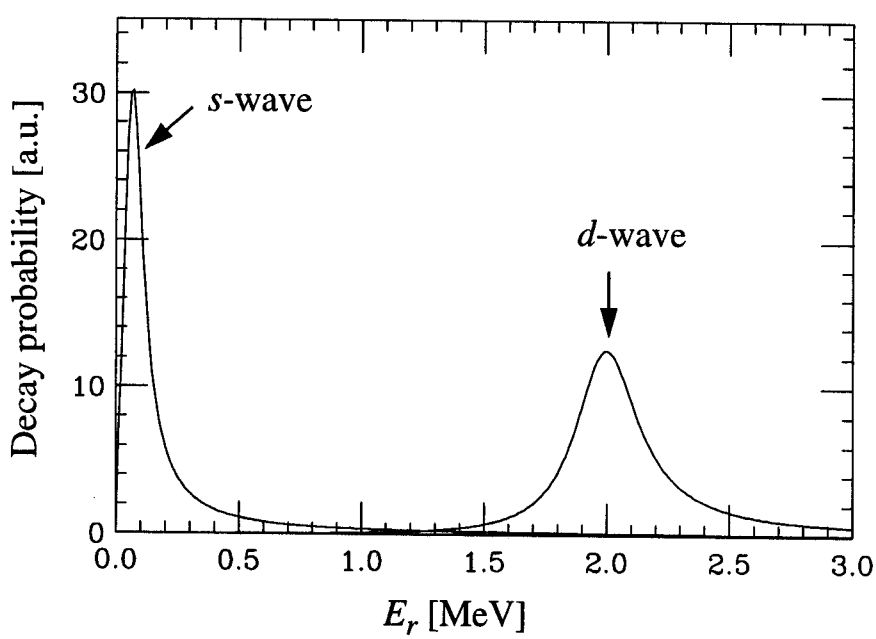

Figure 5.13: The ^{13}Be lineshapes used for the best fit of the simulation to the data. The relative population of the *s*-wave and *d*-wave is 44% and 56%, respectively.

Although it can not be ruled out, it is unlikely that the assumed *s*-wave decays to the first excited state of ^{12}Be as shown in part (b) of Figure 5.11. It would be dominating decay to the ground state with a decay energy of ~2200 keV and this would be extremely wide. Also, the experimental data reported by Ostrowski *et al.*, [Ost92], Penionzhkevich [Pen94], and Korsheninnikov *et al.* [Kor95] did not detect any states of ^{13}Be at $E_r \approx 2200$ keV.

5.4.2 The *d*-wave Case

The limit of the χ^2 analysis and the Wigner limit assuming the initial state for the central peak to be a *d*-wave state and the final state to be the ground state of ^{12}Be are plotted in Figure 5.14. The reduced chi-square minimum $\chi^2_{\nu min} = 1.07$ indicates the decay energy at $E_r = 50$ keV with essentially a width of 0 keV. As can be seen in Figure 5.14 there is no experimental limit on the width of the state. However, the decay energy has to be very small in order to reproduce the central peak and the corresponding Wigner limit makes this an very unlikely scenario. Such a narrow state should have been observed in the transfer reactions [Ost92, Pen94].

On the other hand, if the case (b) of Figure 5.11 is assumed and the excitation energy of the ^{12}Be $E_x = 2100$ keV is taken into account as an offset for the initial state energy level of ^{13}Be, the overall reduced chi-square minimum is $\chi^2_{\nu min} = 1.07$ at $E_r = 2150$ keV. Again the analysis is insensitive with respect to the width. Figure 5.15 shows the χ^2 surfaces and the Wigner limit with the offset of $E_x = 2100$ keV. Within the uncertainties this would be consistent with the known $vd_{5/2}$ state in ^{13}Be. The central peak in the relative velocity spectrum would then be due to the decay from the tail of the $vd_{5/2}$ state at $E_r = 2010$ keV in ^{13}Be to the first excited state of ^{12}Be at $E_r = 2100$ keV. Due to the larger decay energy the restriction due to the Wigner limit as in case (a) are not present and the data are consistent

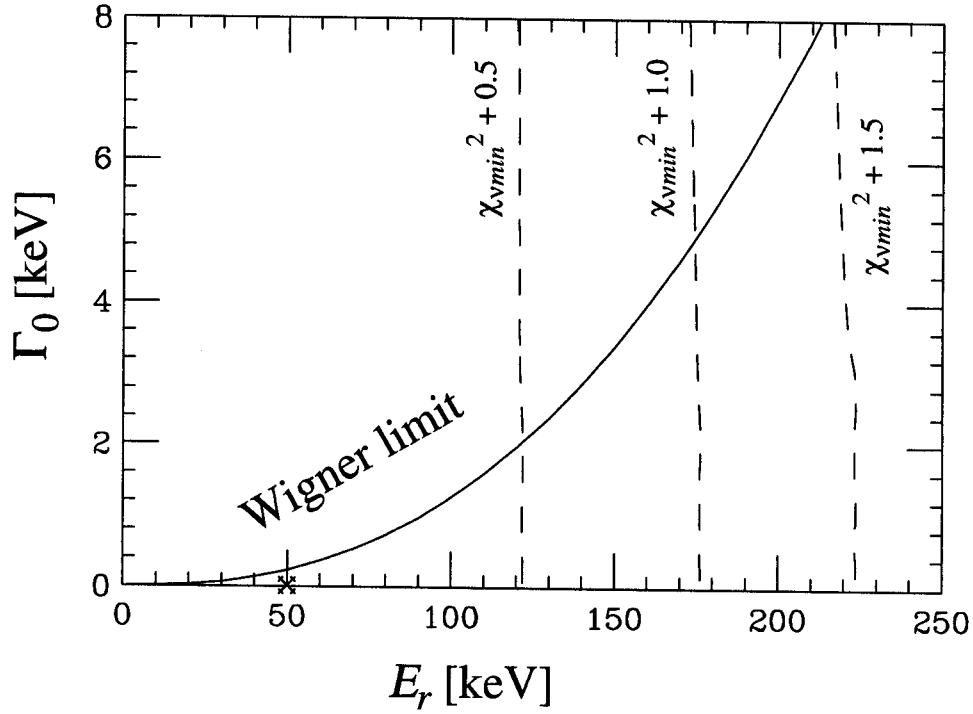

Figure 5.14: The valid region of the E_r and Γ_0 space based on the χ^2 analysis and Wigner limit for d-wave initial state of ^{13}Be. The case (a) in Figure 5.11 is assumed.

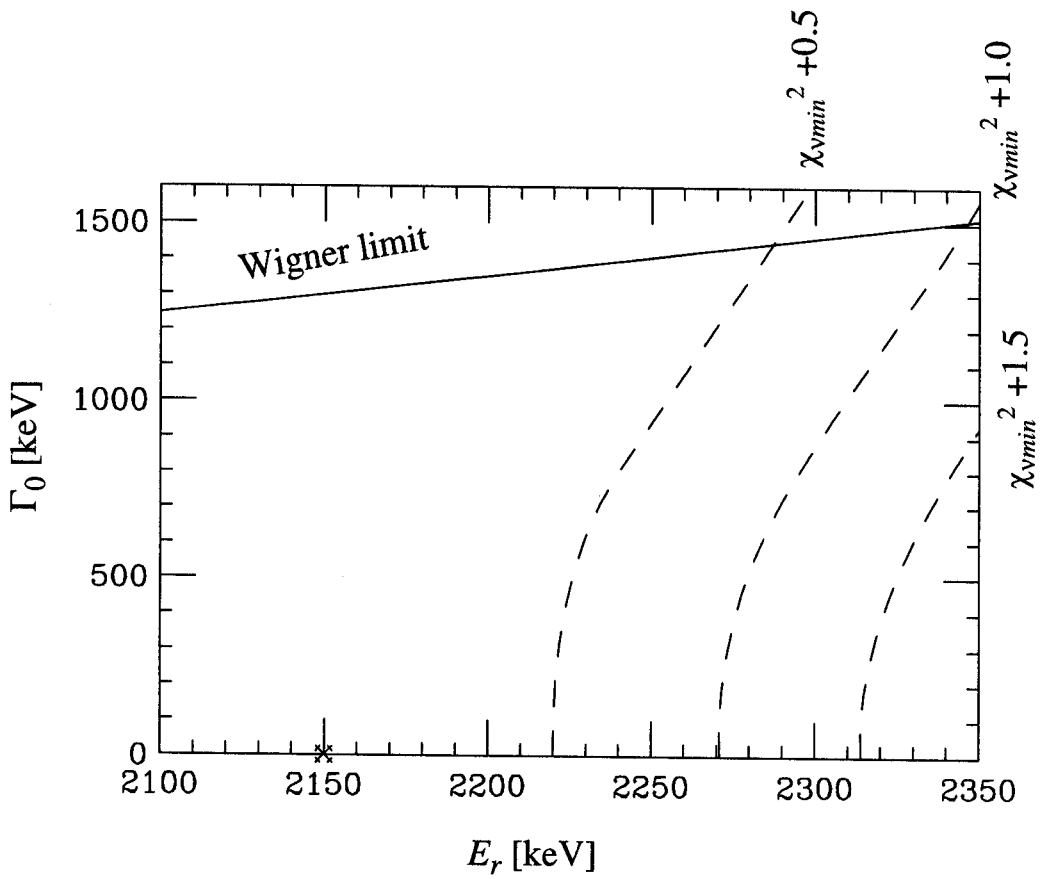

Figure 5.15: The result of χ^2 analysis in the case of *d*-wave state in ^{13}Be as an initial state and the first excited state of ^{12}Be as a final state.

with the measurement of $\Gamma = 300$ keV [Ost92]. Thus the scenario is a possible explanation of the data. The branching ratio for the decay to the first excited state and the ground state respectively have to be extracted from the shell model calculations, however as explained in the last section the present data is not very sensitive to the strength distribution.

Chapter 6

Summary and Conclusions

The sequential neutron decay spectroscopy (SNDS) at 0° was employed to study light nuclei beyond the neutron dripline, ^{10}Li and ^{13}Be. The nuclei of interest and the nuclei for the calibration (^{7}He) were created via fragmentation and decayed immediately to one neutron and a daughter fragment (^{9}Li, ^{12}Be, and ^{6}He). Neutrons and the daughter fragments were detected in coincidence and relative velocity spectra were obtained for each isotope from their information of velocities.

The relative velocity spectra was compared with the spectra created by Monte Carlo simulations. The simulation code included the decay kinematics, the beam optics, the detector geometry, and the detector efficiencies. The code was tested and adjusted by comparing the data of the known decay of ^{7}He and the simulation. Decay parameters of the observed peaks were extracted with χ^2 tests.

The result of the ^{10}Li data analysis concluded that the ground state of ^{10}Li is most likely the low-lying *s*-wave state. The result obtained suggested the ground state at $E_r \approx 50$ keV and $\Gamma_0 \approx 240$ keV or in terms of the *s*-wave scattering length, $a_s \approx$ -40.0 fm. It is consistent with the recent experimental data reported by Zinser *et al.* [Zin95] and the three-body calculations for ^{11}Li reported by Thompson and Zhukov [Tho94]. The current work experimentally established the existence of the low-lying *s*-wave ground state of ^{10}Li which was

suggested experimentally by Kryger *et al.* [Kry93], Young *et al.* [You94], and Zinzer *et al.* [Zin95] and predicted theoretically by Thompson and Zhukov [Tho94]. It is unlikely to improve the experimental limits of the low-lying *s*-wave ground state in near future due to its wide width for the low energy level, however the *p*-wave states at 500 ~ 200 keV observed by Bohlen *et al.* [Boh93] and Ostrowski *et al.* [Ost96] still need to be resolved.

The conclusions from ^{13}Be data showed that there are two possible scenarios for the observed neutron decay of ^{13}Be. The decay was either from a low-lying *s*-wave ground state of ^{13}Be to the ground state of ^{12}Be or from a tail of the known $5/2^+$ state [Ost92] of ^{13}Be to the first excited state of ^{12}Be. The current result does not distinguish those two cases. One way to resolve these two cases in the future would be to measure γ-rays in coincidence with a neutron and ^{12}Be. If the final state of the decay which caused the central peak is the first excited state of ^{12}Be, the events would be followed by γ-ray emissions. Further experimental information of the ^{13}Be ground state is awaited for the understanding of the neutron dripline nucleus ^{14}Be.

BIBLIOGRAPHY

BIBLIOGRAPHY

[Ajz80] F. Ajzenberg-Selove and C.L. Busch, Nucl. Phys. **A 336**, 1 (1980).

[Ajz88] F. Ajzenberg-Selove, Nucl. Phys. **A 490**, 1 (1988).

[Ame90] A.I. Amelin, M.G. Gornov, Yu.B. Gurov, A.L. Il'in, P.V. Morokhov, V.A. Pechkurov, V.I. Savel'ev, F.M. Sergeev, S.A. Smirnov, B.A. Chernyshev, R.R. Shafigullin, and A.V. Shishkov, Sov. J. Nucl. Phys. **52**, 782 (1990).

[Aud93] G. Audi and A.H. Wapstra, Nucl. Phys. **A 565**, 66 (1993).

[Ban92] J.M. Bang and I.J. Thompson, Phys. Lett. **B 279**, 201 (1992).

[Bar77] F.C. Barker and G.T. Hickey, J. Phys. **G 3**, L23 (1977).

[Ber91] G.F. Bertsch and H. Esbensen, Ann. Phys. **209**, 327 (1991).

[Bev69] P.R. Bevington, *Data Reduction and Error Analysis for the Physical Sciences*, McGraw-Hill (1969).

[Boh93] H.G. Bohlen, B. Gebauer, M. von Lucke-Petsch, W. von Oertzen, A.N. Ostrowski, M. Wilpert, Th. Wilpert, H. Lenske, D.V. Alezandrov, A.S. Demyanova, E. Nikolskii, A.A. Korsheninnikov, A.A. Ogloblin, R. Kalpakcheva, Y.E. Penionzhkevich, and S. Piskor, Z. Phys. **A 344**, 381 (1993).

[Cec79] R.A. Cecil, B.D. Anderson, and R. Madey, Nucl. Instrum. Meth. **161**, 439 (1979).

[Che70] Y.S. Chen, W.D. Harrison, and T.A. Tombrello, Bull. Am. Phys. Soc. **15**, 1598 (1970).

[Deá87] F. Deák, A. Kiss, Z. Seres, G. Caskey, A. Galonski and B. Remington, Nucl. Instrum. and Meth. **A 258**, 67 (1987).

[Des94] P. Descouvemont, Phys. Lett. **B 331**, 271 (1994).

[Esb92] H. Esbensen and G.F. Bertsch, Phys. Rev. **C 46**, 1552 (1992). See also G.F. Bertsch and H. Esbensen, Ann. Phys. (N. Y.) **209**, 327 (1991).

[Fox89] R. Fox, R. Au, and A. VanderMolen, IEEE Trans. on Nucl. Sci. **36**, 1562 (1989).

[Fox92] R. Fox and J.S. Winfield, NSCL Data acquisition system reference guide, (1992).

[Gol74] A.S. Goldhaber, Phys. Lett. **B 53**, 306 (1974).

[Gre75] D.E. Greiner, P.J. Lindstron, H.H. Heckman, B. Cork and F.S. Bieser, Phys. Rev. Lett. **35**, 152 (1975).

[Han87] P.G. Hansen and B. Jonson, Europhys. Lett. **4**, 409 (1987).

[Han95] P.G. Hansen, A.S. Jensen, and B. Jonson, Ann. Rev. Nucl. Part. Sci. 1995 **45,** 591 (1995).

[Han96] P.G. Hansen, (private communication).

[Hei90] L.H. Heilbronn, Ph. D. Thesis, unpublished, Michigan State University (1990).

[Hel88] J.H. Heltsley, L. Brandon, A. Galonsky, L. Heilbronn, B.A. Remington, S. Langer, A. Vander Molen, J. Yurkon, and J. Kasagi, Nucl. Instrum. Meth. **A 263**, 441 (1988).

[Hüf81] J. Hüfner and M.C. Nemes, Phys. Rev. **C 23**, 2538 (1981).

[Ish96] M. Ishihara, Contribution to the Gull Lake Conference on Nuclear Physics Near the Driplines, August 21 - 24, 1996, Gull Lake, Michigan (1996).

[Kno89] G.F. Knoll, *Radiation Detection and Measurement*, John Willey & Sons, Inc. (1989).

[Kob88] T. Kobayashi, O. Yamakawa, K. Omata, and I. Tanihata, Phys. Rev. Lett. **60**, 2599 (1988).

[Kob92] T. Kobayashi, Nucl. Phys. **A538**, 343c (1992).

[Kor95] A.A. Korsheninnikov, E. Yu. Nikolskii, T. Kobayashi, D.V. Aleksandrov, M. Fujimaki, H. Kumagai, A.A. Ogloblin, A. Ozawa, I. Tanihata, Y. Watanabe, and K. Yoshida, Phys. Lett. **B 343**, 53 (1995).

[Kow87] S. Kowalski and H.A. Enge, RAYTRACE manual, Laboratory of Nuclear Science and Department of Physics, Massachusetts Institute of Technology, (1987).

[Kra88] Kenneth S. Krane, *Introductory Nuclear Physics*, John Wiley & Sons (1988).

[Kry93] R.A. Kryger, A. Azhari, A. Galonsky, J.H. Kelley, R. Pfaff, E. Ramakrishnan, D. Sackett, B. M. Sherrill, M. Thoennessen, J.A. Winger, and S. Yokoyama, Phys. Rev. **C 47**, R2439 (1993).

[Lan58] A.M. Lane and R.G. Thomas, Rev. Mod. Phys. **30**, 257 (1958).

[Lav73] A. Laverne and C. Gignoux, Nucl. Phys. **A 203**, 597 (1973).

[Len91] H. Lenske, Proc. Int. Symp. on Structure and Reactions of Unstable Nuclei 1991, edited by K. Ikeda and Y. Suzuki, World Scientific, Singapore (1991).

[Mig73] A.B. Migdal, Sov. J. Nucl. Phys. **16**, 238 (1973).

[Oak92] The formulas and parameters of J.F. Ziegler, *The Stopping and Ranges of Ions in Matter*, Vols. 3 & 5, Pergamon Press (1980), coded by OakRidge National Laboratory, doc. in HHIRF_UBOOK, (1992).

[Orr92] N.A. Orr, N. Anantaraman, Sam M. Austin, C.A. Bertulani, K. Hanold, J.H. Kelley, D.J. Morrissey, B.M. Sherrill, G.A. Souliotis, M. Thoennessen, J.S. Winfield, and J.A. Winger, Phys. Rev. Lett. **69**, 2050 (1992).

[Ost92] A.N. Ostrowski, H.G. Bohlen, A.S. Demyanova, B. Gebauer, R. Kalpakchieva, Ch. Langner, H. Lenske, M. von Lucke-Petsch, W. von Oertzen, A.A. Ogloblin, Y.E. Penionzhkevich, M. Wilpert, Th. Wilpert, Z. Phys. **343**, 489 (1992).

[Ost96] A.N. Ostrowski, H.G. Bohlen, B. Gebauer, S.M. Grimes, R. Kalpakchieva, A.A. Korsheninnikov, T.N. Massey, W. von Oertzen, A.A. Ogloblin, Y.E. Penionzhkevich, CH. Seyfert, Th. Stolla, M. Wilpert, and Th. Wilpert, Proceedings of the International Workshop XXIV on Gross Properties of Nuclei and Nuclear excitations, edited by H. Feldmeier, J. Knoll, and W. Nörenberg, GSI, Germany (1996).

[Pen94] Yu. E. Penionzhkevich, Proc. of the IV. Int. Conf. on Selected Topics In Nuclear Structure, edited by V.G. Soloviev, Dubna, Russia (1994).

[Pop85] N.A.F.M. Poppelier, L.D. Wood, and P.W.M. Glaudemans, Phys. Lett. **157B**, 120 (1985).

[Rei68] R. Reid, Ann. Phys. **50**, 411 (1968).

[Rol88] Rolfs and Rodney, *Cauldrons in the Cosmos*, The University of Chicago Press (1988).

[Tal60] I. Talmi and I. Unna, Phys. Rev. Lett. **4**, 469 (1960).

[Tan85] I. Tanihata, H. Hamagaki, O. Hashimoto, Y. Shida, N. Yoshikawa, K. Sugimoto, O. Yamakawa, and T. Kobayashi, Phys. Rev. Lett. **55**, 2676 (1985).

[Thi75] C. Thibault, R. Klapisch, C. Rigaud, A.M. Poskanzer, R. Prieels, L. Lessard, and W. Reisdorf, Phys. Rev. **C 12**, 644 (1975).

[Tho94] I.J. Thompson and M.V. Zhukov, Phys. Rev. **C 49**, 1904 (1994).

[Tho96] I.J. Thompson and M.V. Zhukov, Phys. Rev. **C 53**, 708 (1996).

[Tou75] R. de Tourreil and D.W.L. Sprung, Nucle. Phys. **A 242**, 445 (1975).

[Wap85] A.H. Wapsta, G. Audi, and K. Bos, Nucl. Phys. **A 432**, 1 (1985).

[Won90] S.S.M. Wong, *Introductory Nuclear Physics*, Prentice Hall, N.J., USA 1990.

[Wou88] J.M. Wouters, R.H. Kraus, Jr., D. J. Viera, G.W. Butler, and K.E.G. Löbner, Z. Phys. **A 331**, 229 (1988).

[Wil75] K.H. Wilcox, R.B. Weisenmiller, G.J. Wozniak, N.A. Jelley, D. Ashery, and J. Cerny, Phys. Lett. **59B**, 142 (1975).

[Win92] J.A. Winger, B.M. Sherrill, and D.J. Morrissey, Nucl. Instrum. Meth. **B 70**, 380 (1992).

[You93] B.M. Young, W. Benenson, M. Fauerbach, J.H. Kelley, R. Pfaff, B.M. Sherrill, M. Steiner, J.S. Winfield, T. Kubo, M. Hellström, N.A. Orr, J. Steatson, J.A. Winger, and S.J. Yennello, Phys. Rev. Lett. **71**, 4124 (1993).

[You94] B.M. Young, W. Benenson, J.H. Kelley, N.A. Orr, R. Pfaff, B.M. Sherrill, M. Steiner, M. Thoennessen, J.S. Winfield, J.A. Winger, S.J. Yennello, and A. Zeller, Phys. Rev. **C 49**, 279 (1994).

[Vol65] A.B. Volkov, Nucl. Phys. **74**, 33 (1965).

[Zin95] M. Zinser, F. Humbert, T. Nilsson, W. Schwab, Th. Blaich, M.J.G. Borge, L.V. Chulkov, H. Eickhoff, Th.W. Elze, H. Emling, B. Franzke, H. Freieslleben, H. Gissel, K. Grimm, D. Guillemaud-Mueller, P.G. Hansen, R. Holzmann, H. Irnich, B. Jonson, J.G. Keller, O. Klepper, H. Klinger, J.V. Kratz, R. Kulessa, D. Lambrecht, Y. Leifels, A. Magel, M. Mohar, A.C. Mueller, G. Münzenberg, F. Nickel, G. Nyman, A. Richiter, K. Riisager, C. Sheidenberger, G. Schrieder, B.M. Sherill, H. Simon, K. Stelzer, J. Stroth, O. Tengblad, W. Trautmann, E. Wajda, and E. Zude, Phys. Rev. Lett. **75**, 1719 (1995).